Université de Montréal

Topological order in a broken-symmetry state

par
Roger Alexander Müller

Département de Physique
Faculté des arts et des sciences

Thèse présentée à la Faculté des études supérieures
en vue de l'obtention du grade de Philosophiæ Doctor (Ph.D.)
en Physique

Mai, 2015

Université de Montréal
Faculté des études supérieures

Cette thèse intitulée:

Topological order in a broken-symmetry state

présentée par:

Roger Alexander Müller

a été évaluée à un jury composé des personnes suivantes:

Prof. Sjoerd Roorda,	président-rapporteur
Prof. Andrea D. Bianchi,	directeur de recherche
Prof. Richard MacKenzie,	membre du jury
Prof. Ion Garate,	examinateur externe
Prof. William Skene,	représentant du doyen de la FES

Thèse acceptée le: . . . .

RÉSUMÉ

À travers cette thèse, nous revisitons les différentes étapes qui ont conduit à la découverte des isolants topologiques, suite à quoi nous nous penchons sur la question à savoir si une phase topologiquement non-triviale peut coexister avec un état de symétrie brisée. Nous abordons les concepts les plus importants dans la description de ce nouvel état de la matière, et tentons de comprendre les conséquences fascinantes qui en découlent. Il s'agit d'un champ de recherche fortement alimenté par la théorie, ainsi, l'étude du cadre théorique est nécessaire pour atteindre une compréhension profonde du sujet. Le chapitre 1 comprend un retour sur l'effet de Hall quantique, afin de motiver les sections subséquentes. Le chapitre 2 présente la première réalisation d'un isolant topologique à deux dimensions dans un puits quantique de HgTe/CdTe, suite à quoi ces résultats sont généralisés à trois dimensions. Nous verrons ensuite comment incorporer des principes de topologie dans la caractérisation d'un système spécifique, à l'aide d'invariants topologiques. Le chapitre 3 introduit le premier dérivé de l'état isolant topologique, soit l'isolant topologique antiferromagnétique (ITAF). Après avoir motivé théoriquement le sujet et introduit un invariant propre à ce nouvel état ITAF, qui est couplé à l'ordre de Néel, nous explorons, dans les chapitres 4 et 5, deux candidats de choix pour la phase ITAF : GdBiPt et NdBiPt.

Mots-clés: Effet de Hall quantique, isolant topologique, isolant topologique antiferromagnétique, invariant topologique, théorie du champ cristallin, état de symétrie brisée, symétrie par renversement du temps, diffraction de neutrons, diffraction de rayons X, antiferromagnétique, NdBiPt, GdBiPt, SmB_6

ABSTRACT

In this thesis we will revisit the different steps that led to the discovery of the topological insulator before we then ask the question if a topologically non-trivial phase can coexist with a broken symmetry state. We will see the most important concepts in describing this new state of matter, and we will try to understand what its fascinating consequences are. This field of research is heavily driven by theory, therefore taking first a look at the underlying theoretical framework, will enable us to gain a deeper understanding of the subject. In Chapter 1 we will review the quantum Hall effect to motivate the subject. Chapter 2 deals with the first realization of a two-dimensional topological insulator in a HgTe/CdTe quantum well and then generalizes these results to 3 dimensions. We will also see how one can incorporate principles of topology to characterize a specific system with the use of topological invariants. Chapter 3 will introduce the first derivative of the topological insulator state, the antiferromagnetic topological insulator (AFTI). After theoretically motivating the subject and introducing a proper invariant for this new AFTI phase that is coupled to the Néel order, we will then investigate in Chapters 4 and 5, two prime candidates for the AFTI phase; GdBiPt and NdBiPt.

Keywords: Quantum Hall effect, Topological insulator, Antiferromagnetic topological insulator, Topological invariant, Crystal field theory, broken symmetry state, Time reversal symmetry, Neutron diffraction, X-ray diffraction, Antiferromagnetism, NdBiPt, GdBiPt, SmB_6.

CONTENTS

LIST OF TABLES

LIST OF FIGURES

LIST OF ABBREVIATIONS

2D	Two dimensions
2DEG	Two-dimensional electron gas
3D	Three dimensions
ABINIT	Density functional theory program
AFM	Antiferromagnetic
AFTI	Antiferromagnetic topological insulator
ARPES	Angle-resolved photo emission spectroscopy
CEF	Crystalline electric field
DFT	Density functional theory
FM	Ferromagnetic
irrep	Irreducible representation of a group G
NRC	National research council
PM	Paramagnetic
PSI	Paul Scherrer Institute, Villigen, Switzerland
PBE	Perdew, Burke and Ernzerhof generalized gradient approximation for exchange correlation
QHE	Quantum Hall effect
QSHE	Quantum spin Hall effect
SdH	Shubnikov–de Haas effect
SO	Spin-orbit
SOC	Spin-orbit coupling
sARPES	Spin angle resolved photo emission spectroscopie
TKKN	Thouless, Khomoto, Nightingale

TR	Time-reversal symmetry
S	Combined symmetry class: primitive lattice translation and time-reversal S$=\Theta T_{1/2}$
Θ	Time reversal symmetry
$T_{1/2}$	Primitive lattice translational symmetry

NOTATION

$4f^n$	Fourth electronic orbital f (L = 3) containing n electrons
$(h\ k\ l)$	Miller indices of a crystalline plane
$[h\ k\ l]$	Miller indices describing a family of crystalline planes
Å	Angstrom (10^{-10}m)
B	Magnetic field
B_n	CEF amplitudes
c	speed of light (294 792 458 m/s)
$\chi(M)$	Chern number divided by 2π
C_p	Specific heat at constant pressure
C_{el}	Electronic specific heat
C_{ph}	Phonon specific heat
C_{mag}	Magnetic contribution to specific heat
CeBiPt	Cerium bismuth platinum
$\chi(T)$	Magnetic susceptibility
β	$(k_\mathrm{B}T)^{-1}$
d_c	Critical thickness of a quantum well
d	Angular moment orbital l = 2
E	Electric field
e^*	Elementary charge $1.602176565(35) \times 10^{?19}$C
f	Angular moment orbital l = 3
fcc	Face center cubic lattice

γ	Sommerfeld constant of the electronic contribution to the specific heat
Γ_6	Band formed by p-orbitals
Γ_8	Band formed by s-orbitals
GdBiPt	Gadolinium bismuth platinum
g_J	Landé factor ($\frac{3}{2}+\frac{1}{2}\left[\frac{S(S+1)-L(L+1)}{J(J+1)}\right]$)
γ_n	Neutron gyromagnetic ratio
g	Genus of a manifold
H	Hamiltonian operator
$HgTe/CdTe$	Mercury telluride/cadmium telluride
Hz	Hertz (seconds^{-1})
$\vec{J}$	Total angular moment quantum number
$\overrightarrow{k}$	Wave vector
k_B	Boltzmann constant (8.617×10^{-2} meV/K)
m^*	Efficient electron mass
μ_B	Bohr magneton (9.2741×10^{-21}erg·G^{-1})
μ_{eff}	Efficient magnetic moment ($g_J\mu_\mathrm{B}\sqrt{J(J+1)}$)
MeV	Mega electron volts
N	Nitrogen
ν	Conduction electron density in a electron gas
N_A	Avogadro number (6.023×10^{23})
NdBiPt	Neodymium bismuth platinum

O	Oxygen
O_n^m	Steven's equivalent operator
p	Angular moment orbital L = 1
ϕ_0	Quanta de flux magnétique (2.07×10^{-7} G·cm^2)
F$\bar{4}$3m	Symmetry group Nr. 216
ρ	Electric resistivity
σ	Electric conductivity
$\vec{q}$	Reciprocal lattice vector
$\rho(T)$	Electric resistivity
ρ_{xx}	Longitudinal electric resistivity
ρ_{xy}	Transverse electric resistivity
R	Universal gas constant ($8.3144621(75)$ JK^{1}mol^1)
RE	Rare earth elements
R_H	Hall resistivity
R_K	Von Klitzing constant $25812.807557(18)$ Ω
s	Angular moment orbital l = 0
$\overrightarrow{S}$	Intrinsic angular momentum (spin)
θ_{CW}	Curie-Weiss temperature
θ_D	Debye temperature
T_N	Néel temperature
τ	Drift time
ξ	Berry connection
YdBiPt	Ytterbium bismuth platinum

To my parents and my sister

ACKNOWLEDGMENTS

I want to thank my director of research Prof. Andrea Bianchi for giving me the opportunity to do a doctorate. I could widely profit from your vast knowledge in experimental physics and I learned many valuable lessons from you, some go beyond physics. I would also like to include Prof. Tami Pereg-Barnea, Prof. Carlos Silva, Prof. Michel Côté, Prof. Richard Leonelli and Prof. Dominic Ryan for always offering a helping hand, trusting me with your equipment or simply keeping up the morale at times needed.

I thank the members of my group Bobby, Reza, Alexandre, Luc and Nicholas for your help and camaraderie.

My gratitude goes to Jacqueline, Anne and Lynda for helping me with so many administrative hurdles, you all do a tremendous job and I would have been lost many times without you.

I want to thank my mother Rosemarie, my father Franz and my sister Nicole for your love, support and belief in me at all times - you are the best.

My dear friend Nyssa Marchand, I am so lucky to have had you at my side for all these years. You have broadened my horizon and enriched my live in so many ways. Bernhard Hüssy I thank you for a lifelong friendship, your loyalty and for always having my back. All my other friends, thank you for your support and love; Matthew Leddy, Paule Dagenais, Mortimer Julius Chen, Rick Reid, Philippe Richelet, Andreea Doroftei, Werner Tobias Christ, Cyrill Gaudenz von Planta, William Drury III, Louise Pothier, Marlène and petite cocotte Marie St.Denis.

Thank you Bílý Kůň.

Montréal you have been a fabulous home for the past years and I'm leaving you with tears in my eyes.

♡

INTRODUCTION

> `That's all I have to say about that.`
>
> *Forrest Gump*

Preface

During the last century, physics has proven to be a powerful framework for the description of the many different states matter can form. Symmetries, or more precisely their breaking, led much like Ariadne's thread to a classifications of these states. In 1980, Klaus von Klitzing cut that thread by describing a new quantum state of matter which does not follow this pattern, but shed light on a family of materials, only characterized by their Hilbert space topology. In this new state of matter, the bulk of a two dimensional sample stays insulating, whereas along its edges a unidirectional current is circulating, giving rise to the quantum Hall effect (QHE) in a two-dimensional electron gas (2DEG). Inspired by the mathematical field of topology, the quantized conductivity of such a material can be associated with a topological invariant. In mathematics, such an invariant describes a property of a topology that remains unchanged under homeomorphisms. For example, the number of holes in a two-dimensional manifold cannot be changed by stretching it.

In solid state physics, we can adapt this concept of smooth deformations to the topology of the Hilbert space, which describes the band structure of an insulator. As long as these transformations are adiabatic, the topological invariant will not change, and therefore the band gap at the Fermi level of the material remains unaffected. Two years after von Klitzing's discovery of the QHE, Thouless, Kohmoto, Nightingale and den Nijs (TKNN) [1] developed the concept of topological invariants in their description of the same effect. The TKNN number represents the topology of the system in the form of an integral of the Bloch wave functions over the Brillouin zone. This operation results in an integer number which also corresponds to the number of dissipation less edge modes. The edge modes are guaranteed by the topology and are also protected by it. The goal of this new topological classification scheme, is the description of phenomena, independent of specific material characteristics, like the quantized Hall current.

The TKNN number, however, explicitly breaks time reversal (TR) symmetry and is therefore zero in a time-reversal-invariant system. While the quantum Hall state in a 2DEG requires an applied magnetic field that breaks time reversal symmetry, in the case of a Hg/CdTe quantum well, strong spin-orbit coupling acts as an effective field [2] and TR symmetry is preserved. If the well is thinner than a critical value d_c, it behaves like a conventional insulator. For $d_{QW} > d_c$ the topological invariant changes and a single pair of helical edge stages that form a Kramers pair counter propagate on the same edge. In consequence, the magneto-transport in such a quantum well shows steps [3].

Spin-orbit coupling is also at the origin of topological insulators in three dimensions [4–6]. Experimentally, spin- and angle-resolved photoemission spectroscopy (ARPES) on bismuth doped with antimony showed the presence of metallic surface states, as well as a spin texture [7]. At the same time, *ab initio* calculations predict a small gap in the electronic spectrum for the bulk of this material [8].

In 2010 theorists have proposed a new type of topological insulator where the topological phase is bound to an antiferromagnetic phase transition [4]. One of the main problems in experimentally testing a material for its topologically non trivial properties lies in the fact that conventional transport measurements are challenging due to the small band gap, usually in the range of a few milli-electronvolts, of all known TI's. This is where the idea of the topological phase being bound to a conventional phase transition becomes interesting, because it allows further methods in researching this new state of matter. In this thesis we study two possible candidates for a derivative state of the topological insulator, GdBiPt and NdBiPt, where the topologically non-trivial phase coexists with a broken symmetry state, i.e. antiferromagnetic order. Both materials belong to the family of half-Heusler rear-earth compounds that show many interesting features, ranging from superconductivity, antiferromagnetic order to super-heavy fermion behaviour [9–16].

CHAPTER 1

QUANTUM HALL EFFECT

> **"It must be carefully remembered, that the mechanical force which urges a conductor carrying a current across the lines of magnetic force, acts, not on the electric current, but on the conductor which carries it.[...] If the current itself be free to choose any path through a fixed solid conductor or a network of wires, then, when a constant magnetic force is made to act on the system, the path of the current through the conductors is not permanently altered but after certain transient phenomena, called induction currents, have subsided, the distribution of the current will be found to be the same as if no magnetic force were in action."**
>
> *James Maxwell*

1.1 Introduction

In 1879 Edwin H. Hall, puzzled by the above words of Maxwell (noted in Vol.II of the series *Electricity and Magnetism*), set out to find an experiment in which he could show that indeed, the current in a fixed conductor is itself manipulated by a magnetic field. He was convinced that such a current should be drawn to one side of the wire, which in return would have an effect on the resistance [17]. He concluded that if a wire, carrying a current, is exposed to a magnetic field perpendicular to the direction of the current, he would be able to measure a potential difference across the wire, perpendicular to the current and the magnetic field. Hall successfully conducted such an experiment and could prove that the magnetic field deflects the electrons as expected, perpendicular to itself and to the velocity of the electrons along the wire.

According to the theory of Drude, an electron is accelerated by an electric field for an average time τ, before being scattered by an impurity, a lattice imperfection or a phonon. The drift velocity of an electron in average is:

$$\mathbf{v}_d = -e\mathbf{E}\tau/m \tag{1.1}$$

The component of the electric field, perpendicular to the current direction, that ensures the electrons move along the wire, is called the Hall field E_{H}. One can determine its magnitude based on the fact that the two forces perpendicular to the wire, the Lorentz force due to the magnetic field and the the force due to the perpendicular component of the electric field, must cancel each other out. The Lorentz force acting on the electrons is:

$$\mathbf{F} = e(\mathbf{E} + \frac{\mathbf{v}}{c} \wedge \mathbf{B}). \tag{1.2}$$

In the flat geometry of a Hall bar setup, the electrons can only flow along the x-direction with the velocity v_x. The Lorentz force becomes:

$$F_y = e(E_y - \frac{v_x}{c} B_z). \tag{1.3}$$

With the electrons flowing in the x-direction, the net force is zero along the y and z-direction, so Equation 1.3 has to be equal to zero and

$$E_{\mathrm{H}} = E_y = \frac{1}{c} v_d B_z. \tag{1.4}$$

The current density $\mathbf{j}$ and the drift velocity $\mathbf{v}_d$ are connected to each other by

$$\mathbf{j} = -\eta e \mathbf{v}_d, \tag{1.5}$$

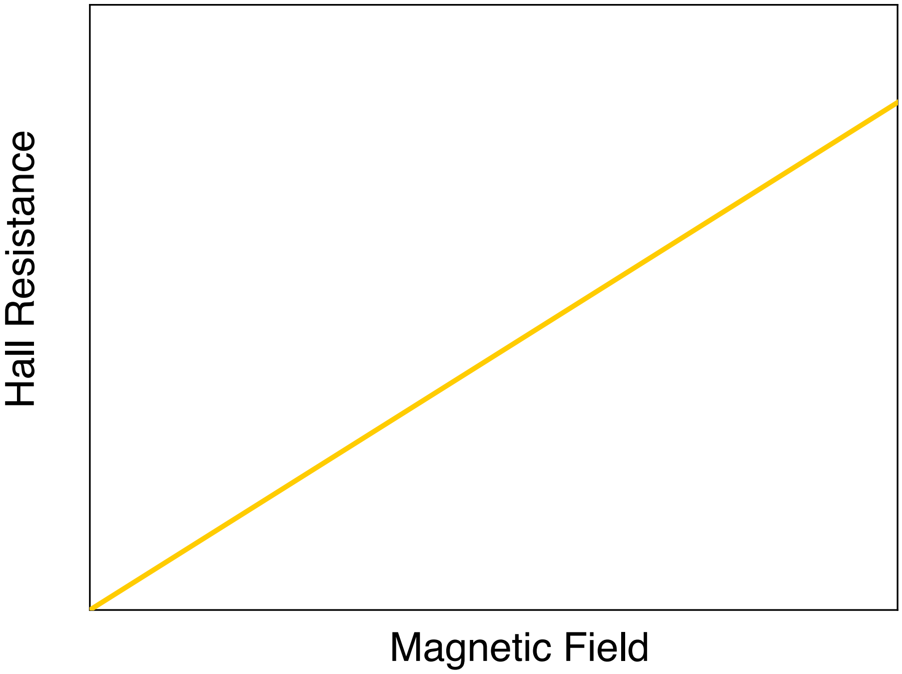

Figure 1.1: *Hall resistance vs. magnetic field*

where η is the the conduction electron density. We can therefore write

$$E_{\mathrm{H}} = -\frac{1}{c}\frac{1}{\eta e} j B_z = R_{\mathrm{H}} B_z, \tag{1.6}$$

where

$$R_{\mathrm{H}} = -\frac{1}{c}\frac{1}{\eta e} \tag{1.7}$$

is called the Hall constant which depends only on the conduction electron density η.

1.2 Integer quantum Hall effect

Having revisited the important results of the classical Hall effect, we now want to develop a quantum mechanical description from scratch. We start off with a magnetic field $\mathbf{B} = \nabla \wedge \mathbf{A}$, perpendicular to the xy-plane of a 2DEG. The magnetic field only being defined up to the rotation of a vector potential $\mathbf{A}$ leaves us with a freedom of gauge, i.e. if we look at the two possible potentials

$$\mathbf{A_1} \; : \; B(0,x,0) \qquad \text{and} \tag{1.8}$$

$$\mathbf{A_2} \; : \; \frac{B}{2}(-y,x,0), \tag{1.9}$$

we realize, that both result in the same magnetic field along the z-direction,

$$\mathbf{B} : (0,0,B). \tag{1.10}$$

For the following considerations we choose a particular gauge, the so called Landau gauge, to simplify the problem at hand.

$$\mathbf{A} = Bx\hat{\mathbf{y}}. \tag{1.11}$$

In the Hamiltonian that describes a single electron exposed to a magnetic field, the canonical momentum is not just mass × velocity, it has an extra term due to the vector potential in the Lagrangian:

$$p = \partial_{\dot{x}} L = mv + qA \tag{1.12}$$

which leads to

$$H = \frac{1}{2m}\left[\mathbf{p} + \frac{e}{c}\mathbf{A}(\mathbf{r})\right]^2, \tag{1.13}$$

with the vector potential $\mathbf{A}(\mathbf{r})$ and m describing the mass of the electron. If we quantize the system we have to replace the generalized momentum in the Hamiltonian with its operator:

$$\mathbf{p} \rightarrow \frac{\hbar}{i}\frac{\partial}{\partial x_j}. \tag{1.14}$$

Rewriting the Hamiltonian with the Landau gauge fixed, we arrive at:

$$H = \frac{1}{2m}\left[-\hbar^2 \frac{\partial^2}{\partial x^2} - \hbar^2 \frac{\partial^2}{\partial y^2} + 2\frac{\hbar e}{ic} Bx \frac{\partial}{\partial y} + \frac{e^2}{c^2} B^2 x^2 \right]. \tag{1.15}$$

To solve the Schrödingier equation $H\psi = E\psi$, we can make a single-particle Ansatz on the fact that the momentum operator p_y commutes with the Hamiltonian (1.15), meaning they share the same eigenfunctions [18].

$$\psi_{kn}(x,y) = \phi_{kn}(x)e^{iky} \tag{1.16}$$

is an eigenfunction of p_y; an extended wave in y-direction while localized in x-direction. Using periodic boundary conditions along a length L_y on the y-axis and by applying (1.15) on the wave function (1.16) one obtains, after dividing by e^{iky} on both sides, the single particle Schrödinger equation

$$\left[-\frac{\hbar^2}{2m}\frac{d^2}{dx^2} + \frac{e^2 B^2}{2mc^2}\left(\frac{\hbar c}{eB}k + x\right)^2 \right] \phi_{kn}(x) = E_{kn}\phi_{kn}(x). \tag{1.17}$$

This is the harmonic oscillator equation centered at postion $x = -(\hbar c/eB)k$ for each allowed value of $k = 2\pi l_k/L_y$, with $l_k = 0, \pm 1, \pm 2, ...$ and L_y the length imposed by the boundary condition.

$\omega_c = eB/(mc)$ is the cyclotron frequency. The eigenvalues are then simply:

$$E_{nk} = (n + \frac{1}{2})\hbar\omega_c \qquad n = 0, 1, 2, ... \tag{1.18}$$

One can see that the energy eigenvalues do not depend on the momentum $\hbar k$, but only on the index n, which is called the Landau level index. To determine the degeneracy of such a level, we will have to sum up all states with the same index n. One can understand this as how many such oscillators "fit" into one level. The distance $\triangle x$ between two oscillator centre positions x_{k_1} and x_{k_2}, with $x_k = -(\hbar c/eB)k$ is given by

$$\triangle x = -\frac{\hbar c}{eB}\frac{2\pi}{L_y}. \tag{1.19}$$

This results in $L_x/\triangle x = \frac{eBL_xL_y}{2\pi\hbar c}$ states per Landau level for a width of L_x. At this point it is useful to define a new quantity, called the filling factor $\nu = \frac{2\pi\hbar c\eta}{eB}$. Where η defines the number of electrons per unit area. For example, for $\nu = 1$, all the states of the lowest Landau level $n = 0$,within the area $A = L_xL_y$ are filled.

The Pauli principle tells us that each level associated with the quantum number n can contain as many electrons as the degree of degeneracy of the level, given by $L_x/\triangle x$, so spin is implicitly taken care of.

If we look at a case where the filling factor takes on a certain value ν_0, describing completely filled levels, we can then express the number of electrons per unit area by

$$\eta = \nu_0\frac{L_x}{\triangle xA} = \nu_0\frac{eB}{hc}. \tag{1.20}$$

If we now go back to equation 1.7, we can easily obtain the relation between the current j_x and the perpendicular component E_y of the electric field

$$j_x = -\frac{\eta e}{B}E_y = -\nu_0\frac{e^2}{h}E_y. \tag{1.21}$$

This results in a Hall resistivity of

$$R_{\mathrm{H}} = -\frac{h}{e^2\nu_0}. \tag{1.22}$$

The quantized Hall resistivity is therefore described by the quantum number n of filled Landau levels

$$R_{\mathrm{H}} = -\frac{h}{ne^2}, \tag{1.23}$$

expressing the fact that the ratio between j_x and E_y is an integer divided by a constant, h/e^2 equal to 25813 ohm. The quantization of the Hall resistance is experimentally confirmed to one part in 10^9 [19]

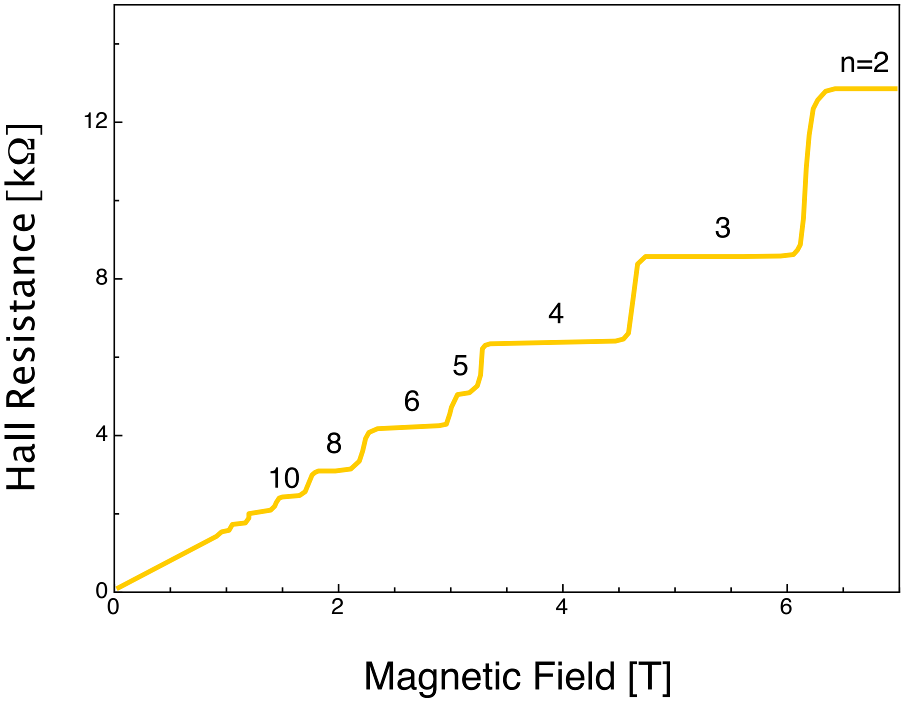

Figure 1.2: . Hall resistance versus Magnetic field, forming a plateau after reaching each new Landau level n.

1.3 Argument of Laughlin

In 1981 Robert Laughlin, at the time still working at Bell laboratories, proposed a different, a somewhat more technical approach to explain the quantum Hall effect [20]. To understand further concepts within our subject, we will have to take a look at his ideas.

Again, we start from the two dimensional geometry of a thin strip in an external magnetic field, containing just one electron for the time being. Further we consider a uniform magnetic field which is contained to the centre of the strip, in the sense that the outer ends in $\pm\hat{y}$ direction are not effected by the field.

If we turn on a transverse electric field along the y-direction, the current carried by a single-particle state is described by the density operator [21]

$$\mathbf{J} = -\frac{e}{m}\big(\mathbf{p} + \frac{e}{c}\mathbf{A}\big) \tag{1.24}$$

This operator is proportional to the derivative of (1.13) with respect to the vector potential. With this observation, we now can use a trick, by introducing a purely fictitios vector potential $\mathbf{a} = -(q\Phi_0/L_y)\hat{y}$ [21]. Φ_0 is one flux quantum hc/e and q is a dimensionless parameter. It is important to notice that we didn't add any new physics to the system, since $\nabla \wedge \mathbf{a} = 0$. With this additional potential, we end up with the new Hamiltonian

$$H(q) = \frac{1}{2m}\big[\mathbf{p} + \frac{e}{c}\mathbf{A}(\mathbf{r}) - q\frac{e}{c}\frac{\Phi_0}{L_y}\hat{\mathbf{y}}\big]^2. \tag{1.25}$$

and for the current density operator in y-direction we can write in similar fashion

$$J_y = -\frac{e}{m}\big(\mathbf{p} + \frac{e}{c}\mathbf{A} - \frac{qh}{L_y}\hat{\mathbf{y}}\big) \cdot \hat{\mathbf{y}}. \tag{1.26}$$

Now the question is, what do we learn by comparing this current with the derivative of the Hamiltonian, with respect to the purely artificial vector potential:

$$J_y = \frac{eL_y}{h}\frac{\partial H(q)}{\partial q} \tag{1.27}$$

It seems that we can evaluate the current in y-direction, in any state by forming the expectation value of the derivative of the Hamiltonian with respect to our fictitious vector potential in that state. That means, that if we have a current carring state, this expectation value must be non-zero and therefore connects the eigenvalue spectrum directly to the fictitious vector potential. What seems like a paradox at first, can be resolved by adding a phase to the electron wave function, the so-called Aharonov-Bohm phase

$$\phi_{A.B.} = \frac{-e}{\hbar c} \int \mathbf{a} \cdot d\mathbf{r}. \tag{1.28}$$

Laughlin then considered the following situation. If we take the two dimensional band and tie it together at the ends, letting it form a loop in the yz-plane (see Fig. 1.3), the newly added term $q\Phi_0 = qhc/e$ could be the result of a real magnetic field, piercing the center of the loop with q flux quanta [21]. If we integrate 1.28 along the y-direction we get:

$$\phi_{A.B.} = 2\pi q. \tag{1.29}$$

Therefore, the phase factor is periodic in flux Φ_0, that is piercing the system through an enclosed area.

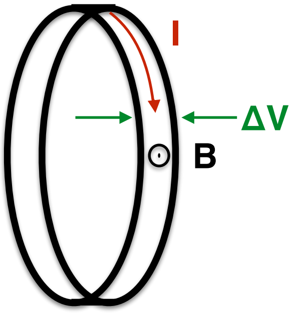

Figure 1.3: . Scheme of the loop in the Laughlin ansatz.

Going back to our electron, we have to advance its wave function by this value as it travels once around the circumference L_y. What we have left out so far is the fact that, additional to its Aharonov-Bohm phase, the phase of the wave function also advances by kL_y, where k is the wavenumber along the y-direction of the ribbon. As long as the parameter q is an integer we don't add anything due to 1.29 and the standard wave numbers, $k_i = 2\pi i/L_y$

with $i = 0, \pm 1, \pm 2, ...$ keep the wave function single valued. In the case of a non-integer q though, the phase added by the artificial vector potential would no longer be a multiple of 2π and the wave numbers k_i would make the wave function multi-valued. But there is a trick. We can adjust the wave numbers in a way that $k_i L_y$ brings in an extra phase, which precisely cancels the phase due to the vector potential $\mathbf{a}$:

$$k_i = 2\pi(i - q)/L_y. \tag{1.30}$$

This is a very interesting result. Equation (1.30) indicates that $\mathbf{a}$ changes the boundary conditions depending on whether the number of flux quanta piercing our system is integer or not.

So far, we have assumed the localization length of our wave function to be L_y. But what happens if our wave function is much more localized? In this case we have $l \ll L_y$, where $l = \sqrt{\hbar c/eB}$ (see eq.1.17), and the wave function will not run the risk of being multi-valued. The same wave function stays single-valued as we go around the ribbon no matter what q is. That mean that the Hamiltonian can no longer depend on q and cannot therefore describe a system in which the wave function carries a current. This situation of very localized wave functions, we find for example in disordered insulators, where electrons are constrained to the vicinity of impurities and cannot be deflected by the magnetic field.

We want to apply this trick now to a two dimensional electron gas, confined to a circular ribbon with width L_x and circumference L_y. We turn on an electric field $\mathbf{E} = E_x \hat{\mathbf{x}}$ across the ribbon and then calculate the Hall resistance. The Hamiltonian, still in Landau gauge, with the electric field turned on, becomes:

$$H(q)\psi_\alpha(x,y) = \left\{ \frac{1}{2m}\big[\mathbf{p} + \frac{e}{c}B\big(x - q\frac{\Phi_0}{BL_y}\big)\hat{\mathbf{y}}\big]^2 + eE_x x \right\} \psi_\alpha(x,y) = E_\alpha \psi_\alpha(x,y). \tag{1.31}$$

By now adding flux q to the system, we make the harmonic oscillator centre positions (as in eq.1.17) march from $x_{ki} = -k_i l^2 = -(2\pi i/L_y)(\hbar c/eB)$ to $x_{ki} + q\Phi_0/BL_y$. Again we use the single-particle Ansatz $\phi^q_{kn} e^{iky}$. Inserting this into (1.31) leaves us after factorization, with

$$\begin{aligned} H(q)\phi^q_{kn} e^{iky} &= \Big\{ \frac{1}{2m} p_x^2 + \frac{1}{2} m\omega_c^2 \big[x + \big(x_k - \frac{q\Phi_0}{BL_y} + \frac{v_d}{\omega_c}\big)\big]^2 \\ &\quad - \frac{1}{2} m v_d^2 - \hbar k v_d + e\frac{E_x q\Phi_0}{BL_y} \Big\} \phi^q_{kn} e^{iky}, \end{aligned} \tag{1.32}$$

where $v_d = cE/B$ is the classical drift velocity defined in equation 1.2. We can see that the Hall field introduces a dependence of the eigenvalues on the wavenumber k and therefore, on the oscillator centre x_k. This connects the energy of the system to the amount of flux quanta q we insert. By "moving" the single-particle states, they increase their energy and we have to do work on the system in order to insert flux, much like a quantum pump. If we adiabatically insert precisely one flux quantum, the single-particle states and their energies do not change but while doing so all occupied states march one step over to the right, so that in the process we have transferred exactly one electron per occupied Landau level across the width of the ribbon. This cost energy, exactly $\Delta E = neE_x L_x$, n sitll describing the number of occupied Landau levels. We have thus described the transfer of charge from one edge of the loop to the other (see Fig. 1.4).

We have seen in the last section that the eigenvalues of our non-interacting system, in the absence of an external electric field, are described by delta functions at the energies $E = (n + \frac{1}{2})\hbar\omega_c$. Each of these delta peaks must have a weight of $\frac{L_x L_y}{2\pi l^2}$, $l = \sqrt{\hbar c/eB}$ denoting the localization length of each state, as already described above. By adding electrons to the system, the chemical potential will always be at one of these energies, except we reach an integer number of filled Landau levels. The regions between the Landau levels are called *mobility gaps*. If the chemical potential moves into a mobility gap, the occupa-

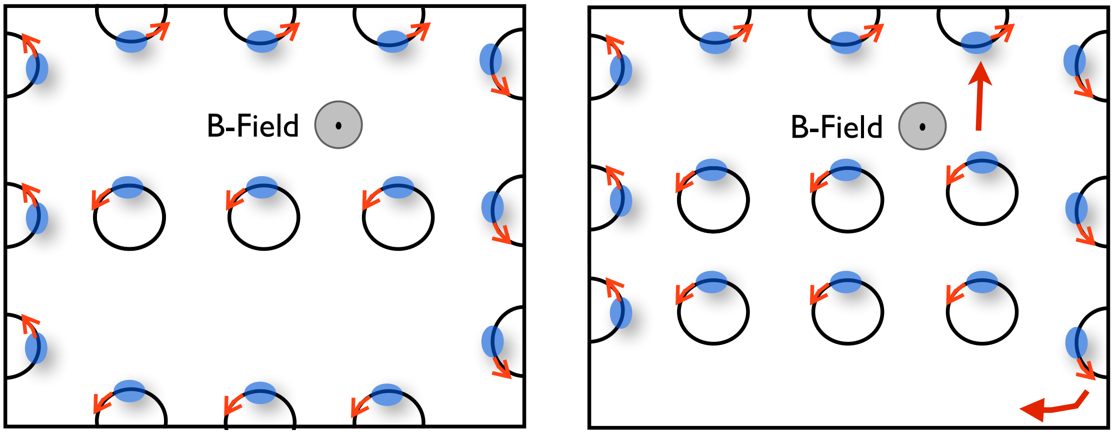

Figure 1.4: The left panel shows the electrons trapped in a circular motion, only the edge modes can't complete a full circle. The right panel shows the situation as we introduce flux and the positions of the orbits start moving across the hall ribbon. Tis motion creates a Hall potential that leads to a net current along the edge as the edge modes complete their orbits in a sort of "skipping motion".

tion of extended states does not change and, since these states are the carrier of current, the Hall resistance will not change. Therefore, we will record a Hall plateau, as depicted in figure 1.2, leaving the system dissipation-less until the next Landau level is reached.

Let us now take a look at what happens if we turn on an electric field in the y-direction. The resistivity tensor of the system shall be described by ρ. In two dimensions, the Hall resistance (1.23) is related to the resistivity tensor ρ as, $R_{\mathrm{H}} = -\rho_{xy}$ - resistivity and resistance are the same quantity. If we assume no dissipation, based on the arguments in the last paragraph, the diagonal component of this tensor must vanish [21] and only the off-diagonal elements are non-zero. This is because the diagonal term of the conductivity tensor $\sigma = \rho^{-1}$ can be entirely expressed in terms of states at the Fermi level [22]. The off-diagonal terms, on the other hand, are determined by all the states below the Fermi level. Therefore if the Fermi energy lies in the mobility gap, we find $\rho_{xx} = 0$ for $T = 0$; if $T \neq 0$, ρ_{xx} is not exactly zero but exponentially small so that we can assume it to be zero [22].

$$\rho = \begin{pmatrix} 0 & \rho_{xy} \\ -\rho_{xy} & 0 \end{pmatrix}.$$

For an electric field in the y-direction we can write using Faraday's law [21]:

$$\frac{1}{c}\frac{d\Phi}{dt} = \frac{1}{c}\int d\mathbf{S}\cdot\frac{d\mathbf{B}}{dt} = \int_{\mathscr{C}} dl\cdot\mathbf{E}_y = \int_{\mathscr{C}} dl\rho_{yx}j_x, \tag{1.33}$$

where $\mathscr{C}$ is a contour enclosing the flux quantum and $j_x = J_x/L_y$ is the current density in x-direction, the response of the system to the applied field. If we carry out the Integral over $t = \pm\infty$, we can relate the change in flux $\Delta\Phi$ to the charge that is transferred along the width x of the ribbon:

$$\frac{1}{c}\Delta\Phi = \rho_{yx}\int_{\mathscr{C}} dl\int dt\, j_x = \rho_{yx}\int dt J_x. \tag{1.34}$$

If we now set the amount of flux introduced to one flux quantum, $\Delta\Phi = \Phi_0$, the total charge that is transferred is equal to $\int dt J_x$ which must be equal to $-ne$, where n is the number of occupied Landau levels. We can therefore write

$$\frac{1}{c}\Phi_0 = -\rho_y x n e, \tag{1.35}$$

which leads, using $\Phi_0 = hc/e$, to the result obtained earlier for the Hall resistivity

$$\rho_{xy} = -\frac{h}{ne^2}. \tag{1.36}$$

Having reached the same result twice, raises the question, why we had to indulge in this second, more complicated solution by Laughlin. The reason is that so far we have only considered an ideal, non-interacting system. In a real system, we will find interacting electrons in the presence of disorder. The gauge-invariant argument of Laughlin has the

advantage that it is independent of the details of the system and allows us therefore, to also describe a real system with disorder.
Let us summarize the most important results so far.

- Only states that are extended over the whole system can carry charge across the Hall bar, driven by the inserted flux.
- The system remains dissipation less as long as the Fermi energy lies within a mobility gap, giving rise to the Hall plateaus.
- By inserting exactly one flux quantum, the eigenstates of the system remain unchanged.

The last point has the interesting consequence that, as we adiabatically add one flux quantum to the system, the occupation of single-particle states can only change within a Landau level, otherwise the gap has to be overcome, which can not happen adiabatically. Therefore we have to interpret the change in the system, as the transfer of n electrons from one side of the system to the other. This phenomenon of a dissipation less edge current will turn out to be important in the following chapters. Earlier, we have used the argument that if the Fermi energy lies within a mobility gap, there will be no increase in occupation of extended states, which leads to the Hall plateaus. If we introduce impurities to our system, extended states will start to mix, due to scattering off the impurities. This scattering will broaden each Landau level into a band. Backed on experimental knowledge [21], we know that the centre of each Landau band always carries a number of extended states, while the states in the tail of each band will be occupied by localized states in the vicinity of impurities (see fig:1.5).

If a certain number of Landau levels are completely filled, described by the quantum number n, the Fermi level remains in between two Landau levels, in the gap. Varying the filling factor η will only result in a change in the occupation of the electrons within

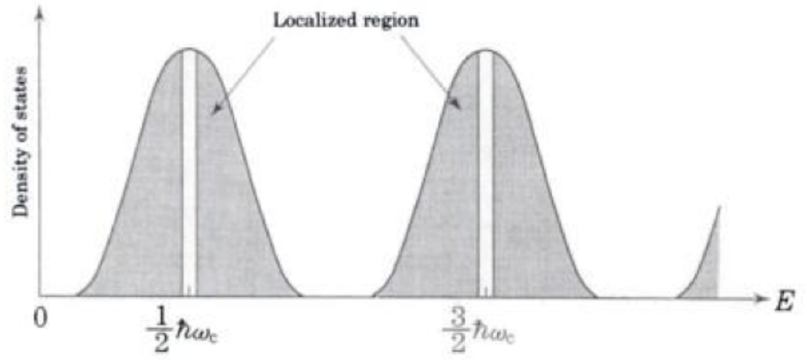

Figure 1.5: Density of states of a system hosting impurities. The Landau levels are broadened by the impurity potential [23].

the localized states, which don't carry current. Thus the Hall resistance remains constant even when the Fermi energy is shifted into the localized states.

1.4 Adiabatic Curvature, Chern Numbers and the Topological Invariant

So far, we have taken a look at the QHE using a gauge invariance argument. It incorporates impurities into the system and can explain edge currents. To understand how topology plays a role in the description of the integer quantum Hall effect, we must first quickly revisit a fundamental concept of geometry: parallel transport. In a flat, Euclidian geometry, the notion of parallel transport is very intuitive, but what if we want to move a vector in a parallel fashion on a curved surface? The best example for such a scenario is the Foucault pendulum. During the 24 hours of a day, the pendulum makes one lateral rotation of 360 degrees. The plane described by the swing of the pendulum defines a certain direction on a to the earth tangential surface. If the pendulum is neither on the equator nor on one of the two poles of earth, after earth having completed a full rotation, the intersection between these two planes will not be the same as in the beginning (see Figure 1.6) [24, 25].

This failure of parallel transport for a closed path, is expressed in the field of differential geometry in terms of a mapping called the connection. In Euclidian space the curvature is simply the second derivative. If, however, we consider a path in a curved space, we cannot build the differential quotient in the same fashion, since derivatives at different points also lie in different vector spaces and we cannot just calculate their difference. To solve this problem, one can define a mapping which connects these different vector spaces, hence the name connection. This notion of curvature lets us introduce the same concept into quantum mechanics [26]. If we describe a physical system that depends on two angular components, by its Hamiltonian $H(\phi,\theta)$, we can associate these two angles with the spherical coordinates of the Earths surface.

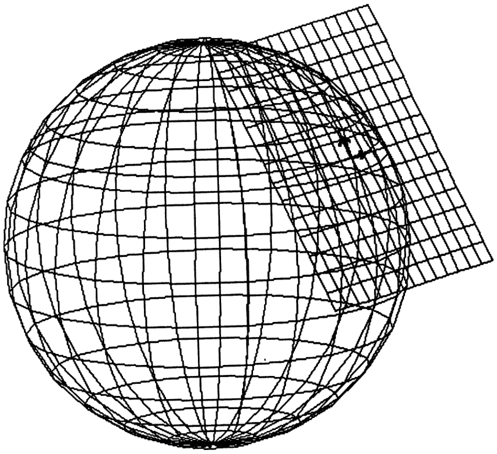

Figure 1.6: Plane of the intersection with the pendulum's swing, tangential to earth's surface [25].

But how can we apply this to the Hall effect? If we can transform our Hamiltonian into the form $H(\phi,\theta)$ so that it depends on two angular components, we can identify the Hall conductance with a curvature.

Let's put this on a more formal ground. We start again from a two-dimensional electron system which is exposed to a magnetic field $B\hat{\mathbf{z}}$, perpendicular to the plane, as well as an in-plane electric field $E\hat{\mathbf{x}}$. To express the Hall current we make use of the Kubo formula which is a general expression for a current, regarded as a linear response to an external field [27]. This method breaks up the expression for the conductivity and then treats one part exactly while approximating the second part.

The Hall current in the y-direction can be written as [27]:

$$\sigma_{xy} = \frac{ie^2\hbar}{L_1L_2}\sum_n \frac{\langle 0|v_1|n\rangle\langle n|v_2|0\rangle - \langle 0|v_2|n\rangle\langle n|v_1|0\rangle}{(E_0-E_n)^2} \tag{1.37}$$

with $|0\rangle$ and $|n\rangle$ denoting the ground state and excited states of the N-electron Hamiltonian

$$H = \sum_{i=1}^{N}\left[\frac{1}{2m_i}\left(-i\hbar\frac{\partial}{\partial x_i}\right)^2 + \frac{1}{2m_i}\left(-i\hbar\frac{\partial}{\partial y_i} - eBx_i\right)^2\right] + \sum_i U(x_i,y_i) + \sum_{j=1}^{N}\sum_i V(|r_i-r_j|) \tag{1.38}$$

and E_0 as well as E_n are the corresponding energies. Here, we have now added to our original Hamiltonian 1.15, a lattice potential $U(x_i,y_i)$ as well as an exchange interaction between the electrons described by V. The velocity operators are:

$$\begin{aligned} v_1 &= \sum_{i=1}^{N}\frac{1}{m_i}\big(-i\hbar\frac{\partial}{\partial x_i}\big) && (1.39)\\ v_2 &= \sum_{i=1}^{N}\frac{1}{m_i}\big(-i\hbar\frac{\partial}{\partial y_i} - eBx_i\big). && (1.40)\end{aligned}$$

Next, we want to think about the boundary conditions to our problem. Given a wave function, delocalized in the x-direction, extended over the length of the square, and localized in the y-direction over the with of the square, we can write, with the Landau gauge fixed [28]:

$$\begin{aligned} \psi(x_i = L_1) &= \psi(0) = 0 && (1.41)\\ \psi(y_i + L_2) &= e^{i\beta L_2}\psi(y_i), && (1.42)\end{aligned}$$

where the wave function, as we have already seen, gains a phase factor while wandering along L_2. The phase parameter β is required to keep total antisymmetry for two states due to the Pauli principle. Since we are only interested in the bulk contribution to the Hall effect we can relax 1.41 to [28]:

$$\psi(x_i + L_1) = e^{i\alpha L_1} e^{i(eB/\hbar)y_i L_1} \psi(x_i). \tag{1.43}$$

We had to introduce a y-dependent factor in 1.43 to keep the Hamiltonian hermitian. If we now apply a unitary transformation on our wave-function, we achieve the angular dependent form, as discussed in the beginning of this section. We can write

$$\gamma_n = \exp[-i\alpha(x_1 + ... + x_N)]\exp[-i\beta(y_1 + ... + y_N)]\psi_n. \tag{1.44}$$

This leads to a transformed Hamiltonian $\tilde{H}$ and we can write for the Hall conductivity

$$\sigma_{xy} = \frac{ie^2}{L_1 L_2 \hbar} \sum_n \frac{\left\langle \gamma_0 \middle| \frac{\partial \tilde{H}}{\partial \alpha} \middle| \gamma_n \right\rangle \left\langle \gamma_n \middle| \frac{\partial \tilde{H}}{\partial \beta} \middle| \gamma_0 \right\rangle - \left\langle \gamma_0 \middle| \frac{\partial \tilde{H}}{\partial \beta} \middle| \gamma_n \right\rangle \left\langle \gamma_n \middle| \frac{\partial \tilde{H}}{\partial \alpha} \middle| \gamma_0 \right\rangle}{(E_0 - E_n)^2} \tag{1.45}$$

where $(1/\hbar)\partial\tilde{H}/\partial\alpha$ and $(1/\hbar)\partial\tilde{H}/\partial\beta$ are the transformed velocity operators. A simple manipulation lets express the conductivity in terms of the partial derivatives of the transformed wave function for the ground state of our two-dimensional system. Furthermore we set $\theta = \alpha L_1$ and $\phi = \beta L_2$, so that we can write

$$\sigma_{xy} = \frac{ie^2}{\hbar}\left(\left\langle \frac{\partial \gamma_0}{\partial \theta} \middle| \frac{\partial \gamma_0}{\partial \phi} \right\rangle - \left\langle \frac{\partial \gamma_0}{\partial \phi} \middle| \frac{\partial . \gamma_0}{\partial \theta} \right\rangle \right). \tag{1.46}$$

So far, we cannot see why the Hall conductance should be quantized. If we assume that there is always a finite energy gap between the ground state and the excitations, independent of the boundary conditions 1.42 & 1.43 and we make the plausible assumption that the bulk conductance, given by the Kubo formalism, should be insensitive to the boundary conditions, as long as the electrons have no long range correlation in the ground state [28] - in short, the Hall conductivity is a local response function - we can average σ_{xy} over all phases $0 \leq \theta \leq 2\pi$ and $0 \leq \phi \leq 2\pi$, that specify different boundary conditions.

$$\bar{\sigma}_{xy} = \frac{e^2}{h} \int_0^{2\pi} \int_0^{2\pi} d\theta d\phi \frac{1}{2\pi i} \left(\left\langle \frac{\partial \gamma_0}{\partial \theta} \middle| \frac{\partial \gamma_0}{\partial \phi} \right\rangle - \left\langle \frac{\partial \gamma_0}{\partial \phi} \middle| \frac{\partial . \gamma_0}{\partial \theta} \right\rangle \right) \tag{1.47}$$

This can be further evaluated, using Stokes' theorem

$$\bar{\sigma}_{xy} = \frac{e^2}{h} \int_0^{2\pi} d\theta \int_0^{2\pi} \frac{d\phi}{2\pi i} \nabla \wedge \zeta = \frac{e^2}{h 2\pi i} \oint_C dl \cdot \zeta \tag{1.48}$$

where ζ is a vector with the components

$$\zeta_l = \frac{1}{2} \left[\left\langle \frac{\partial \gamma_0}{\partial l} \middle| \gamma_0 \right\rangle - \left\langle \gamma_0 \middle| \frac{\partial \gamma_0}{\partial l} \right\rangle \right], \quad l = \theta, \phi. \tag{1.49}$$

Since we know that because of the energy gap the ground state can only change by a phase factor (depending on θ and ϕ), i.e. it must go back to itself (up to an overall phase) as θ and ϕ change by 2π, the integral

$$\oint_C dl \cdot \zeta \tag{1.50}$$

must be equal to $2\pi i \times$ an integer and thus

$$\sigma_{xy} = \text{integer} \times \frac{e^2}{h}. \tag{1.51}$$

The integrand in the contour integral 1.50, is called the Berry connection. As already pointed out in the beginning of this section, the Berry connection is a measure of the change in direction of a vector as a result of a parallel transport. We can identify this mismatch in terms of the curvature of the topology. The curvature itself is directly derived from the connection by

$$K = \nabla \wedge \zeta. \tag{1.52}$$

The Chern theorem states that if we integrate the Berry curvature over a closed manifold without a boundary, it is quantized by 2π, where the quantum number is called the

Chern number. This theorem is a generalization of the theorem of Carl Friedrich Gauss and Pierre Bonnet, to n dimensions. Gauss and Bonnet proved, that for a compact two-dimensional Riemann manifold M with curvature K and boundary ∂M with geodesic curvature k_g, one can connect the geometry of a manifold with its topology

$$\int_M K dA + \int_{\partial M} k_g ds = 2\pi\chi(M). \tag{1.53}$$

The right side of this equation represents a topological invariant called the Euler characteristic and goes back to the Swiss mathematician Leonard Euler who showed in 1758, that for a manifold[1] we can define an even integer g, called genus:

$$\chi(M) = 2 - 2g. \tag{1.54}$$

If we look at 1.53, we need to know that the second summand has to fall off, because our topology - a torus parametrized by the two angular components θ and ϕ - has no boundary [29]. The right hand side in Chern's generalization remains an integer. It is called the Chern number and in contrast to the Euler characteristic, it has no longer to be even. The Chern number is topological in the sense that it stays invariant under small deformations of our Hamiltonian. Such small changes result in changes of the curvature, one might think and therefore in changes of the Chern number. Because the Chern number has to be an integer, it can't change continuously and we can conclude that the graph of the Chern number must show plateaus.

In nuce

So far we have seen that the quantum number of the quantum Hall effect can be interpreted in terms of its underlying Hilbert space topology. Further more, we established

---

[1] if it is oriented

that the quantum number is topological in the sense that the number of electrons that carry conductance in the boundary only depends on the electronic structure of the bulk.

This is a new type of edge state that depends only on the structure of the bulk Hilbert space. Most physical properties dependent on the potentials in the crystal. Here we describe states that are not depended on the potentials at the edge, but only on the topology of the manifold associated with the bulk states. This is a very exciting result that explains the surprising precision with which von Klitzing and many after him could measure the plateau structure of the Hall resistance.

CHAPTER 2

TOPOLOGICAL INSULATOR IN TWO AND THREE DIMENSIONS

2.1 Introduction

In the last chapter we have seen how we can express the Hall conductivity by means of an integral over the local curvature of a manifold. This integral has the form of a topological invariant and introduces the intuitive concept of Chern numbers. What we have to remember is that even though the integrand may be sensitive to smooth deformations of the Hamiltonian, the value of the integral isn't.

In a QH system, the motion of the electrons is explained as a sort of skipping, as their cyclotron orbits bounce off the edge of the Hall band. This motion is chiral in the sense that it can only propagate in one direction along the edge [30]. We have seen that the motion of such edge states is *topologically robust* against impurities, in the sense that there is no way for the electrons to turn back, making the transport dissipantionless. These are quite spectacular properties, but so far we have not talked about any symmetry breaking in connection with the QH state. We have seen in Chapter 1 that the Hall conductivity changes its direction upon a 180° rotation of the magnetic field, in other words, its is odd under a time reversal operation. The spin-orbit (SO) interaction on the other hand, does not break time reversal (TR) symmetry. SO coupling appears in nearly every atom and solid. A given spin leads to a momentum-dependent force on the electron like there would be a local magnetic field:

$$H_{SO} = \lambda \mathbf{L} \cdot \mathbf{S}. \tag{2.1}$$

Since this local "field" is spin dependent it makes the SO coupling transform even under a TR operation. In this chapter we will see a new topological class of materials that is characterized by its TR-invariant behaviour.

2.2 Quantum Spin Hall Effect

In 2006, a new class of topological materials, which are time reversal (TR) invariant and in which spin-orbit coupling (So coupling) would play an important part, had been predicted by Bernevig, Hughes and Zhang [2] and later on observed experimentally [3–5, 31]. The first realization of a 2D topological insulator is the quantum spin Hall (QSH) insulator, which can be understood as two copies of the QH state, that have opposite spin. The states with opposite spin propagate in opposite directions, as schematically illustrated in in Figures 2.1 & 2.2.

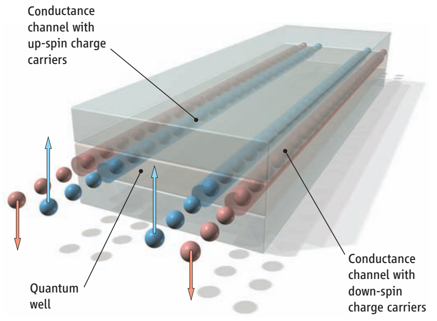

Figure 2.1: Schematic of spin-polarized edge channels in the QSH insulator [3].

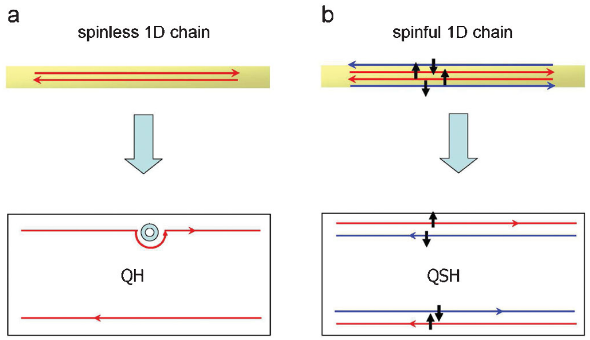

Figure 2.2: Illustration of the spacial separation between a) a forward and a backward mover in the QH state and b) if we include spin we end up with two counter propagating channels of opposite spin on each edge [31].

Bernevig, Hughes and Zhang [2] suggested that a two dimensional QSH insulator could be realized in a HgTe/CdTe quantum well, a sandwich nanostructure as depicted in figure 2.1. They predicted a phase transition, as a function of the quantum well's thickens d_{QW}. If the well is thinner than a critical value d_c, it behaves like a conventional insulator, for $d_{QW} > d_c$, like a QSH insulator with a single pair of helical edge stages, opposite spin states that form a Kramers pair, counter propagating on the same edge. König *et al.*[3] realized experimentally such a time-reversal-invariant QSH system and prooved the existence of 1D gapless edge states, that lie inside the bulk insulating gap and that are topologically protected. These edge states are spin correlated with the direction of motion and appear as predicted in Kramers doublets. TR symmetry ensures the crossing of their energy levels at special points in the Brillouin zone. Due to these level crossings, the band structure of such a QSH insulator cannot be adiabatically deformed into that of a trivial insulator [32].

In an earlier publication [33] it was shown, that the stability of these edge states, depends upon the fact that they appear in odd numbers. On this base, Kane and Mele proposed a classification of TR invariant 2D insulators. All TR invariant insulators fall into two categories, which are classified by a $\mathbb{Z}_2$ topological order parameter. This $\mathbb{Z}_2$ classification is analogous to the Chern number classification for the quantum Hall effect [33]. The $\mathbb{Z}_2$ topological quantum number can be understood in the sense that states with an even number of Krames pairs of edge states, are topologically trivial, while odd numbers of Kramers pairs define topologically non-trivial states (see section 2.7). Experimentally, the $\mathbb{Z}_2$ classification manifests itself in a specific quantized current on the edge [34]. The model by Bevering *et al.*[2], presents a simple formalism for a two-dimensional, time-reversal invariant topological insulator, as it can be realized in a HgTe/CdTe quantum well (QW). If we take a look at the the band structures of the quantum well, as depicted in figure 2.3, we see that all bands close to the Fermi energy, are in vicinity of the Γ point in the Brillouin zone. On the left side of figure 2.3, for the HgTe layer, Γ_6 denotes an s-type band while Γ_8 and Γ_7 denote p-type bands, split by spin-orbit coupling into $J = 3/2$ and $J = 1/2$. CdTe has a s-type (Γ_6) conduction band and p-type valence bands (Γ_8, Γ_7). In a common semiconductor, s-electrons form the conduction band while the valence band is formed by the p-orbitals. However, if spin-orbit coupling is strong enough, it can push the p-band above the s-band as it is the case in heavy elements like Hg and Te. By sandwiching mercury telluride between cadmium telluride, one can realize both types of band structures, depending on the thickness of the HgTe system and thereforee of the strength of spin-orbit coupling.

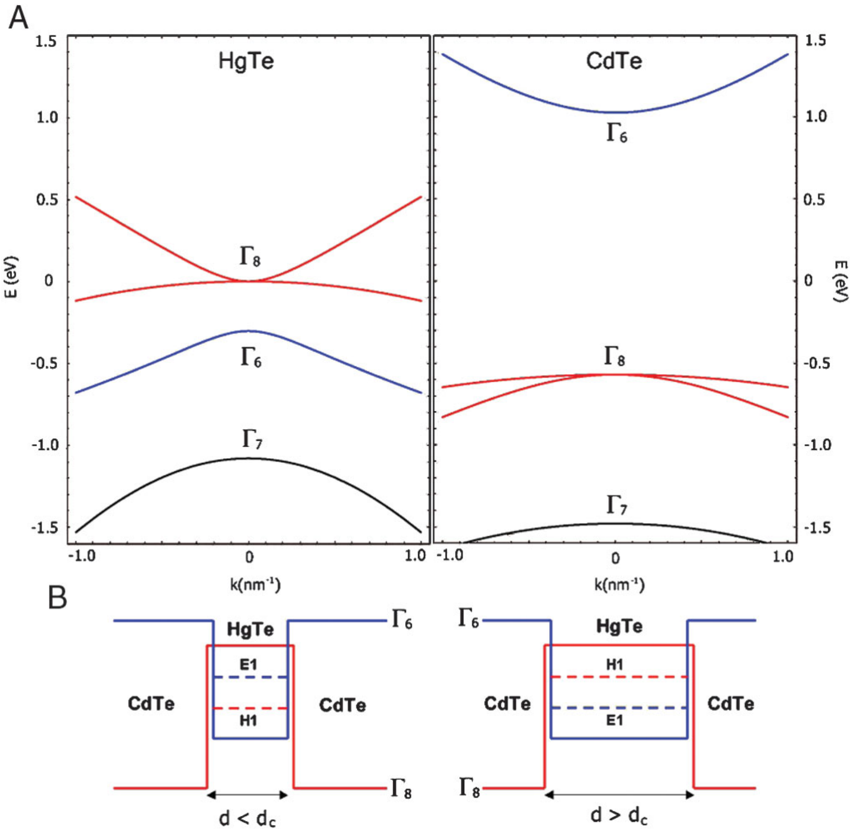

Figure 2.3: (A) Bulk band structure of a HgTe/CdTe well for two different d_{QW}, above and below a critical thickness. (B) Schema of QW with lowest sub-bands for different d_{QW}. The s-like conduction band E1 is located above the p-like valence H1 band for $d < d_c$ and inverted for $d > d_c$ [2].

Figure 2.3 B shows the phase transition as a function of the well's thickness. If the well is wide, we find an inverted band structure, down to a critical value d_c, below which the well behaves like CdTe with a *normal* band order. If the well is wider than this critical value, it behaves more like HgTe, with inverted bands. The question remains, why the QW presents TR invariant, two-dimensional, topologically protected edge states. To answer this question, we take a look at a simple model. We will see, that states at the Γ point, are described by the relativistic Dirac equation. At the critical thickness d_c the effective mass term will change its sign, leading to two distinct $U(1)$-spin and $\mathbb{Z}_2$ topological numbers, on either side of the transition (see Section 2.7).

Due to the TR invariant nature of the Dirac equation, it has doubly degenerated eigen solutions, which are referred to as Kramers pairs. We start with defining a basis for our problem, where we neglect the Γ_7 band due to its minor relevance for effects on the band structure [2]. We have thereforee 6 basic states per unit cell:

$$\{|\Gamma_6, 1/2\rangle, |\Gamma_6, -1/2\rangle, |\Gamma_8, 3/2\rangle, |\Gamma_8, 1/2\rangle, |\Gamma_8, -1/2\rangle, |\Gamma_8, -3/2\rangle\}. \tag{2.2}$$

where $|\Gamma_x, \pm m_j\rangle$ denote two sets of Kramers partners with opposite parity. We set the growth direction as the z-axis, with the spherical symmetry broken down, to axial rotation in plane, perpendicular to the growth direction. The six bands form the spin-up and spin-down states of three QW sub-bands, we call them E_1, H_1 and L_1. The L_1 sub-band is well separated from the other two, thus we neglect it [2]. At the Γ point, we have an in-plane momentum of $k_{\|} = 0$, m_j remains a good quantum number. We need two basis sets, for two bands

$$|E_1, m_j\rangle \quad : \quad \{|\Gamma_6, \pm 1/2\rangle, |\Gamma_8, \pm 1/2\rangle\} \tag{2.3}$$

$$|H_1, m_j\rangle \quad : \quad \{|\Gamma_8, \pm 3/2\rangle\}. \tag{2.4}$$

Away from this point, E_1 and H_1 states can mix. To find the corresponding matrix element, let's take a look at the parity of the different states. $|\Gamma_6, m_j = \pm 1/2\rangle$ states have even parity, while $|\Gamma_8, m_j = \pm 3/2\rangle$ have odd parity under in-plane reflection. We conclude that the matrix element, that couples these two states, must be an odd function of in-plane momentum k. On this ground, we can model an effective Hamiltonian for the E_1 and H_1 states, using the basis:

$$\{|E_1, m_j = 1/2\rangle, |H_1, m_j = 3/2\rangle, |E_1, m_j = -1/2\rangle, |H_1, m_j = -3/2\rangle\}, \tag{2.5}$$

where $|E_1, \pm\rangle$and $|H_1, \pm\rangle$ are two sets of Kramers partners. The states $|E_1, \pm\rangle$and $|H_1, \pm\rangle$

have opposite parity, thereforee a matrix element coupling them, must be an odd function under parity [32]. To lowest order in k, ($|E_1,+\rangle$,$|H_1,+\rangle$) and ($|E_1,-\rangle$,$|H_1,-\rangle$) will each be coupled via a term linear in k. We call $|H_1,+\rangle$, the heavy hole state, that is formed from the p-orbitals $|p_x+ip_y,\uparrow\rangle$ and $|H_1,-\rangle$ the heavy hole state that is formed from the p-orbitals $|p_x+ip_y,\downarrow\rangle$. thereforee, to preserve rotation symmetry around the growth axis, the matrix elements must be proportional to $k_x \pm ik_y$. For each k, the sub-bands must be two-fold degenerate, so there can be no matrix elements mixing the + and the - state within one band. These arguments lead to the following model:

$$H_{\text{eff}}(k_x,k_y) = \begin{pmatrix} \hat{H}(k) & 0 \\ 0 & \hat{H}^*(-k) \end{pmatrix} \tag{2.6}$$

$\hat{H}^*(-k)$ is unitarily equivalent to $\hat{H}^*(k)$, where $\hat{H}^*(-k)$ is determined from time-reversal symmetry [2].

$$\hat{H}(k) = \varepsilon(\mathbf{k})\mathbb{I}_{2\times 2} + d_i(k\mathbf{k})\sigma_i, \tag{2.7}$$

with σ_i representing the Pauli matrices. If we take the above expression to the lowest order of k, one can deduce that, due to the symmetry arguments given above, $d_3(k)$ is an even function of k while $d_1(k)$ and $d_2(k)$ are odd. We can expand them to lowest order in k, as follows [2]:

$$\begin{aligned} d_1 + id_2 &= A(k_x+ik_y) \equiv Ak_+ \quad (2.8)\\ d_3 &= M - B(k_x^2+k_y^2) \quad (2.9)\\ \varepsilon(\mathbf{k}) &= C - D(k_x^2+k_y^2), \quad (2.10)\end{aligned}$$

with A,B,C and D representing system dependent parameters. Equation 2.7 is equivalent to a (2+1) dimensional Dirac hamiltonian. The parameter M in equation 2.9, plays the important role, of describing the difference in energy between the E_1 and H_1 bands at the

Γ-point[1] and can thereforee be interpreted as gap parameter which changes sign at the critical thickness of the well. For $d_{QW} > d_c$, the level E_1 falls under the H_1 level and M becomes negative. With the parameter C, we can tune the top of the bulk valence band of HgTe to 0 and the parameter B describes the mass term in the quadratic regime of the dispersion relation (Newtonian mass term). We will see later on, that the relative sign between the parameter M and B plays an important role in the determination, whether we describe a topological insulator state with protected edge states or a common insulator.

2.3 Edge states

In our description of the QH state, we have shown the existence of current-carrying edge states. Historically, one of the motivations behind the discovery of the 2D topological insulator was the search for similar edge states, existing in a system that would not depend on a strong magnetic field. With the formalism that was reviewed above, we are now able to obtain these states by solving equation 2.7. Bernevig, Hughes and Zhang [2] used a tight-binding model for the E_1 and H_1 states, based on their symmetry properties in a square lattice, with four states per unit cell. Considering nearest-neighbour interactions only, results in a Hamiltonian of the form of equation 2.6 with the simplified matrix elements:

$$\begin{aligned} d_1 &= A\sin(k_x) && (2.11)\\ d_2 &= -A\sin(k_y) && (2.12)\\ d_3 &= -2B[2-(M/2B)-\cos(k_x)-\cos(k_y)] = M(\mathbf{k}) && (2.13)\\ \varepsilon(\mathbf{k}) &= C-2D[2-\cos(k_x)-\cos(k_y)]. && (2.14) \end{aligned}$$

---

[1] since all the interesting physics happens near the Γ-point and we are not interested in the dispersion at higher energies than the bulk gap at the Γ-point.

For simplicity reasons, the lattice constant is assumed to be 1. If we further constrain $x > 0$, we can divide the Hamiltonian into two parts

$$\hat{H} = \tilde{H}_0 + \tilde{H}_1 \tag{2.15}$$

with

$$\tilde{H}_0(k_x) = \tilde{\varepsilon}(k_x) + \begin{pmatrix} \tilde{M}(k_x) & Ak_x & 0 & 0 \\ Ak_x & -\tilde{M}(k_x) & 0 & 0 \\ 0 & 0 & \tilde{M}(k_x) & -Ak_x \\ 0 & 0 & -Ak_x & -\tilde{M}(k_x) \end{pmatrix} \tag{2.16}$$

and

$$\tilde{H}_1(k_y) = -Dk_y^2 + \begin{pmatrix} -Bk_y^2 & iAk_y & 0 & 0 \\ -iAk_y & Bk_y^2 & 0 & 0 \\ 0 & 0 & -Bk_y^2 & iAk_y \\ 0 & 0 & -iAk_y & Bk_y^2 \end{pmatrix} \tag{2.17}$$

with $\tilde{\varepsilon}(k_x) = C - Dk_x^2$ and $\tilde{M}(k_x) = M - Bk_x^2$, all k_x dependent terms are included in $\tilde{H}_0$. Because of our restriction $x > 0$, we deal with a semi-infinite system and we have to replace k_x by the operator $-i\partial_x$ [32] (since the wave function can extend over the system). In the y- direction, translational symmetry is preserved, so that we can choose k_y as quantum number. Since we are interested in solutions at the edge, we can set $k_y = 0$ and find $\tilde{H}_1 = 0$. The wave equation is then given by

$$\tilde{H}_0(-i\partial_x)\Psi(x) = E\Psi(x). \tag{2.18}$$

The eigenstates will have a simple form, due to the block diagonal structure of $\tilde{H}_0$:

$$\Psi_\uparrow(x) = \begin{pmatrix} \psi_0 \\ \mathbb{O} \end{pmatrix} \tag{2.19}$$

$$\Psi_\downarrow(x) = \begin{pmatrix} \mathbb{O} \\ \psi_0 \end{pmatrix}. \tag{2.20}$$

Equation 2.18 has been solved analytically, using different methods [35–37]. The general solution is given by

$$\psi_0(x) = (ae^{\lambda_1 x} + be^{\lambda_2 x})\phi_- + (ce^{-\lambda_1 x} + de^{-\lambda_2 x})\phi_+, \tag{2.21}$$

where $\phi_\pm$ is an eigenstate of the Pauli matrix σ_2. $\lambda_{1,2}$ has to satisfy:

$$\lambda_{1,2} = \frac{1}{2B}\big(A \pm \sqrt{A^2 - 4MB}\big). \tag{2.22}$$

The coefficients a, b, c and d can be determined by enforcing the open boundary condition $\psi(0) = 0$. This on the other hand, leads to a further condition for the existence of edge states [32]:

$$\mathrm{Re}\lambda_{1,2} < 0 \leftrightarrow c = d = 0 \text{ and } \mathrm{Re}\lambda_{1,2} > 0 \leftrightarrow a = b = 0. \tag{2.23}$$

It is important to notice, that 2.22 allows these conditions only to be satisfied in the inverted band regime, when $M/B > 0$. This is the change in sign of the effective mass term, that describes the phase transition and was already mentioned in the last section. Another important consequence of $\mathrm{Re}\lambda_{1,2} < 0$ is $A/B < 0$, while $\mathrm{Re}\lambda_{1,2} > 0$ leads to $A/B > 0$. Summarizing, we can write for the wave function of the two edge states (one for each spin) at the Γ-point,

$$\psi_0(x) = \left\{ \begin{array}{ll} a(e^{\lambda_1 x} - e^{\lambda_2 x})\phi_-, & A/B < 0 \\ c(e^{-\lambda_1 x} - e^{-\lambda_2 x})\phi_+, & A/B > 0 \end{array} \right\}, \tag{2.24}$$

where the sign of A/B determines the spin polarization of the edge states, and $l = \max|\mathrm{Re}\lambda_{1,2}|^{-1}$ is their decay length [32], .

To obtain edge states, we have solved the effective Hamiltonian on the boundary of the system. We can thereforee also write down a specific Hamiltonian for these edge states, by projecting the bulk Hamiltonian onto them. We have $\Psi_\uparrow$ and $\Psi_\downarrow$ as defined in equation 2.20, so we write:

$$H^{\alpha\beta}_{edge}(k_y) = \langle\Psi_\alpha|\tilde{H}_0 + \tilde{H}_1|\Psi_\beta\rangle\,. \tag{2.25}$$

To first order in k_y this is

$$H_{edge} = Ak_y\sigma^z. \tag{2.26}$$

Further, it is also interesting to see how the well behaves, when it has exactly the critical thickness d_c, where the topological quantum phase transition occurs. In this case the effective mass term becomes zero and a massless Dirac fermion state is realized, showing both spin orientations. The existence of massles Dirac fermions in HgTe quantum-wells was experimentally proved by Bütter *et al.* in 2010 [38].

The biggest difference between edge states in the QH effect that we have discussed in the last chapter, and the wave functions for the states at the edge of a QSH system, is obviously the fact that for the latter spin plays an important role. Before we move on to three dimensional topological insulators, we have to take a look at the consequences of spin-orientation dependence in the QSH effect.

It has been shown [39], that edge states with opposite spin counter-propagate. We have seen in the first chapter, that for the QH system, edge states cannot be backscattered if the sample width is larger that the decay length of the edge states. This suggests the following question: is backscattering possible for the spin polarized edge states of our QW system? To answer this question in full, let us first take a look at a semi-classical analogy that can be found in today's glasses that we wear to correct limitations in sight, or to protect our eyes from sunlight. Such glasses are equipped with anti-reflective coating which guarantees perfect transmission. The coating works in a way, that reflections on the top and bottom surfaces interfere destructively, resulting in a better sight. Turning back to our solutions for edge states, given by equation 2.24, if they encounter a non-magnetic impurity, it can cause backscattering (due to So coupling). A right-moving spin-$\uparrow$ electron is backscattered by an impurity along a clockwise path into a left moving spin-$\downarrow$ electron. In this process it will pick up a phase of π, due to TR symmetry. A right moving spin-$\uparrow$ electron also picks up a phase, in this case $-\pi$, traveling along a counterclockwise path. This results in a difference for the two paths of a $\pi-(-\pi)=2\pi$ rotation of the spin, and the two reflected electrons would interfere destructively with each other[2], allowing perfect transmission (see Fig. 2.4). This effect is referred to as *protection by time-reversal symmetry*, pointing out that only in a time reversal symmetric system, like for Dirac particles, this destructive interference is assured.

Another characteristic property of topological insulators can be derived from backscattering. If we assume four scatterers, a left-moving spin-$\uparrow$ electron can then scatter into the right-moving spin-$\uparrow$ channel without picking up a phase difference, which allows it to interfere destructively. This odd-even effect was pointed out by Qi and Zhang [34]. It expresses the fact that, for the QSH effect to be robust against impurities, we need an odd number of forward (backward) movers, which ties directly to the Z_2 topological number[3]. One must also note that, if an electron encounters a magnetic impurity, TR symmetry is broken and destructive interference is no longer assured.

---

[2] A spin-$1/2$ particle picks up a negative sign under a 2π spin rotation, thereforee we are assured that two backscattering electrons related by TR symmetry, always interfere destructively

[3] See Section 2.7

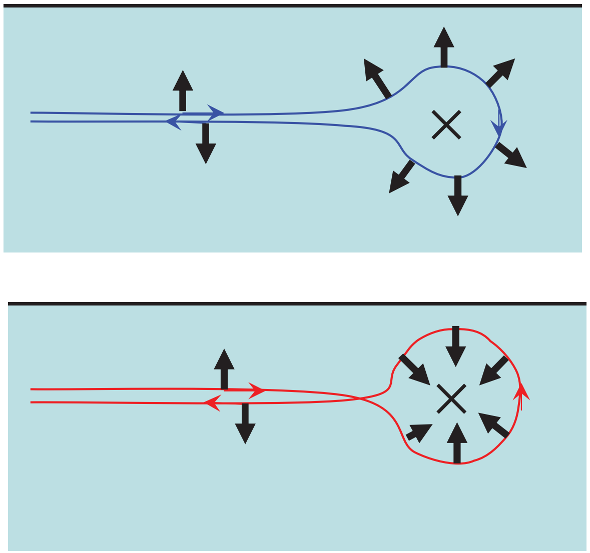

Figure 2.4: Spin-↑ electron will pick up a phase of π while a spin-↓ electron picks up $-\pi$ resulting in a total phase of 2π, which leads to destructive interference.[31].

2.4 Experimental realization of the HgTe/CdTe quantum well

In 2007 König *et al.*published results of transport measurements in HgTe/CdTe quantum well devices that could reproduce theoretical predictions [40]. In their experiment they used several devices, fabricated by molecular beam epitaxy, of different widths, ranging from 5.5nm $(d < d_c)$ to 12nm $(d > d_c)$. They fabricated several devices in Hall bar geometry (see inset of Figure 2.5), with a 110nm Si_3N_4/SiO_2 insulating layer toped with a Ti/Au gate. Transport measurements where carried out in a ^{3}He/^{4}He dilution refrigerator and in a ^{4}He cryostat fitted with a vector magnet.

Figure 2.5 shows the zero B-field four terminal resistance $R_{14,23} = V_{23}/I_{14}$ as a function of normalized gate voltage (V_{thr} is defined as the voltage for which the resistance is largest).

$R_{14,23}$ is measured while the Fermi level in the device is scanned through the gap. Curve I was obtained from a $(20 \times 13.3)\mu m^2$ device with $d_{QW} < d_c$ and shows a resistance of the order of $M\Omega$ as expected from an insulator. Measurements II-IV show wells of different sizes in the inverted regime with resistances below 100 $k\Omega$. The green and the red curve represent shorter samples of about $1\mu m$ length and reach the predicted value close to $2e^2/h$ demonstrating the existence of the QSH insulator state in the inverted regime of the well.

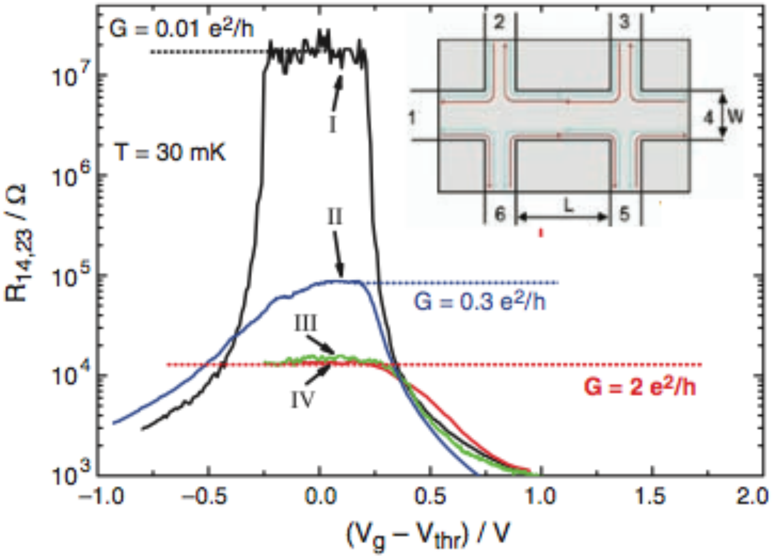

Figure 2.5: Resistance of quantum wells in different regimes. In I the well is wider than d_c, II-IV shows wells of different sizes in the inverted state, with $d < d_c$ [40].

2.5 Topological insulator in three dimensions

Later in 2006 theorists [41–43] started to develop a formalism for a 3D realization of the topological insulator. The first idea was a sort of staking of QSH insulators, in the same manner as the step from the QH state to the QSH state was realized. The physics of this weak three-dimensional topological insulator, turned out to be generally similar to the 2D version, in the sense that one obtains 2D topological insulator behaviour in a 3D material.

There exists however also a strong topological insulator, on which we will focus in this chapter. Also in the case of strong topological insulators we use the HgTe QW, as a basic template and generalize it to 3D. We can use our knowledge from the last chapter to build a model Hamiltonian for a class of materials with a rather simple structure. In this chapter, we will focus on the materials Bi_2Se_3, Bi_2Te_3 and Sb_2Te_3. Similar as for the QW system, spin-orbit coupling plays an important role in these materials, resulting in a band inversion at the Γ-point. In a 3D topological insulator we have a fully gapped bulk regime and one topologically protected surface state, a massless Dirac fermion. This fermion is helical in the sense that its spin points perpendicular to its momentum, forming a left handed helical system in momentum space. Again, this surface state is protected by TR symmetry, in the sense that only a TR-symmetry-breaking perturbation can open a gap on the surface.

2.6 Effective Hamiltonian in 3D

The effective model we will focus on in this chapter, was developed in 2009 by H. Zhang *et al.*[44]. The model is adjustable for the family of compounds named in the introduction to this chapter, only by changing parameters. At the beginning of their search for a 3D system, they focused on compounds where the conduction and valence bands have opposite parities and a band inversion can occur, as a function of spin-orbit coupling. The family Bi_2Se_3, Bi_2Te_3 and Sb_2Te_3 share the same rhombohedral crystal structure with space group $D^5_{3d}(R\bar{3}m)$, carrying five atoms per unit cell.

As an example candidate, we will take Bi_2Se_3. The structure of Bi_2Se_3 is depicted in figure 2.6. Within one quintuple layer of the material, the bonding is strong between two atomic layers, but of nearly pure van-der-Waals type between two quintuple layers. Because the Se2 site acts as an inversion centre between the sites Bi1/Se1 and Bi1'/Se1', we can construct eigenstates for this system with definite parity [44].

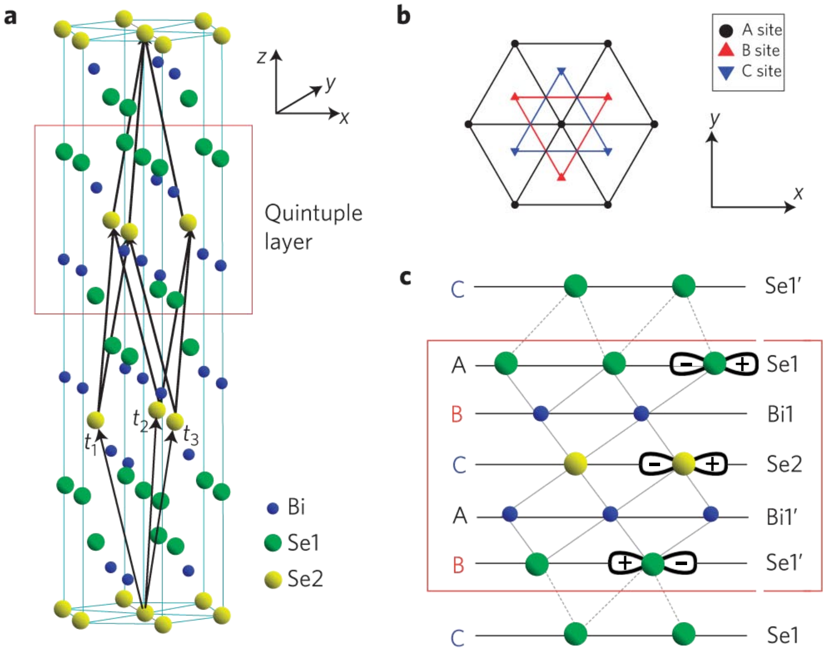

Figure 2.6: a) Layered structure of Bi_2Se_3, the red square indicates a quintuple layer. b) Trigonal structure within one layer. c) Stacking of the crystal along the z-axis. The Se1/Bi1 is related to the Se1'/Bi1' layer by inversion symmetry [44].

Zhang *et al.*performed *ab initio* calculations, using the generalized gradient functional of Perdew-Burke-Ernzerhof, to analyze the band structure of the crystal. They noted an energy gap of 0.3eV which is in good agreement with experimental data ($0.2-0.3$eV) [44]. Figure 2.7 shows the calculated band structure without and with So coupling.

If we compare the two figures, we can make out a qualitative change near the Γ-point.

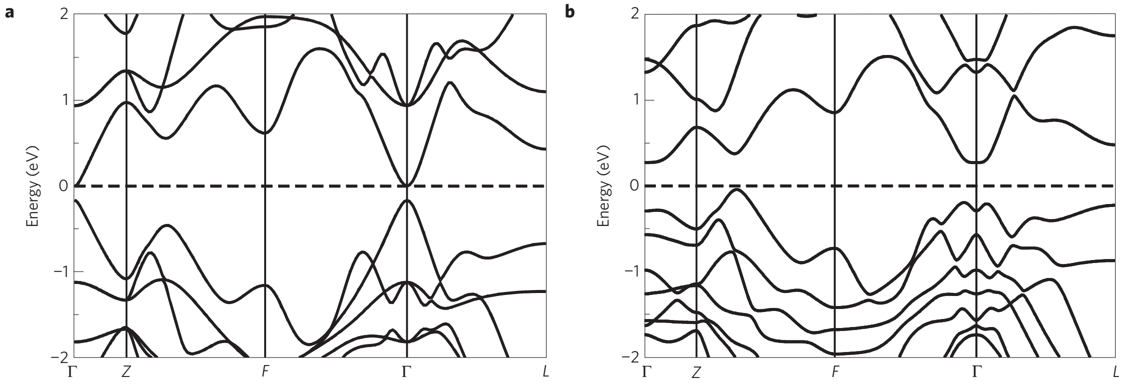

Figure 2.7: Ab initio calculation of band structure of Bi_2Se_3 a) without and b) with spin-orbit coupling. The dashed line denotes the Fermi energy [44].

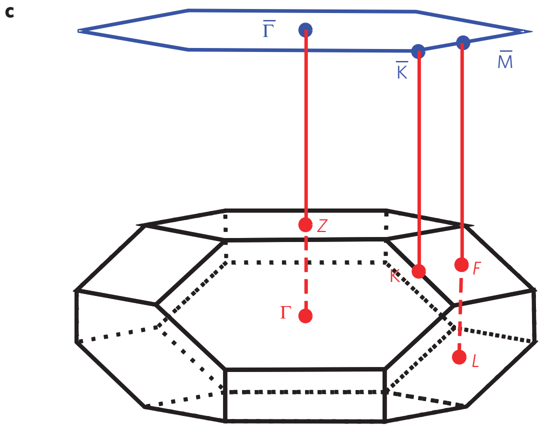

Figure 2.8: Brillouin zone of Bi_2Se_3. The blue hexagon shows the projection of the Brillouin zone in which the high-symmetry points $\bar{\Gamma}$, $\bar{K}$ and $\bar{M}$ are labelled [44].

It seems that turning on So coupling, results in an anti-crossing feature around this point. Figure 2.7 a) shows how close the valence band approaches the conduction band at the Γ-point. In Figure 2.7 b) the two bands will overlap and due to the additional spin-orbit potential, a gap opens and lifts the degeneracy where the bands cross. To establish a firm proof for the topological nature of the crystal, Zhang *et al.* calculated the parities of the states at the time-reversal invariant Γ-point, as well as at the three inequivalent time-reversal-invariant points $L(\pi,0,0)$, $F(\pi,\pi,0)$ and $Z(\pi,\pi,\pi)$. They found that the parity changed on turning on So coupling, of one occupied band, at the Γ-point. The parity of all occupied bands remained unchanged at the other momenta F, L, Z. This indication of a band swap, suggest that Bi_2Se_3 is in fact a topological insulator. To better understand the inversion of bands, take a look at figure 2.9.

We start with the electron configuration of Bismuth: [Xe]$4f^{15}5d^{10}6s^26p^3$, and Selenium:

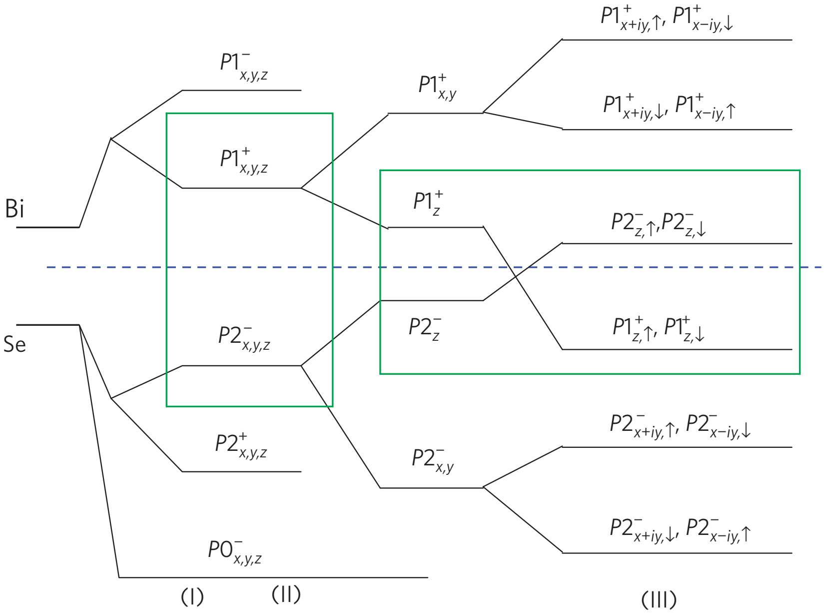

Figure 2.9: Schematic diagram for the evolution of the atomic orbitals close to the Fermi energy. (I) Chemical bonding, (II) crystal-field splitting and (III) effects of So coupling. [44]

[Ar]$3d^{10}4s^24p^4$. The conduction and valence bands are formed from states close to the Fermi energy, we are thereforee interested in the *p*-orbitals and will neglect the effects of the *s*-orbitals. The first stage (I) in figure 2.9, shows the recombination of the *p*-orbitals, according to their parity (calculated by [44]). Bonding of the states results in hybridization, lowering all Se states, while lifting up all Bi states. If we go back to figure 2.6 c) and imagine *p*-shaped orbitals at each Bi and Se site in the primitive cell, denoted by the red rectangle, we see that due to inversion symmetry, we can group all orbitals due to their parity. This results in two odd, $|P2^-/P0^-_{x,y,z}\rangle$ and one even state $|P2^+_{x,y,z}\rangle$, for each Se atom and one odd and one even $|P1^\pm_{x,y,z}\rangle$, for each Bi site (the sign denotes the parity of the states). As an example I have drawn in figure 2.6 c) the orbitals on two Se atoms that are connected by a third Se atom, which acts as an inversion centre. The example shows the case of an odd - even combination. Stage (II) describes crystal-field effects, between different p-orbitals. According to the point-group symmetry, the p_z orbital is split from the p_x and p_y orbitals, leaving the last two degenerate [44]. We are left with the states $|P1^+_{x,y}\rangle$, $|P1^+_z\rangle$, $|P2^-_z\rangle$ and $|P1^-_{x,y}\rangle$. We see that $|P1^+_z\rangle$ and $|P2^-_z\rangle$, are the closest to the Fermi energy. In stage (III) we turn on So coupling, which we describe by the Hamiltonian $H_{\mathrm{SO}} = \lambda \mathbf{l} \cdot \mathbf{S}$, with l and S being the orbital and spin angular momentum and λ is the So coupling parameter. By mixing spin and orbital angular momenta but preserving their total J, this Hamiltonian leads to a level repulsion between $|P1^+_z, \uparrow\rangle$ and $|P1^+_{x+iy}, \downarrow\rangle$ and similar combinations. This repulsion can be understood, by rewriting the SO Hamiltonian. Because we can write $J^2 = J \cdot J = (l+S)(l+S) = l^2 + S^2 + 2l \cdot S$, it follows that $H_{\mathrm{SO}} = 1/2\lambda(J^2 - l^2 - S^2)$. For $J = 3/2$, we get the state $|l = 1, \uparrow\rangle$, for $J = 1/2$ we get the sates $|l = 1, \downarrow\rangle$ and $|l = 0, \uparrow\rangle$. The first two cases must be in the xy-plane, where we have rotational symmetry ($l = 1$): P_{x+iy}. The other case is out of plane, along the z-direction P_z, where $l = 0$.

As a consequence of this repulsion, the $|P1^+_z, \uparrow(\downarrow)\rangle$ state is pushed down while the $|P2^-_z, \uparrow(\downarrow)\rangle$ state is pushed up. The inversion of this two bands can therefore be modelled as a function of the parameter λ. Calculations by [44] have revealed, that the critical value λ_c, for band inversion to take place, lies around 60% of the real So coupling value. Since the swapping states have opposite parity, we find the same mechanism as in the 2D quantum well system described in the last chapter.

2.6.1 Surface states

Due to the similarities between the 2D and the 3D topological insulator, we can generalize our results from the last chapter. We know from *ab initio* calculations, that the interesting physics happens around the Γ-point, where the band inversion occurs and the topological nature of our compound is determined. If one again tries to sketch out a simple Hamiltonian, to characterize the properties of this system, one has to start from our four states $|P1_z^+, \uparrow(\downarrow)\rangle$ and $|P2_z^-, \uparrow(\downarrow)\rangle$. The formalism behind finding the correct Hamiltonian is called, *theory of invariants* and is described here [45]. Our system has the following symmetries:

- time-reversal symmetry Θ
- inversion symmetry I
- C_3 rotation symmetry along the z-axis

In the basis of our four states, we can represent these symmetry operations as [44]:

$$\Theta = K \cdot i\sigma^y \wedge \mathbb{I}_{2\times 2} \tag{2.27}$$

$$I = \mathbb{I}_{2\times 2} \wedge \tau_3 \tag{2.28}$$

$$C_3 = \exp(i\frac{\pi}{3})\sigma^z \wedge \mathbb{I}_{2\times 2}, \tag{2.29}$$

where K is the complex conjugation operator and σ and τ denote the Pauli matrices in the spin and orbital space. By demanding these symmetries from the system and keeping only terms up to quadratic order in $\mathbf{k}$, one can write the effective Hamiltonian according to [32] as:

$$H(\mathbf{k}) = \varepsilon_0(\mathbf{k})\mathbb{I}_{4\times 4} + \begin{pmatrix} \mathfrak{M}(\mathbf{k}) & A_1 k_z & 0 & A_2 k_- \\ A_1 k_z & -\mathfrak{M}(\mathbf{k}) & A_2 k_- & 0 \\ 0 & A_2 k_+ & \mathfrak{M}(\mathbf{k}) & -A_1 k_z \\ A_2 k_+ & 0 & -A_1 k_z & -\mathfrak{M}(\mathbf{k}) \end{pmatrix} + \mathbb{O}(\mathbf{k^2}), \tag{2.30}$$

with $k_\pm = k_x \pm ik_y$, $\varepsilon_0(\mathbf{k}) = C + D_1 k_z^2 + D_2 k_\perp^2$ and $\mathfrak{M}(\mathbf{k}) = M - B_1 k_z^2 - B_2 k_\perp^2$. The parameters used, are then determined by fitting the energy spectrum of the Hamiltonian to *ab initio* calculations [31, 44]. Next, we again split the Hamiltonian, identical to Equation 2.15

$$\hat{H} = \tilde{H}_0 + \tilde{H}_1. \tag{2.31}$$

For the half space $z > 0$ we get

$$\tilde{H}_0 = \tilde{\varepsilon}(k_z) + \begin{pmatrix} \tilde{M}(k_z) & A_1 k_z & 0 & 0 \\ A_1 k_z & -\tilde{M}(k_z) & 0 & 0 \\ 0 & 0 & \tilde{M}(k_z) & -A_1 k_z \\ 0 & 0 & -A_1 k_z & -\tilde{M}(k_z) \end{pmatrix} \tag{2.32}$$

and

$$\tilde{H}_1 = -D_2 k_\perp^2 + \begin{pmatrix} -B_2 k_\perp^2 & 0 & 0 & A_2 k_- \\ 0 & B_2 k_\perp^2 & A_2 k_- & 0 \\ 0 & A_2 k_+ & -B_2 k_2 k\perp^2 & 0 \\ A_2 k_+ & 0 & 0 & B_2 k_\perp^2 \end{pmatrix}, \tag{2.33}$$

with $\tilde{\varepsilon}(k_z) = C + D_1 k_z^2$ and $\tilde{M}(k_z) = M - B_1 k_z^2$. We see that $\tilde{H}_0$ in 2.15 is identical to 2.31, up to the replacement of the parameters A, B, C, M with A_1, B_1, C, D_1 and M. For a surface perpendicular to the z-direction, we can use k_x and k_y as quantum numbers, but k_z we have to replace in equation 2.31, on the same grounds as for the QSH system, with $-i\partial_z$. We conclude that the edge states at $k_x = k_y = 0$ are described by the same equation as for the QSH system. Again a surface solution exists in the regime $M/B_1 > 0$, and also the helicity of the surface state is determined in the same way, by the sign of A_1/B_1. For $k_x = k_y = 0$, there exists two surface states on the half-infinite space $z > 0$: $\Psi_{0,\uparrow}$ and $\Psi_{0,\downarrow}$. In the same manner as we have obtained equation 2.26, by projecting the bulk Hamiltonian onto the surface states, we can obtain a surface Hamiltonian for the 3D topological insulator. To leading order in k_x and k_y, this results in [32]:

$$H_{\text{surf.}}(k_x, k_y) = C + A_2(\sigma^x k_y - \sigma^y k_x), \tag{2.34}$$

where the surface state wave function $\Psi_{0,\uparrow(\downarrow)}$ is a superposition of the $|P1_z^+, \uparrow(\downarrow)\rangle$ and $|P2_z^+, \uparrow(\downarrow)\rangle$ states.

2.7 A word on topological invariants

In the beginning of this chapter we have already mentioned the $\mathbb{Z}_2$ topological index and how it stands in relation with the appearance of an even or odd number of Kramers partners, let us take a more precise look at this new topological quantum number. First we go back to the operator that describes a TR operation (Equation 2.27), but write it in exponential form:

$$\Theta = \exp(i\pi\sigma^y/2)K = \exp(i\pi S_y/\hbar)K. \tag{2.35}$$

Here S_y represents the y-component of the spin operator and K denotes as before, complex conjugation. For a physical system to be symmetric under a TR operation means that its Hamiltonian operator has to commute with Θ, i.e. for every eigenstate, the time-reversed state is also an eigenstate with the same energy. One might argue that the time-reversed state is identical with the original state, but if we have a half-integer spin system at hand this is no longer possible since equation 2.35 reverses all angular momenta and reversing a half integer spin cannot yield an identical state because the magnetic quantum number is never zero. This is exactly the statement of Kramers degeneracy theorem. In the absence of spin-orbit coupling Kramers theorem simply expresses the degeneracy between up and down spins, in the presence of spin-orbit interactions however, it has nontrivial consequences [5, 46].

On a 2-D square lattice we find four time-reversal-invariant points (8 for a 3-D qubic lattice). With a reciprocal lattice vector $\mathbf{G}$ we can write for these points [47]:

$$-\Gamma_i = \Gamma_i + n_i\mathbf{G}, \tag{2.36}$$

with $n_i = 0, 1$. We can thereforee write for the points $\Gamma_i = n_i\mathbf{G}/2$: [47]:

$$H(\Gamma_i) = \Theta H(\Gamma_i)\Theta^{-1}. \tag{2.37}$$

In accordance with Kramers theorem all eigenvalues of this Hamiltonian are at least doubly degenerate. If an insulator further has inversion symmetry;

$$H(-\mathbf{k}) = IH(\mathbf{k})I^{-1}, \tag{2.38}$$

where I (Eq. 2.28) denotes the parity (inversion) operator $I\,|\mathbf{r}, s_z\rangle = I\,|-\mathbf{r}, s_z\rangle$ changing the sign of the coordinates but leaving the spin unchanged because it is a pseudo-vector. If we combine TR symmetry and inversion symmetry, the Berry curvature must vanish because it is odd under TR and even under inversion [46]. If we consider the m-th pair of occupied

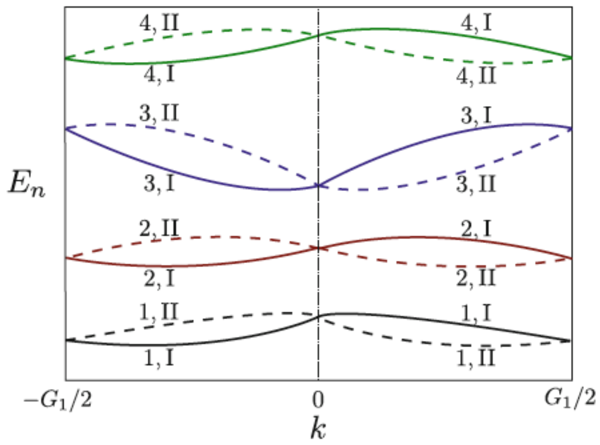

Figure 2.10: Structure of bands along one reciprocal lattice vector. Kramers pairs at $k = 0, G_1/2$ [46]

energy bands at the TR symmetry points in k-space Γ_i (see Fig: 2.10) for a 1-D model, we can define the parity eigenvalues $\xi_{2m}(\Gamma_i) = \pm 1$ through the eigenwert problem:

$$I\,|u_{2m,\Gamma_i}\rangle = \xi_{2m}(\Gamma_i)\,|u_{2m,\Gamma_i}\rangle\,. \tag{2.39}$$

At the TR symmetric points Γ_i, degenerate Kramers partners share the same eigenvalue, $\xi_{2m} = \xi_{2m-1}$ and the $\mathbb{Z}_2$ index $\nu = \pm 1$ is determined by the equation:

$$(-1)^{\nu} = \prod_{i} \prod_{m=1}^{N} \xi_{2m}(\Gamma_i), \tag{2.40}$$

N being the total of pairs of degenerate eigenstates.

CHAPTER 3

ANTIFERROMAGNETIC TOPOLOGICAL INSULATOR

3.1 Introduction

In the following three chapters we will take the models and methodologies introduced so far, but go one step further and ask the question if topological order can coexist with a broken symmetry state. More specifically, if it is possible that a local order parameter which breaks one or more symmetries can give rise to topological order? The answer to this question, theoretically, is a tentative ‘yes’ [48, 49].

After taking a look at the theoretical foundation of the antiferromagnetic topological insulator (AFTI), we turn to two magnetic half-Heusler compounds of the *RE*BiPt family. Half-Heusler materials qualify for this new phase of matter, depending on the type of magnetic order they present.

3.2 Magnetically induced spin-orbit coupling

In 2010 Mong *et al.*[48] came forward with the concept of an antiferromagnetic topological insulator. In contrast with an *ordinary* topological insulator, in an AFTI the presence of magnetic order breaks TR symmetry Θ as well as primitive-lattice translational symmetry $T_{1/2}$, yet their product $S = \Theta\, T_{1/2}$ is preserved. This allows the definition of a topological invariant which preserves this S symmetry. In three dimensions the result is a topological state with antiferromagnetic order. Depending on whether the surface breaks the S symmetry or not, metallic surface states may arise within the band gap and a half-integer quantum Hall effect is expected [48]. Moreover, in certain systems, the presence of the topological phase is bound to the antiferromagnetic phase and so vanishes above the Néel temperature. This makes the AFTI particularly interesting, as the topological state appears only after the system undergoes a classical phase transition. Therefore, changing the temperature allows one to turn the topological phase on or off, resulting in a quantum phase transition at T_N.

Mong *et al.* [48] propose two different models. "Model A" is based on the strong topological insulator as introduced in Section 2.6, but with an additional term in the Hamiltonian that breaks TR- and $\mathrm{T}_{1/2}$-symmetry.

In their "model B" they show how spin-orbit interaction may result from the Néel order. The model contains itinerant electrons and fixed spins. When the electrons hop between lattice sites they may do so through intermediate magnetic sites. For certain paths of the conduction electrons the magnetic moments serve to create an Aharonov-Bohm-like flux which in turn acts as intrinsic spin-orbit coupling, responsible for the topological order. One can illustrate the basic concepts in a two-dimensional lattice with four atoms placed in a rhombohedral arrangement as depicted in Figure 3.1 a). The spin-orbit term for a path from the non-magnetic site X to the non-magnetic site Y along the bonds $X \to M$ and $M \to Y$ (where M is a magnetic site), depends on how the spins on the two magnetic sites are oriented [50]. If both spins are aligned in the $+z$ direction, they create a

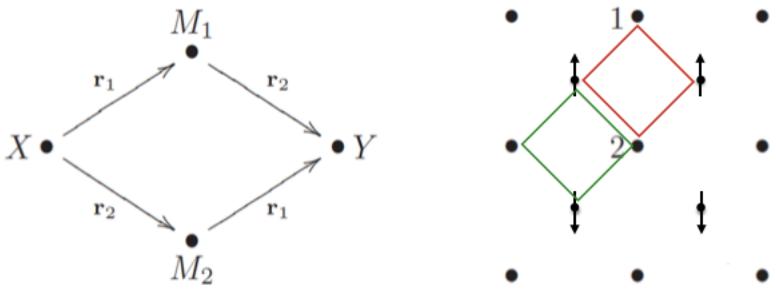

Figure 3.1: Left panel: Shematic of inter-plane hopping. SO coupling between X and Y depends on the orientation of the spins on the two lattice sites M_1 and M_2. Right panel: cross-section of the Mong model B at the (110) plane with the spin direction arbitrarily chosen to lie in the plane. The red and the green path indicate two possible hopping terms with and without additional SO coupling due to the magnetic order [48].

net magnetic field inside the rhombus and therefore the symmetry between the two paths is broken. One can account for the orbital effect of this net magnetic flux by attaching an Aharonov-Bohm phase of $e^{\pm i\phi}$ to each of the two paths. The spin-orbit term of the effective Hamiltonian then takes the form [48].

$$H_{SO} = i\lambda_{SO}[e^{\pm i\phi} r_1 \wedge r_2 + e^{\pm i\phi} r_2 \wedge r_1] \cdot (c_Y^\dagger \sigma c_X) \approx 2\phi\lambda_{SO}|r_2 \wedge r_1| \cdot (c_Y^\dagger \sigma^z c_X). \qquad (3.1)$$

Equation 3.1 shows that the flux ϕ is proportional to the path asymmetry between the two bonds along r_1 and r_2 in the rhombus and therefore to the net magnetization at the magnetic sites M. In other words, the magnitude of the spin-orbit term is proportional to the absolute spin-component in $\pm z$ direction. The theoretical model is inspired by systems like GdBiPt which have been proposed to be topological based on band structure calculations, without the additional spin-orbit coupling from the AFM order [51–54]. In order for the S symmetry to be preserved together with a significant spin-orbit coupling, the model requires a specific magnetic structure. The moments should be aligned ferromagnetically in layers which are stacked antiferromagnetically. For the half-Heusler structure, this spin-orbit term is maximal if the moments are aligned ferromagnetically in the (111) plane and stacked antiferromagnetically along the $[111]$ space diagonal as shown in Figure 4.1 [51].

3.3 Half-Heusler Compounds

The Heusler and the derivative half-Heusler structures favour half-metallic band structures with just one band crossing at the Fermi level, while leaving all the other bands well separated and have been also proposed as candidate materials for *conventional* topological insulators [51, 55]. *RE*BiPt materials, where *RE* is a rare earth, discovered in 1991 [56], are are members of the half-Heusler family of compounds. They display a whole set of emergent behaviours ranging from a massive electron state in YbBiPt [57], to superconductivity without inversion symmetry in LaBiPt [11], LuBiPt, [16], and YbBiPt [13–15], to CeBiPt which shows a magnetic field-induced change of the Fermi surface [12] (see Figures 3.2 & 3.3). Such a field-induced change is absent in the compound LaBiPt whose properties are consistently described by Fermi-liquid theory [58]. CeBiPt on the other hand differs from this model at temperatures below 10 K with a substantial increase in the Shubnikov-de Haas (SdH) frequency by almost a factor of two for certain magnetic field orientations. It is the Ce $4f$ electrons that become decoupled from the delocalized electrons with an increasing magnetic field, that are responsible for these observed band structure modifications.

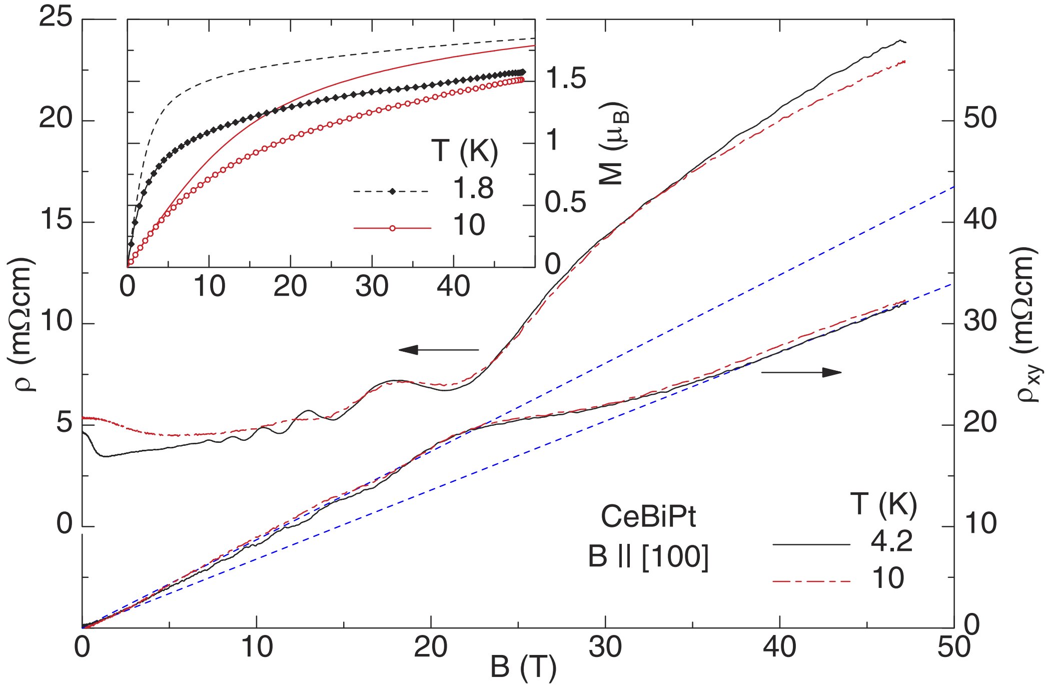

Figure 3.2: Field dependence of the longitudinal and transverse resistivities of CeBiPt for different temperatures. The dashed lines are linear fits to the low- and high-field Hall data with a Hall carrier density of $9.2 \times 10^{-17} cm^{-3}$ in the regime below 25 K and of $7.3 \times 10^{-17} cm^{-3}$ above. The inset shows the measured (symbols) in comparison to the calculated (lines) magnetization [58].

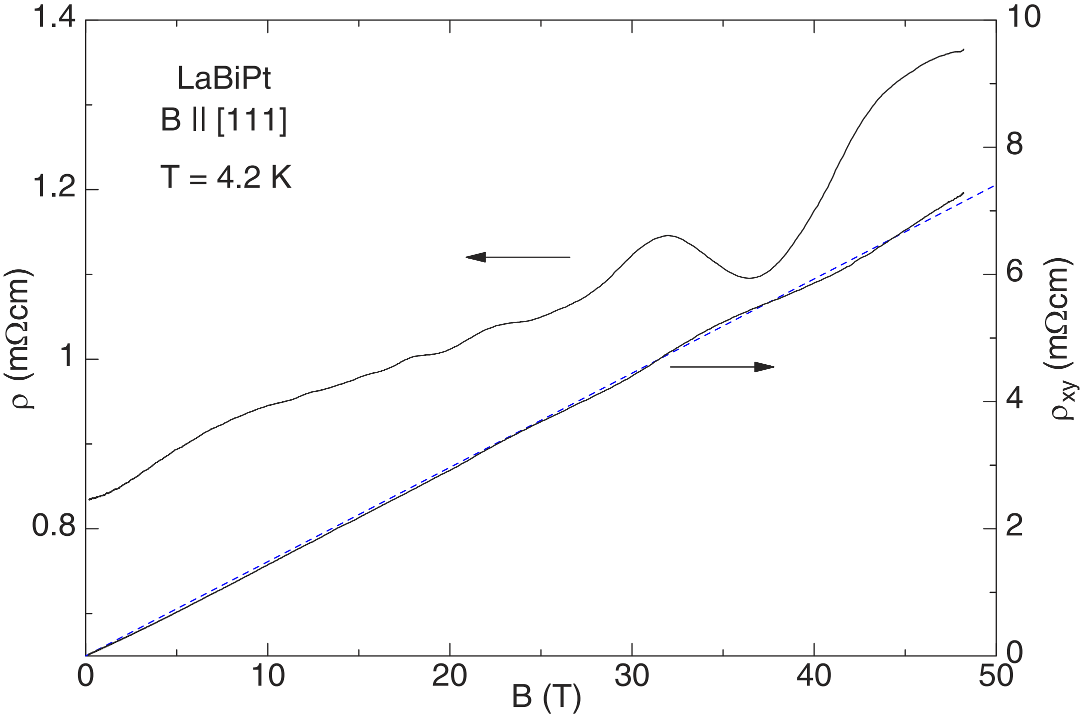

Figure 3.3: Field dependence of the longitudinal and transverse resistivities of LaBiPt. The dashed line is a linear fit to the Hall data resulting in a Hall carrier density of $4.2 \times 10^{-18} cm^{-3}$ [58].

This also led to investigations of the *RE*BiPd [59] versions which resulted in the discovery of superconducting LuBiPd, a compound that shows an anomaly in the electronic specific heat, and weak anti-localisation, which is characteristic for 2D conduction [60].
Angle-resolved photoemission experiments on Lu, Dy, and GdBiPt have shown indications of metallic surface states that differ from the bulk band structure [61]. Liu *et al.* [61] found that within their resolution an even number of bands cross at the chemical potential, making surface states vulnerable to non-magnetic backscattering and these materials should not be qualified as strong topological insulators and can therefore be excluded from "model A" proposed by [48] (see Figure 3.4). Also it has to be mentioned that the half-Heusler structure does not meet the symmetry considerations of "model A" and we therefore focus from here on on "model B".
On this background we have carried out neutron and X-ray diffraction experiments on single crystals and powder samples in order to determine the magnetic structures of GdBiPt and NdBiPt, as their nuclear crystal structure have all the necessary symmetries for being AFTI.

3.4 The $\mathbb{Z}_2$ invariant for the S-symmetry class

In Section 1.4 and 2.7, we have already touched on the classification of electronic states according to topological invariants. The $\mathbb{Z}_2$ classification, defined for time reversal invariant Hamiltonians, is analogous to the Chern number classification of the quantum Hall effect where the magnetic field breaks TR symmetry. For the S-symmetry class that is inherent to the AFTI phase, we can yet find another equivalent $\mathbb{Z}_2$ index, one that is characteristic for an invariant transformation behaviour of the Hamiltonian under the combined S-symmetry.
From the lattice translational vectors a_i, $i = 1,2,3$ we can choose a "stiff" axis along which the translation operator acts – let's say a_3 – so that the translational operator $T_{1/2}$ is given by a translation of $-\frac{1}{2}a_3$. $T_{1/2}^2$ in the antiferromagnetic phase, where the unit cell is

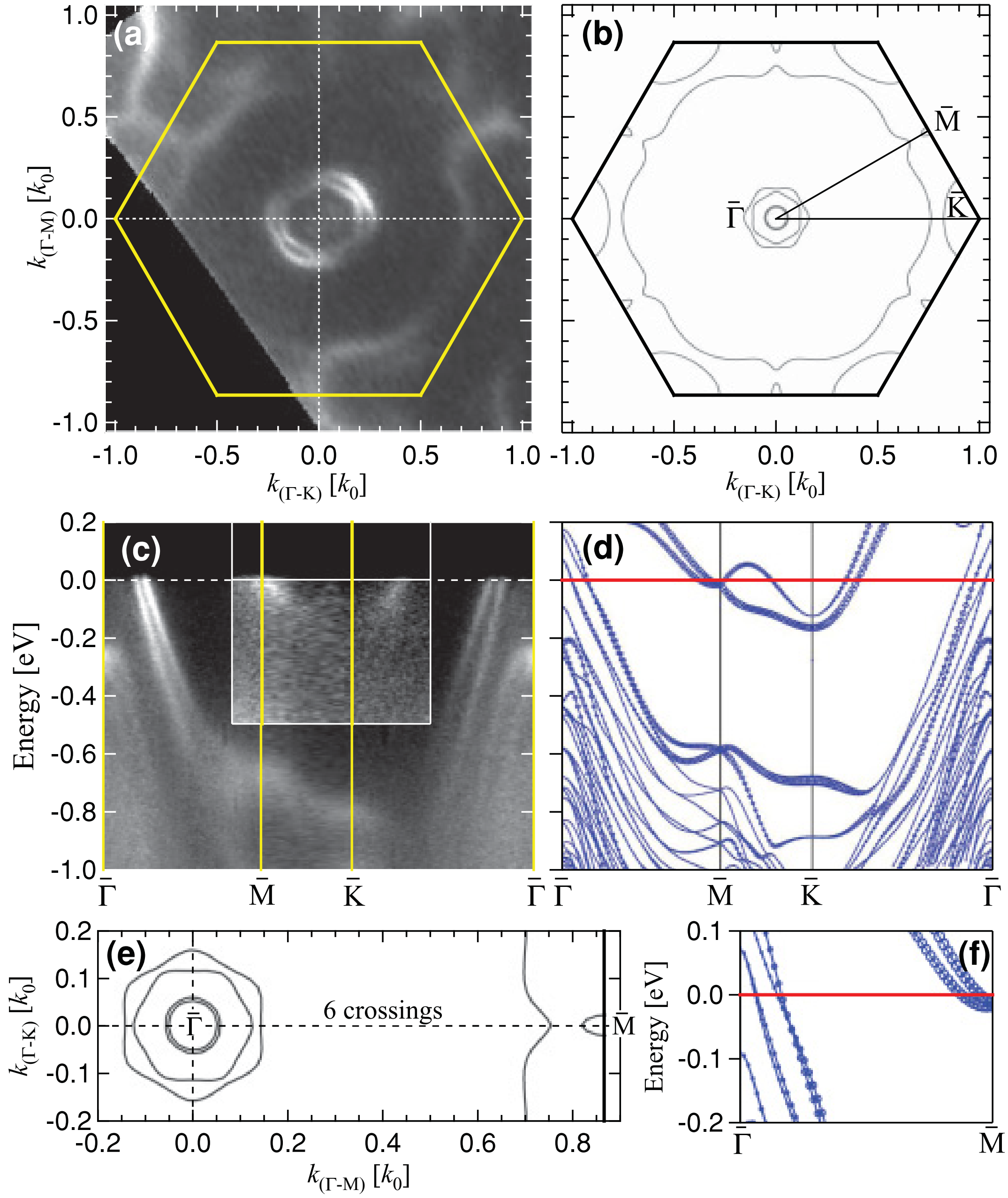

Figure 3.4: Surface electronic structure of GdPtBi: Comparison between ARPES data and calculational result. (a) Fermi map of GdPtBi observed by ARPES, same as in Fig. 1(e). (b) Calculational surface Fermi map of GdPtBi at the Bi(111) cleaving plane. See text for details. (c) ARPES band structure along the contour $\bar{\Gamma}-\bar{M}-\bar{K}-\bar{\Gamma}$. Inset of (c) shows enhanced ARPES intensity near $\bar{M}$ and $\bar{K}$ for better visibility of the bands. (d) Calculational band structure with respect to (c). Sizes of hollow circles represent the contribution of surface Pt atoms. (e),(f) Expanded figures for (b) and (d), respectively, showing six Fermi crossings. Panel (e) is rotated by 30° with respect to (b) [61].

doubled, will be equal to a translation of $-a_3$. In reciprocal space we can therefore write:

$$T_{1/2}(\mathbf{k}) = e^{\frac{i}{2}k_3} \begin{pmatrix} 0 & \mathbb{1} \\ \mathbb{1} & 0 \end{pmatrix}, \tag{3.2}$$

where $\mathbb{1}$ represents the identity on half of the unit cell [48]. Equation 3.2 shows the difference of the new symmetry S from the antiunitary transformation behaviour of Θ, i.e. while $\Theta^2 = -1$ for spin-$1/2$ particles, we find now $S^2 = -e^{ik_3}$. The Hamiltonian stays invariant under S:

$$S_k H(\mathbf{k}) S_k^{-1} = H(-\mathbf{k}). \tag{3.3}$$

At the boundary in k_3-direction of the Brillouin zone, we can write for the Hamiltonian of the so defined plane:

$$SH(k_1, k_2, 0)S^{-1} = H(-k_1, -k_2, 0) \tag{3.4}$$

and $S^2|_{k3=0} = -1$. The $\mathbb{Z}_2$ invariant of this 2D system is equivalent to the ν index we have seen in Section 2.7 and even though this invariant was calculated from a 2D slice of the Brillouin zone for a particular choice of unit cell it characterizes the topology of the 3D band structre [48]. Mong *et al.* show that the S-symmetry results in no such invariants in 1D or 2D and that the 3D invariant is independent of unit-cell choice.

In Chapter 4 & 5 we will see if the concept of the AFTI is applicable to two specific half-Heusler compounds. The Half-Heulser structure has the advantage being built out of three interpenetrating fcc lattices and is symmetric under space inversion. We can therefore as in Sec. 2.7 calculate the $\mathbb{Z}_2$ invariant by looking at the four time-reversal momenta at $k_1, k_2 \in \{0, \pi\}$ [48].

CHAPTER 4

HALF-HEUSLER GDBIPT

4.1 Introduction

In the last chapter we have already pointed out that members of the *RE*BiPt family show many interesting properties such as superconductivity, antiferromagnetic order and super-heavy-fermion behaviour. Band structure calculations and ARPES experiments on Lu, Nd, and GdBiPt [61] indicate the presence of metallic surface states that differ strongly from the band structure in the bulk. However, the authors found that within their resolution an even number of bands cross the Fermi level at the surface. As a result, these states are sensitive to disorder (unlike in strong topological insulators where an odd number of crossings is expected, protecting surface states from being backscattered by a non-magnetic impurity). An inelastic X-ray scattering study on GdBiPt indicated a doubling of the unit cell along its [111] space diagonal, however the authors were unable to establish the exact direction of the magnetic moments [62], information that is essential in determining whether GdBiPt could be an AFTI.

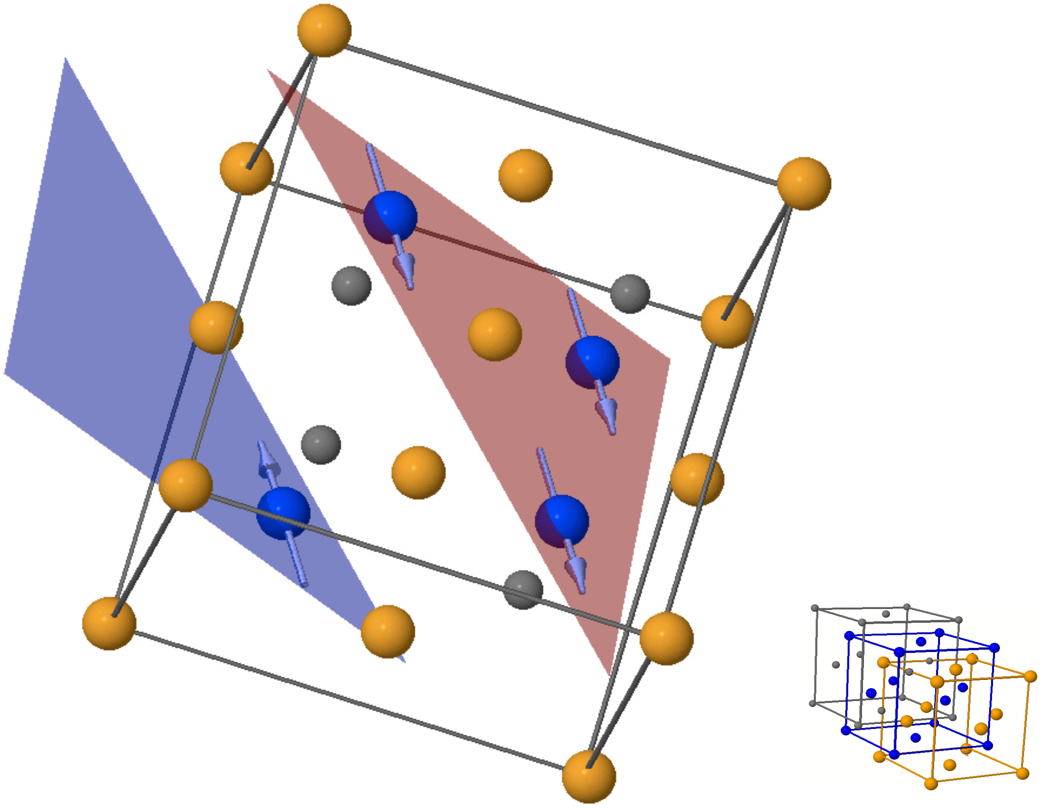

Figure 4.1: The Gd atoms are shown in blue, the Bi in gray, and the Pt in yellow. The spins on the Gd atoms are oriented in ferromagnetic planes which are stacked antiferromagnetically along the magnetic propagation vector $(\frac{1}{2}\frac{1}{2}\frac{1}{2})$. The small image shows the full half-Heusler structure [10].

4.2 Sample growth

Single crystals were grown using Bi flux. Gd, Bi and Pt of high purity were placed in a ceramic crucible in the ratio 1:15:1 which was then sealed in a quartz ampoule under argon atmosphere. The melt was kept at 1200 °C for two days and then cooled down to 550 °C over a one-weak period. After two days the ampoules where then taken out of the furnace and centrifuged to separate the flux from the crystals.

4.3 Crystal structure of GdBiPt

GdBiPt crystallizes in the cubic half-Heusler crystal structure with the space group $F\bar{4}3m$ [56]. The half-Heusler structure consists of four interpenetrating fcc lattices shifted by $[\frac{1}{4},\frac{1}{4},\frac{1}{4}]$, three of them occupied by a different element while the fourth forms an ordered vacancy (see Figure 4.1). We carried out combined refinement of our X-ray and neutron scattering data, which yields the lowest χ^2, if the atoms in GdBiPt take the same positions as reported for YbBiPt [63] and CeBiPt [12] - platinum located on the $[0,0,0]$ site (4*a*), Gd^{3+} on the $[\frac{1}{4},\frac{1}{4},\frac{1}{4}]$ (4*c*), and Bi on the $[\frac{3}{4},\frac{3}{4},\frac{3}{4}]$ position (4*d*) (See Table 4.I). These atomic positions are in agreement with the ones that have been previously reported by Kreyssig *et al.* [62]. In addition, we also carried out a single crystal X-ray diffraction experiment. Due to the non-centrosymmetric nature of the $F\bar{4}3m$ space group, we also tested an inverted structure (racemic twin) with Pt on the 4*a*, Bi on the 4*c* and Gd on the 4*d* site in order to see if such a structure could account for the observed intensities (see Figure 4.8). In a non-centrosymmetric structure, anomalous X-ray scattering leads to different intensities for so-called *Friedel* pairs, such as (hkl) and $(\bar{h}\bar{k}\bar{l})$.The refinement confirmed the original structure, resulting in R1 = 0.0241, where R1 is the difference between the experimental observations and the ideal calculated values, and a Flack parameter, which is the absolute structure factor, of -0.13(2) for the current structure in contrast to R1 = 0.0806 and Flack parameter of 1.2(1) for the inverted structure (please note that a Flack parameter is 0 for the correct structure and 1 for the inverted structure).

Table 4.I: Comparison of the χ^2 obtained from refining the powder data for the three different possible occupation of the crystallographic sites.

site		reported in [62]	Gd on unique site	Bi on unique site
$0,0,0$ $4a$	unique site	Pt	Gd	Bi
$\frac{1}{4},\frac{1}{4},\frac{1}{4}$ $4c$		Gd	Bi	Pt
$\frac{1}{2},\frac{1}{2},\frac{1}{2}$ $4b$	ordered vacancy			
$\frac{3}{4},\frac{3}{4},\frac{3}{4}$ $4d$		Bi	Pt	Gd
χ^2	Neutrons	23.7	86.1	32.6
	X-rays	10.4	26.3	14.9
	Combined	25.1	74.8	34.79

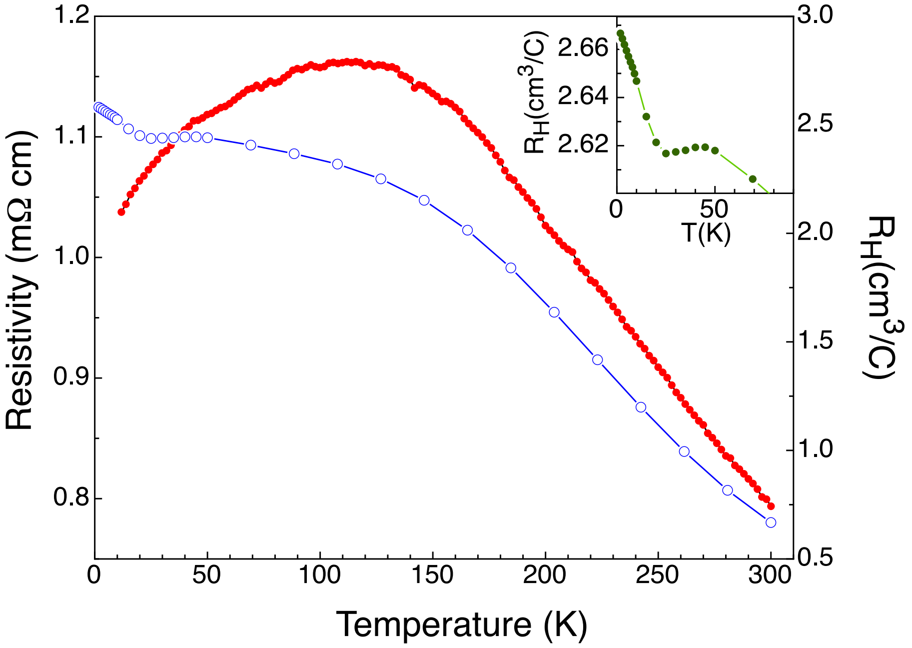

Figure 4.2: The solid points show the resistivity $\rho(T)$ of GdBiPt at zero magnetic field for a temperature range of 10 K to 300 K. The open circles show the temperature evolution of the Hall coefficient from 1.8 K to 300K, revealing a kink well above the 9 K Néel temperature (shown in more detail in the inset).

4.4 Magnetic and Transport Properties

GdBiPt has a low carrier density ($\sim 3 \cdot 10^{18}$ cm^{-3}/C). Figure 4.2 shows that there is a gradual increase in the Hall coefficient as the temperature is reduced, with a clear kink near 25 K. The Hall coefficient was measured using a Quantum Design PPMS, which was also used for the specific heat measurements. CeBiPt also shows such a kink followed by a stronger increase of R_{H}. In CeBiPt this kink appears at the transition temperature T_{N} and was ascribed to the development of a superzone gap in the ordered state and consequently a reduction of the number of charge carriers [64]. In GdBiPt a similar kink seems to be present, however it occurs around 25 K which is above $T_{\mathrm{N}} \sim 9$ K.

For a temperature range of 50 to 300 K, the magnetic susceptibility χ of Gd^{3+} shows a Curie-Weiss behaviour with a Curie-Weiss temperature θ_{W} of $-31.5(3)$ K, and an effective magnetic moment μ_{eff} of $7.97(4)\mu_{\mathrm{B}}$ consistent with the $7.94\mu_{\mathrm{B}}$ expected for Gd^{3+}.

The data were taken in an applied field of 0.05 T using a Quantum Design VSM squid magnetometer. The magnetic entropy S_{mag} shown as the dashed line reaches $0.9R\ln(8)$ at T_{N} indicative of the absence of frustration in contrast to the predictions of [65]. Here S_{mag} was calculated by integrating the magnetic specific heat $C - C_{\mathrm{ph}} - C_{\mathrm{el}}$ after subtracting the phonon C_{ph} and electronic contributions C_{el}, respectively. Figure 4.3 shows that also $\frac{d}{dT}(\chi T)$ exhibits a peak at 8.5 K which confirms the antiferromagnetic ordering with a Néel temperature T_{N} of 8.5 K. In fact, all three measurements: Specific heat $C_p(T)$, electrical resistivity $\frac{d}{dT}\rho(T)$ (not shown), as well as the magnetic susceptibility $\frac{d}{dT}(\chi T)$, show discontinuities at the same critical temperature T_{N}, giving evidence to the high quality of our samples [66, 67].

A Debeye fit of C/T as a function of T^2 for temperatures above 15 K yields a $C_{\mathrm{ph}} = \beta T^3$ with a β of $2.9(2) \times 10^{\text{fl}4}$J /mol K^4. This value of β corresponds to a Debye temperature θ_{D} of 188(5) K. The same fit results in Sommerfeld coefficient γ of only 2 mJ/mol K^2, which is low for a metallic compound containing heavy elements such as Gd and Bi. In contrast, the heavy fermion YbBiPt shows a γ of 8 J/mol K^2, which was assigned to low-lying crystal field levels [63]. Since in GdBiPt the angular momentum L of the $4f^7$ configuration is zero, crystal fields are not expected to play a significant role. Consequently, we should observe the full magnetic moment of the Gd^{3+} ion. This is supported by the 0.9 R ln(8) entropy release observed in the phase transition.

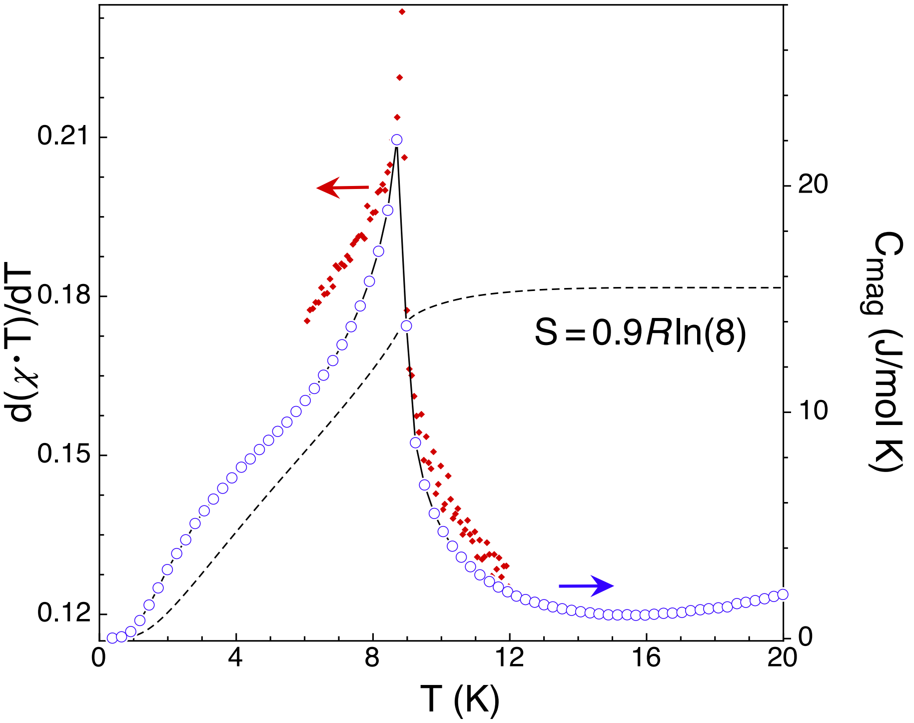

Figure 4.3: The open circles show the magnetic specific heat $C_m = C - C_{\mathrm{ph}} - C_{\mathrm{el}}$, solid diamonds show the temperature derivative of the magnetic susceptibility $\frac{d}{dT}(\chi T)$. The dashed line represents the temperature dependence of the entropy obtained from integrating the magnetic specific heat, showing no sign of frustration.

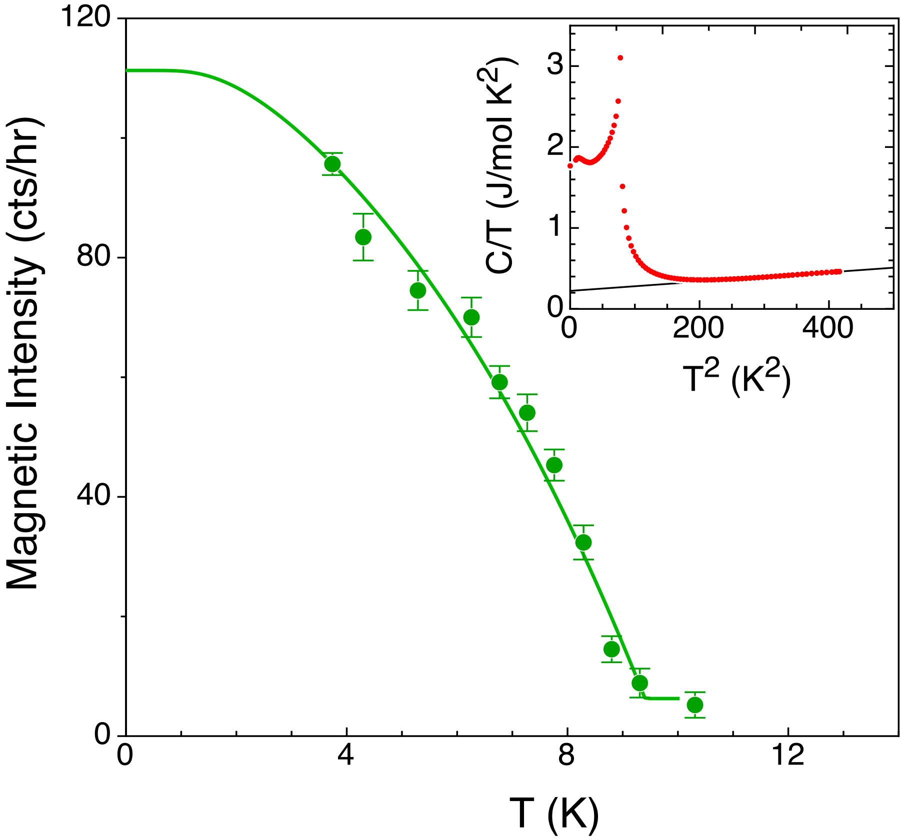

Figure 4.4: Inset: the specific heat is shown as C/T vs. T^2. The solid line is a fit to determine the phonon contribution $C_{\mathrm{ph}} = \beta T^3$ and the electronic specific heat $C_{el} = \gamma T$. Solid green circles show the intensity of the first magnetic peak $(\frac{1}{2}\ \frac{1}{2}\ \frac{1}{2})$ plotted as a function of temperature. The solid line is a fit to the square of the magnetic moment, obtained from numerically solving a Weiss model for a J of $\frac{7}{2}$.

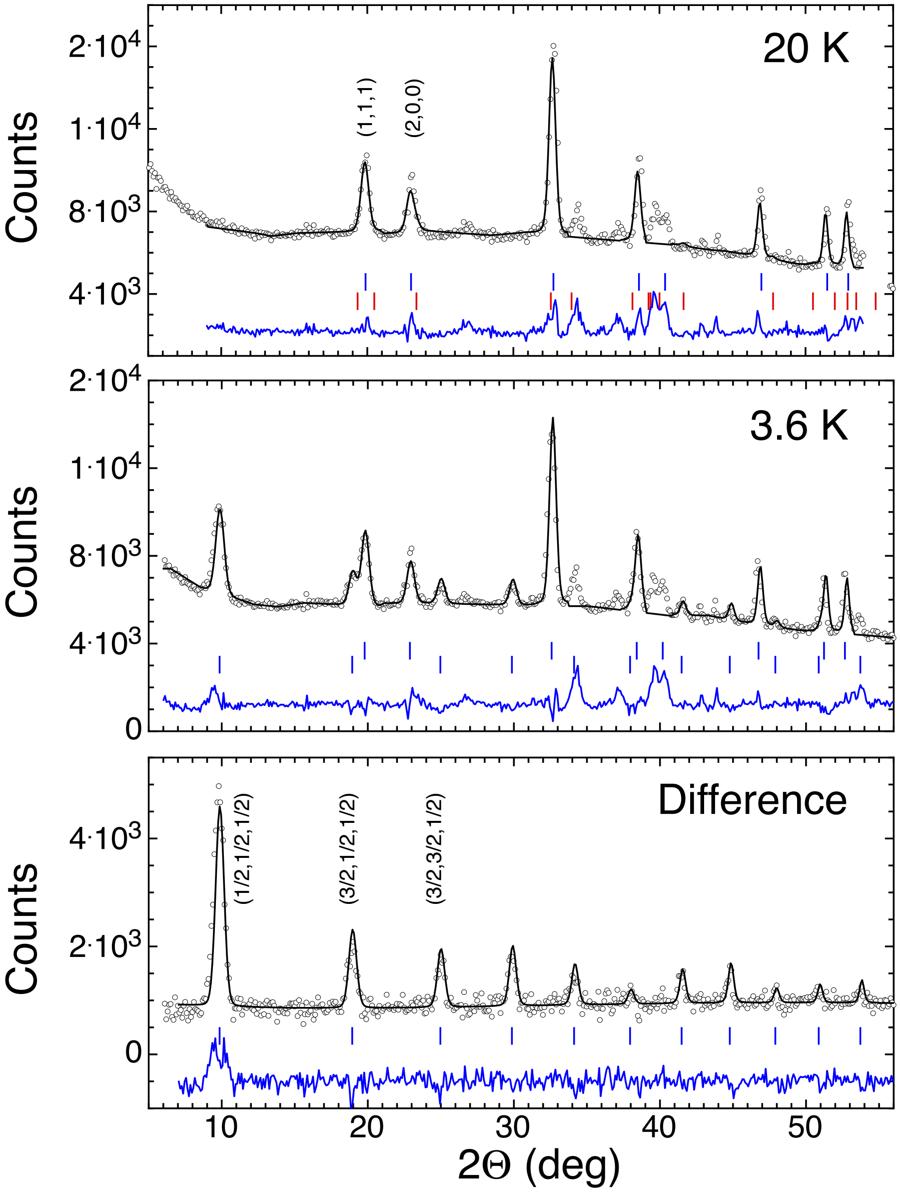

Figure 4.5: Neutron powder diffraction patterns for GdBiPt taken above (20 K, top panel) and below (3.6 K, middle panel) the Néel temperature. The bottom panel emphasises the form of the magnetic scattering by showing the difference between the 20 K and 3.6 K patterns. The solid line through the data is a fit (described in the text) while the solid line below each pattern shows the residuals. In the 20 K pattern (top), the upper set of Bragg markers are for the nuclear contribution from GdBiPt. The second row indicates the position of Bi flux. In the 3.6 K pattern (middle), the first row of Bragg markers is the nuclear contribution, and the bottom row is the magnetic contribution. As the difference pattern (bottom) only has magnetic peaks, the Bragg markers are for the magnetic pattern.

4.5 Neutron Diffraction Results

Neutron diffraction experiments were carried out on the C2 multi-wire powder diffractometer (DUALSPEC) at the NRU reactor of the Canadian Neutron Beam Centre in Chalk River, Ontario (see Figure 5.4). A neutron wavelength λ of 1.3286(1) Å was used as no long-period antiferromagnetic ordering modes were expected.

Our GdBiPt crystals were grown from non-enriched Gd containing the natural abundance of the different Gd-isotopes which lead to an extreme absorption cross section of GdBiPt [68]. To maintain the feasibility of carrying out our neutron diffraction experiment, we used a thinly dispersed sample on a large flat Si sample plate with a very low background [68]. The setup can be seen in Figure 4.7. This geometry reduces the effects of the extreme absorption cross-section of natural gadolinium and permits neutron diffraction on regular samples (no isotopic separation) at thermal wavelengths. To prepare the flat-plate samples for the neutron diffraction measurements, ~ 400 mg (about a $1/e$ absorption thickness) of finely powdered material was spread across a 2.4 cm$\times$8 cm area on a 600 μm thick single-crystal silicon wafer and immobilized using a 1% solution of GE-7031 varnish in toluene/methanol (1:1). A second silicon wafer was used as a cover. The two plates were mounted in an aluminum frame and loaded into a closed-cycle refrigerator with the sample in a partial pressure of helium to ensure thermal uniformity. The plate was oriented with its surface normal to the incident neutron beam to maximize the total flux onto the sample and the measurements were made in transmission mode.

4.5.1 Antiferromagnetic order on a face centred cubic lattice

Figure 4.6 shows the two symmetry points and two possible propagation vectors for simple antiferrromagnetic ordering on a face centred cubic lattice, corresponding to the so-called type-I and type-II antiferromagnetic structure [69, 70]. A simple antiferromagnetic structure is defined by a propagation vector which corresponds to a symmetry point of the Brillouin zone, i.e. $\mathbf{k} = \mathbf{H}/2$ where $\mathbf{H}$ is a reciprocal lattice vector [69]. For the type-III structure we find $\mathbf{k} \neq \mathbf{H}/2 = (1, \frac{1}{2}, 0) = \frac{1}{4}(4,2,0) = \mathbf{H}/4$ which was classified as commensurate structure by Rossat-Mignod [71] rather than an antiferromagnetic structure. Also the type-IV structure, with $\mathbf{k} = (0, -\frac{1}{2}, \frac{1}{2})$ and observed in CrN, should be considered as commensurate. Type-I and type-II magnetic structures are the most commonly found for many rare-earth compounds that crystallize in a NaCl-type structure.

4.5.2 Antiferromagnetic order in GdBiPt

The neutron diffraction pattern in the top panel of Figure 4.5 was taken at 20 K, well above the Néel temperature. It therefore shows only nuclear reflections which can be indexed with the MgAsAg-type fcc structure. On cooling below T_N to 3.6 K the gadolinium moments order and several magnetic reflections appear in the middle panel of Figure 4.5. All of the magnetic peaks can be indexed as $(\frac{2n-1}{2}\,\frac{2n-1}{2}\,\frac{2n-1}{2})$ with n =1, 2, ..., indicating that the magnetic unit cell is doubled along the (1,1,1) direction of the crystallographic unit cell.

Plotting the intensity of the first magnetic peak against temperature (Figure 4.4) and fitting it with a Weiss model for $J = \frac{7}{2}$, reveals a Néel temperature of 9.4(1) K, slightly higher than derived earlier from heat capacity and susceptibility. The $\mathbf{k}$-vector $\mathbf{k}_1 = (\frac{1}{2}, \frac{1}{2}, \frac{1}{2})$ of this type-II antiferromagnetic structure (see Figure 4.6) belongs to a star containing three more elements $\mathbf{k}_2 = (-\frac{1}{2}, \frac{1}{2}, \frac{1}{2})$, $\mathbf{k}_3 = (-\frac{1}{2}, -\frac{1}{2}, \frac{1}{2})$ and $\mathbf{k}_4 = (\frac{1}{2}, -\frac{1}{2}, \frac{1}{2})$,which are equivalent due to the cubic symmetry. We then used the BasIreps program, which is part of the Fullprof Suite [72]) to find the basis functions of the irreducible representations of the $F\bar{4}3m$ space group with $\mathbf{k} = (\frac{1}{2}, \frac{1}{2}, \frac{1}{2})$. This symmetry allows two sets of basis functions whose real and imaginary components are listed in Tab. 4.II.

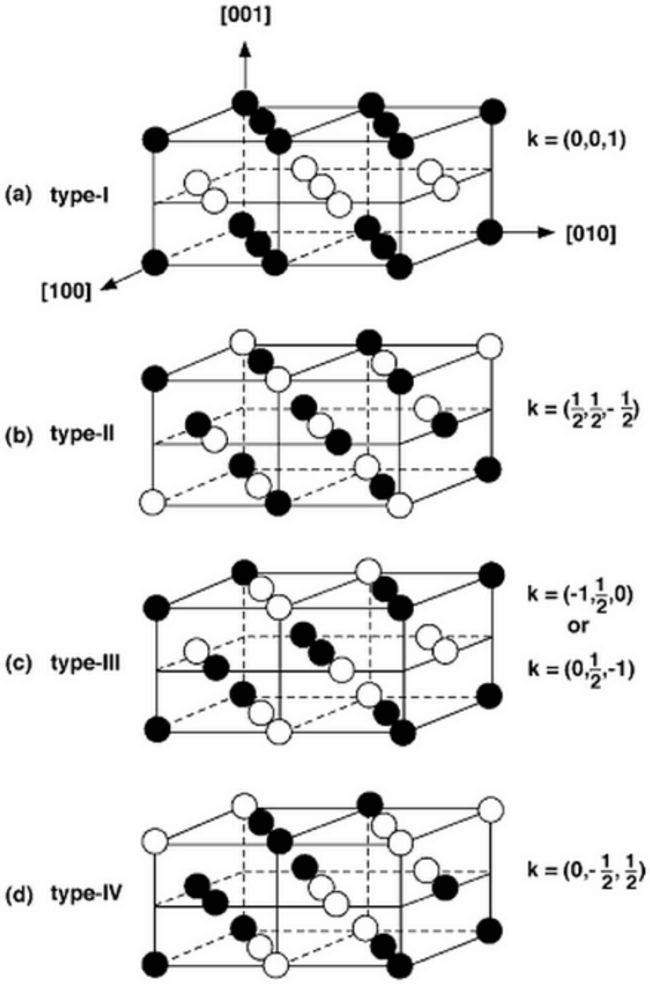

Figure 4.6: Possible antiferromagnetic spin arrangements on a fcc-lattice. Black and white spheres represent spin up and down with respect to any given direction. Also indicated are the propagation vectors [69].

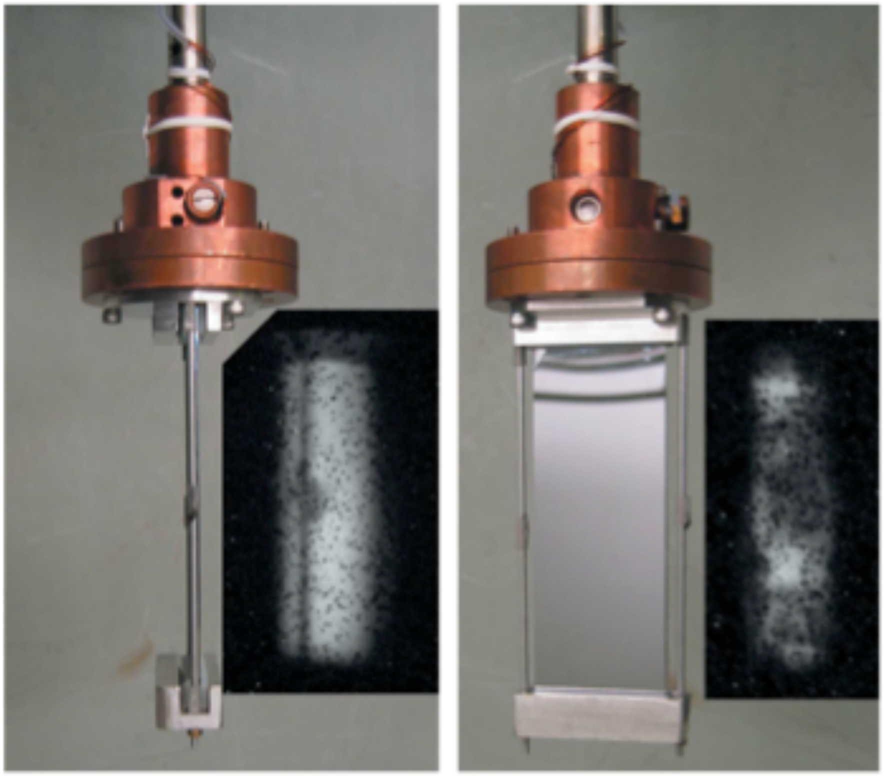

Figure 4.7: Sample holder and corresponding neutron camera images of the silicon plates ($30 \times 90 \times 0.7$mm) each sandwiching 20μm thick $Gd_3Ag_4Sn_4$ powder bound by GE-7031 varnish.[68]

Table 4.II: Real (BASR) and imaginary (BASI) components of the basis vectors for the two permitted commensurable magnetic structures obtained from BasIreps for the space group $F\bar{4}3m$, an ordering wave vector $\mathbf{k}$ of $[\frac{1}{2},\frac{1}{2},\frac{1}{2}]$, and Gd^{3+} sitting on the $4c$ crystallographic site.

	Set 1	Set 2	
BASR	(1 1 1)	(1 -0.5 -0.5)	(-0.5 1 -0.5)
BASI	(0 0 0)	(0 -0.866 0.866)	(-0.866 0 0.866)

For the basis functions given in Tab. 4.II the magnetic moment is given by:

$$\mathbf{S} = C \cdot [\mathbf{BasR} + i\,\mathbf{BasI}] \tag{4.1}$$

The two basis functions of set 2 represents the two racemic structures possible (see Figure 4.8). Due to the fact that we used powder these are indistinguishable in the refinement and we are left with a single parameter C as refinable quantity. The first set of basis functions places the gadolinium moments along the body diagonal of the cubic structure. However the $(\frac{1}{2}\,\frac{1}{2}\,\frac{1}{2})$ peak is forbidden for this set since three of the four equivalent $(\frac{1}{2}\,\frac{1}{2}\,\frac{1}{2})$ peaks are systematically absent due to the translational symmetry of the space group (face centered), and the fourth is absent due to the magnetic polarization factor for neutron scattering. However, it is clear from the difference pattern in figure 4.5 that this is the strongest of the observed magnetic peaks. This allows us to rule out the first set of basis functions. A refinement of the second set of basis functions contains two equivalent basis vectors, of which the first was chosen for the refinement. The 3.6 K pattern returns a Gd magnetic moment of $6.6(7)\mu_\mathrm{B}$ which corresponds to a moment of $7.6(5)\mu_\mathrm{B}$ at 0 K, which is comparable to value of $7.55\mu_\mathrm{B}$ reported for single crystal Gd [73]. The difference pattern in Figure 4.5 was also refined and gave the same $6.7(6)\mu_\mathrm{B}$ for the Gd moment at 3.6 K.

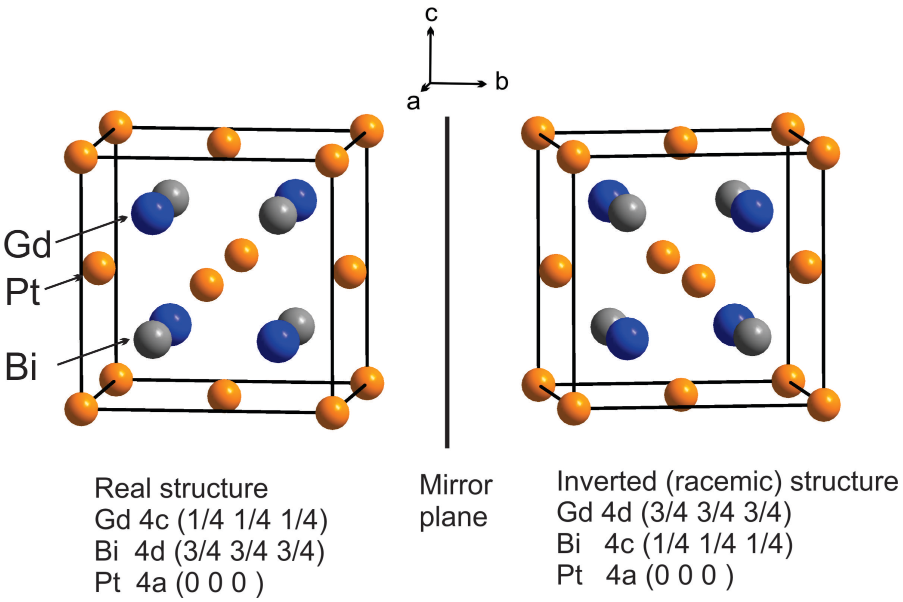

Figure 4.8: View of the two possible atom arrangements in a racemic structure which can be transformed into each other through inversion symmetry. The Pt atoms are shown in orange, the Bi in grey, and the Gd in blue [10].

Previous resonant magnetic X-ray scattering experiments [62], were unable to determine the direction of the magnetic moment of GdBiPt. Their attempts to refine the actual moment direction were inconclusive as they had several sizeable magnetic domains within the $\sim 0.5 \times 0.5$ mm^2 beam footprint that led to incomplete averaging over directions. By working with a powder and a much larger ($\sim 2.5 \times 8$ cm^2) beam footprint, domain averaging is complete in our data permitting a full analysis of the peak intenisties and allowing us to determine the magnetic structure. Complex (e.g. cycloidal) ordering was deemed to be incompatible with the XRMS data [62], and since we detected no other magnetic scattering down to $2\theta = 4°$, ($q \sim 0.33$Å^{-1}), we can directly rule out long-period modulations of the magnetic structure with periods less than about 19 Å (about three lattice spacings). Longer-period modulations would yield satellites around the magnetic peaks which are also absent. We conclude that GdBiPt adopts a simple collinear type-II antiferromagnetic structure.

The magnetic unit cell is eight times larger than the crystallographic unit cell, as the

k=($\frac{1}{2}$, $\frac{1}{2}$, $\frac{1}{2}$) propagation vector doubles all three crystallographic axes. The magnetic moments form ferromagnetic sheets which are stacked antiferromagnetically along the [111] body diagonal (Figure 4.1). The same propagation vector is found for the vanadium doped half-Heusler compound CuMnSb [74], but not for CeBiPt which orders as a type I AFM with a propagation vector of [100] [12]. The evaluation of the magnetic moment direction with the program BasIreps suggests a common, single **k**-vector structure with the moments perpendicular to the space-diagonal.

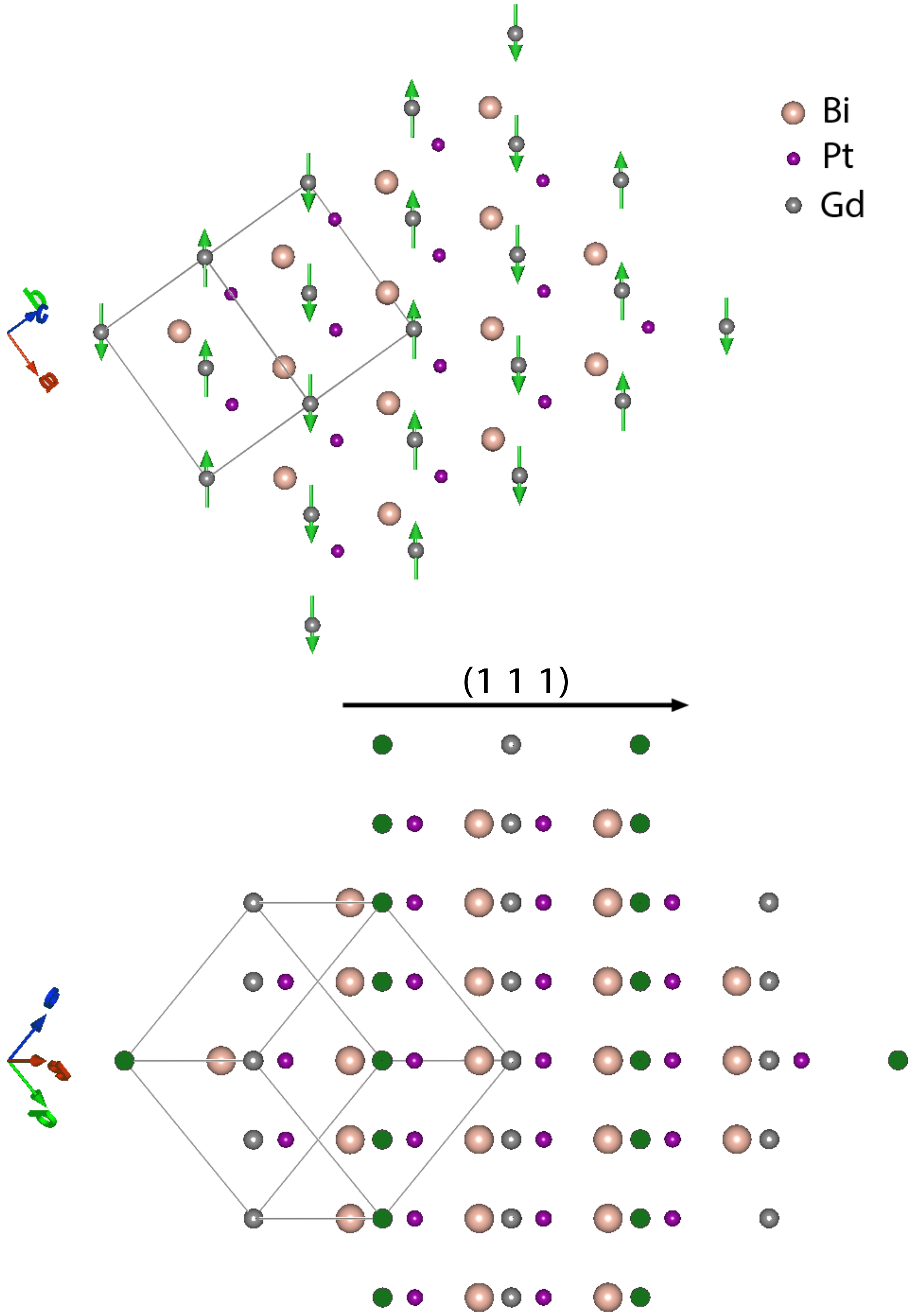

Figure 4.9: View of the magnetic structure of GdBiPt with the [111] body diagonal pointing to the right. The moments are perpendicular to the body diagonal, and form alternating ferromagnetic sheets. The Gd atoms and moments are shown in blue, Bi atoms are grey, and Pt atoms are yellow.

4.6 Conclusion

The results presented here suggest a similar structure to that proposed by Mong *et al.*[48], with an observed spin arrangement that results in strong spin-orbit interaction along the space diagonal. This leads to a path asymmetry for inter-ferromagnetic plane hopping between non-magnetic sites. In conclusion, given its spin-structure, GdBiPt is therefore a promising candidate for an antiferromagnetic topological insulator.

4.7 Additional tables of the neutron and X-ray scattering analysis

We carried out full-pattern magnetic and structural refinements using the FullProf/WinPlotr suite [72, 75] with neutron scattering length coefficients for natural Gd tabulated by Lynn and Seeger [76] As all of the major magnetic reflections occurred below 35°, no absorption correction was applied, however the data were truncated at $2\theta = 54^\circ$ to minimise any possible impact of angle-dependent absorption effects. The room-temperature powder X-ray diffraction data used in the powder refinement was collected on a PANalytical X'Pert Pro diffractometer with a linear X'Celerator detector and Cu K_{α_1} radiation in the 2Θ range from 20° to 120°. The step size was 0.0084° and the total collection time was 12 hours and 54 minutes. For this experiment, a few GdPtBi single crystals were finely ground and deposited on the Si single crystal zero-background sample holder.
Room-temperature single crystal X-ray diffraction data were collected on a STOE IPDSII diffractometer with the MoK_α radiation in the whole reciprocal sphere. A numerical absorption correction was based on the crystal shape that was originally derived from the optical face indexing but later optimized against equivalent reflections using the STOE X-Shape software [77]. Structural refinement was performed using the SHELXL program [78] (Tables 4.III-4.V).

Table 4.III: Anisotropic displacement parameters in units of [Å$^2 \cdot$ 10^3] obtained by refining the single crystal X-ray data. The anisotropic displacement factor exponent takes the form: $-2p^2[h^2 a \cdot 2U^{11} + ... + 2hk\ a \cdot b \cdot U^{12}]$

	U^{11}	U^{22}	U^{33}	U^{23}	U^{13}	U^{12}
Gd	0.0102(7)	0.0102(7)	0.0102(7)	0	0	0
Bi	0.0035(4)	0.0035(4)	0.0035(4)	0	0	0
Pt	0.0091(4)	0.0091(4)	0.0091(4)	0	0	0

Table 4.IV: Summary of the parameters which were obtained from refining the powder diffraction spectra collected at 20, 3.6 K, and the difference pattern.

	20 K	3.6 K	diff
a (Å)	6.681(4)	6.67(9)	6.68(8)
μ_{Gd} (μ_{B})	0	6.6(7)	6.7(6)
Rp	2.20	2.39	9.77
Rwp	2.92	3.23	12.7
Rexp	1.31	1.3	3.08
χ^2	4.99	6.16	17

4.8 Contributions

All samples for this experiment I grew together with Luc Lapointe. He also helped with the characterization of our crystals using different transport measurement techniques. The X-ray study was performed by Yurij Mozhavrivskj at McMaster university in Ontario. All neutron scattering experiments performed at the Canadian Neutron Beam Centre, Chalk River, Ontario where conducted with Prof. Dominic Ryan from McGill university and Roxana Flacau which acted as our local contact. Prof. Ryan also developed the low-absorption sample holder which enabled us to work with Gadolinium. For the structural refinement using the FulProf software I could always count on the help of Nicolas Lee-Hone and Oksana Zaharko from PSI in Switzerland. Prof. Tami Pereg-Barnea from McGill university helped me with many questions in regard of the theoretical model describing the ATFI.

Table 4.V: Refinement of the GdBiPt single crystal X-ray data.

Empirical formula	GdPtBi
Formula weight	561.32
Temperature	293(2) K
Wavelength	0.71073 Å
Space group	$F\bar{4}3m$
Unit cell dimensions	$a = 6.6772(8)$ Å $\alpha = 90^\circ$
	$b = 6.6772(8)$ Å $\beta = 90^\circ$
	$c = 6.6772(8)$ Å $\gamma = 90^\circ$
Volume	297.70(6) ^{3}
Z	4
Density (calculated)	12.524 Mg/m^3
Absorption coefficient	127.510 mm^{-1}
F(000)	900
Theta range for data collection	5.29° to 34.80°
Index ranges	$-10 \leq h \leq 10$, $-10 \leq k \leq 10$, $-8 \leq l \leq 10$
Reflections collected	1285
Independent reflections	90 [R(int) = 0.0856]
Completeness to theta = 34.80○	100.0 %
Refinement method	Full-matrix least-squares on F^2
Data / restraints / parameters	90 / 0 / 5
Goodness-of-fit on F^2	1.132
Final R indices [I $> 2\sigma(I)$]	R1 = 0.0241, wR2 = 0.0511
R indices (all data)	R1 = 0.0241, wR2 = 0.0511
Absolute structure parameter	-0.13(2)
Extinction coefficient	0.0152(12)
Largest diff. peak and hole	3.058 and -1.094 e.Å^3

Table 4.VI: Bond lengths in units of [Å] obtained from refining the single crystal X-ray data.

Gd-Pt	2.8913(3)
Gd-Pt#1	2.8913(4)
Gd-Pt#2	2.8913(4)
Gd-Pt#3	2.8913(4)
Gd-Bi#3	3.3386(4)
Gd-Bi#4	3.3386(4)
Gd-Bi#1	3.3386(4)
Gd-Bi#5	3.3386(4)
Gd-Bi#2	3.3386(4)
Gd-Bi#6	3.3386(4)
Bi-Pt	2.8913(3)
Bi-Pt#7	2.8913(3)
Bi-Pt#8	2.8913(3)
Bi-Pt#9	2.8913(3)
Bi-Gd#10	3.3386(4)
Bi-Gd#8	3.3386(4)
Bi-Gd#11	3.3386(4)
Bi-Gd#7	3.3386(4)
Bi-Gd#12	3.3386(4)
Bi-Gd#9	3.3386(4)
Pt-Bi#1	2.8913(3)
Pt-Gd#9	2.8913(3)
Pt-Gd#8	2.8913(3)
Pt-Gd#7	2.8913(3)
Pt-Bi#3	2.8913(3)
Pt-Bi#2	2.8913(3)

CHAPTER 5

HALF-HEUSLER NDBIPT

5.1 introduction

In the last chapter we have seen that in its antiferromagnetic phase GdBiPt indicates a doubling of the unit cell along its space diagonal with the moments arranged in ferromagnetic sheets, normal to the [111] direction [10, 79], leading to a path asymmetry for inter-plane hopping of electrons between non-magnetic sites, as proposed by Mong *et al.*, and therefore making this material a strong candidate for the AFTI phase. This has prompted us to carry out single-crystal neutron and X-ray diffraction experiments, to determine the magnetic structure of NdBiPt, another prominent represent of the *RE*BiPt half-Heusler family.

5.2 Sample growth

Our NdBiPt crystals were grown using Bi flux. Nd, Bi and Pt of high purity were placed in a ceramic crucible in the ratio 1:15:1 which was then sealed in a quartz ampoule under argon atmosphere. The melt was kept at $1200\,^{\circ}$C for two days and then cooled down to $550\,^{\circ}$C over a week. After two days the ampoules were taken out of the furnace and centrifuged to separate the flux from the crystals.

5.3 Crystal structure and single crystal X-ray diffraction results

Single crystal X-ray diffraction data were collected at 150 K on a Bruker D8 VENTURE diffractometer with a CMOS PHOTON 100 detector and a liquid metal jet X-ray source using Ga radiation ($\lambda = 1.3414$ Å). The data set was collected using a combination of ω and ϕ scans with a step size of 1°, and 1 s exposure per frame. Data collection and unit-cell lattice parameter determination were performed with the *APEX2* suite [80]. Final lattice parameter values and integrated intensities were obtained using *SAINT* software, and a multi-scan absorption correction was applied with *SADABS* [81]. The structure was refined with *SHELXL* version 2014/3 [78]. NdBiPt crystallizes in the cubic Half-Heusler crystal structure with the space group $F\bar{4}3m$ [56]. This structure consists of four interpenetrating *fcc* lattices shifted by $[\frac{1}{4},\frac{1}{4},\frac{1}{4}]$, where the $[\frac{1}{2},\frac{1}{2},\frac{1}{2}]$ position is an ordered vacancy. The refinement of our single crystal X-ray patterns confirmed this structure (for details see Tabs. 5.I and 5.II). The compound has a lattice constant of $6.7613(2)$ Åwith the Nd^{3+} ion located on the $[\frac{1}{4},\frac{1}{4},\frac{1}{4}]$ (4c), Bi on the $[\frac{3}{4},\frac{3}{4},\frac{3}{4}]$ (4d), and Pt on the $[0,0,0]$ (4a) position, and permutations of $[0,\frac{1}{2},\frac{1}{2}]$ (corresponding to the column D of Tab. 5.I).

In a non-centrosymmetric structure, anomalous X-ray scattering leads to different intensities for so-called *Friedel* pairs, such as (hkl) and $(\bar{h}\bar{k}\bar{l})$. The refinement confirmed the original structure (see Fig. 4.8), resulting in R1 =0.0582, where R1 is the difference between the experimental observations and the ideal calculated values, and a Flack parameter, which is the absolute structure factor, of 0.28(3) for the current structure in contrast to R1 = 0.0800 and Flack parameter of 0.72(4) for the inverted structure, as listed in Tab. 5.I (please note that a Flack parameter is 0 for the correct structure and 1 for the inverted structure).

Table 5.I: Possible arrangements of the Nd, Bi and Pt atoms on the lattice and their single crystal X-ray refinement parameters.

Model	A	B (inv A)	C	D (inv C)	E	F (inv. E)
Nd	$(0,0,0)$	$(0,0,0)$	$(\frac{1}{4},\frac{1}{4},\frac{1}{4})$	$(-\frac{1}{4},-\frac{1}{4},-\frac{1}{4})$	$(\frac{1}{4},\frac{1}{4},\frac{1}{4})$	$(-\frac{1}{4},-\frac{1}{4},-\frac{1}{4})$
Bi	$(\frac{1}{4},\frac{1}{4},\frac{1}{4})$	$(-\frac{1}{4},-\frac{1}{4},-\frac{1}{4})$	$(0,0,0)$	$(0,0,0)$	$(-\frac{1}{4},-\frac{1}{4},-\frac{1}{4})$	$(\frac{1}{4},\frac{1}{4},\frac{1}{4})$
Pt	$(-\frac{1}{4},-\frac{1}{4},-\frac{1}{4})$	$(\frac{1}{4},\frac{1}{4},\frac{1}{4})$	$(-\frac{1}{4},-\frac{1}{4},-\frac{1}{4})$	$(\frac{1}{4},\frac{1}{4},\frac{1}{4})$	$(0,0,0)$	$(0,0,0)$
R1	0.0945	0.0915	0.0800	0.0582	0.0607	0.0389
wR2	0.2518	0.256	0.2188	0.1600	0.1627	0.1003
GoF	1.029	1.046	1.038	1.068	1.050	1.040
Flack	0.81(8)	0.12(4)	0.72(4)	0.28(3)	0.84(6)	0.21(4)
Pos. Res	20.2	21.0	7.9	5.6	3.1	2.7
Neg. Res	-7.9	-6.4	-7.2	-5.9	-4.1	-2.8

5.4 Magnetic and transport properties

All magnetic measurements were taken between 1.8 and 300 K in an applied field of 0.1 T using a Quantum Design VSM SQUID magnetometer. Resistivity was measured in the same temperature range with a Quantum Design PPMS. The specific heat C_p was measured in a ^{3}He insert PPMS using a standard puck but purpose-built electronics.

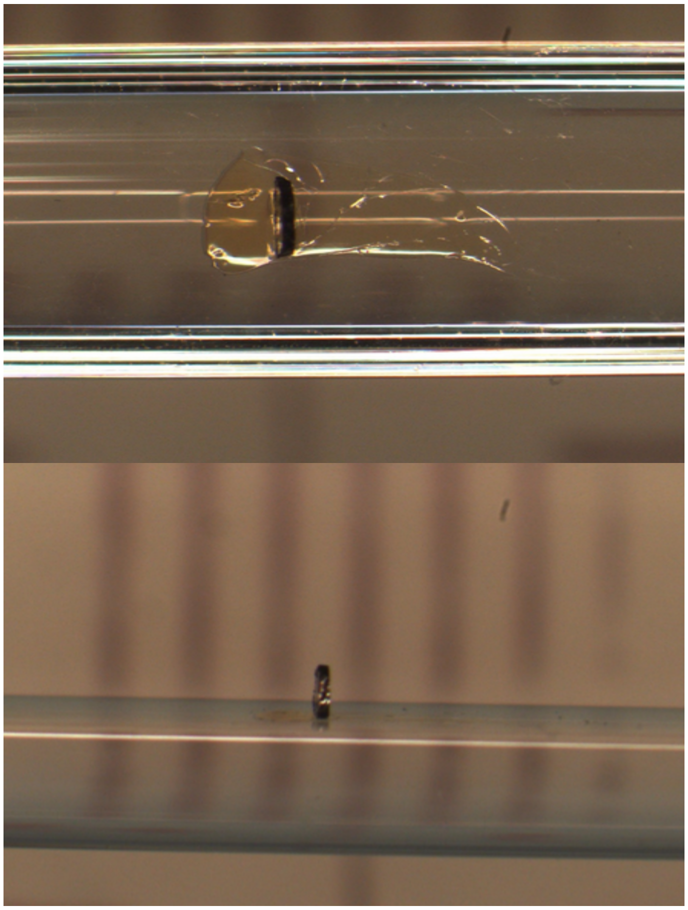

Figure 5.1: Top and side view of a 0.95mg NdBiPt sample that was cut and polished, then mounted on a quartz rod for magnetic susceptibility measurements in a Quantum design SQUID. Dimensions: $0.2mm \times 0.8mm^2$. A magnetic field of a 100Oe was applied parallel to one of the cubic axes.

NdBiPt is a semi-metal with a very low carrier density, and a high carrier mobility [82]. For the temperature range 50 to 300 K, the magnetic susceptibility $\chi = \frac{M}{H}$ measured in an applied field of 0.1 T shows a Curie-Weiss behaviour with a Curie-Weiss temperature

Table 5.II: Refinement of the NdBiPt single crystal X-ray data.

Formula	NdBiPt
Space Group	$F\bar{4}3m$
a (Å)	6.7613(2)
V (Å^3)	309.09(3)
Z	4
Radiation	GaKα
λ (Å)	1.34139
Temperature (K)	150
Density (g/cm^3)	11.783
$\mu(mm^{-1})$	219.35
F(000)	884
T_{min}/T_{max}	0.0062/0.0988
H limits	-8 8
K limits	-8 8
L limits	-8 7
Θ_{max}	1070
Measured	57
Unique	57
Observed R_{int} / R_{σ}	0.1064 / 0.0348

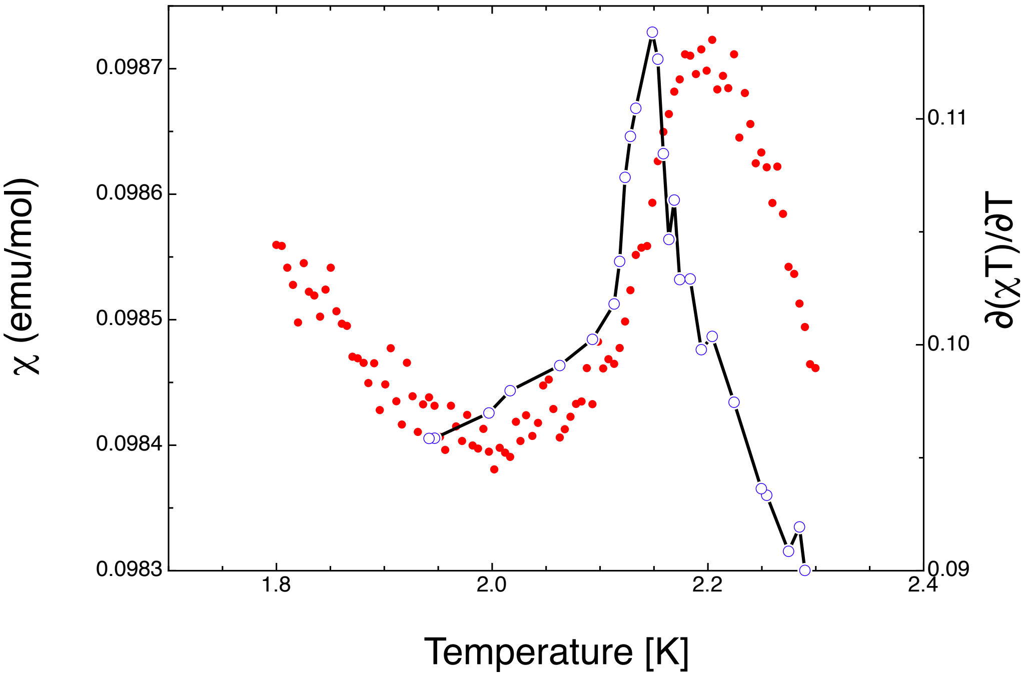

Figure 5.2: Magnetic susceptibility (red dots) and Temperature derivative $\partial(T \cdot \chi)/\partial T$ of magnetic susceptibility (white circles) showing a sharp peak at the critical temperature [9].

Θ_W of -23 K (see Fig.5.3), and an effective magnetic moment μ_{eff} of 3.8 μ_B consistent with the theoretical value of 3.62 μ_B for a free Nd^{3+} ion. Figure 5.2 shows $\chi(T)$ in the temperature range between 1.8 and 2.4 K, where the main features are a maximum at 2.2 K and a subsequent point of inflection at 2.18 K, confirming antiferromagnetic order with a Néel temperature T_N of 2.18 K [83]. Both measurements: Specific heat C_p (see Fig. 5.11), as well as the magnetic susceptibility $\partial(T \cdot \chi)/\partial T$ (Fig.5.2) show a discontinuity at the same critical temperature T_N, giving evidence for the high quality of our samples.

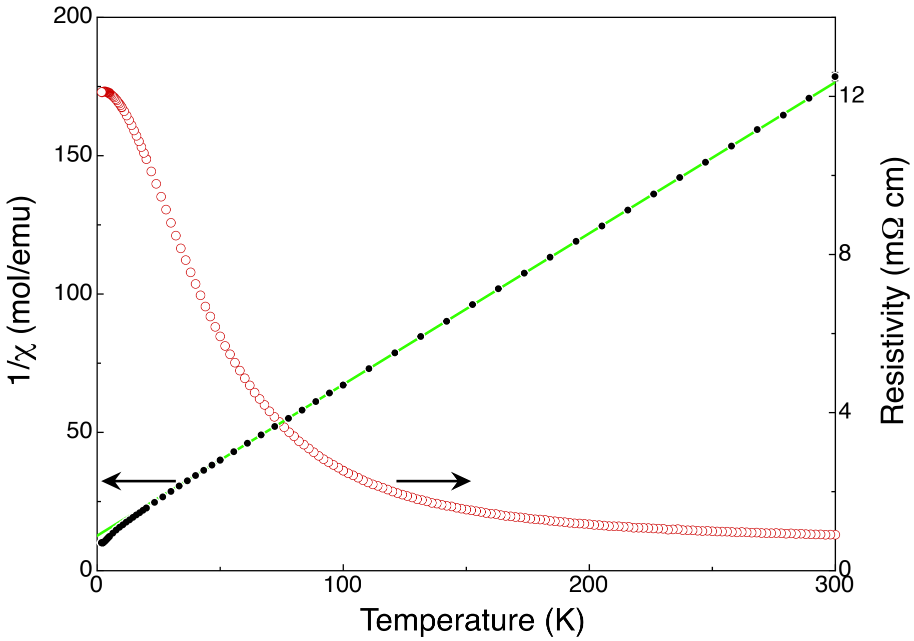

Figure 5.3: Inverse magnetic susceptibility measurement taken at 0.1 T and resistivity (at 0 T) as a function of temperature (black full circles). The inverse susceptibility has been fitted with a Curie-Weiss law in the high temperature regime yielding $\Theta_W = -23$ K with an effective moment of $\mu_{\text{eff}} = 3.8\mu_B$. The red open circles show the resistivity for a temperature range between 1.8 K and 300 K. [9].

5.5 Neutron diffraction

For the single-crystal neutron diffraction experiment we co-aligned three crystals of the size of the order $2 \times 1 \times 1$ mm^3 on an aluminum plate. We oriented our crystals in order to scan the (hhl) scattering plane given the extinction rules of the NdBiPt crystalline structure. Also, this scattering geometry allows us to distinguish between the *type-I* AFM order, seen in the isostructural CeBiPt [12] and *type-II* AFM order, as proposed by Mong *et al.*, in Ref. [48] and observed in GdBiPt [10]. The experiment was carried out on the C5 triple axis spectrometer at the Canadian Neutron Beam Centre in Chalk River. A vertically focusing pyrolytic graphite (PG) (002) monochromator and a flat PG(002) analyzer crystal were used with a fixed final neutron energy of $E_f = 14.56$ meV, with no collimation and with collimations of 0.8°, 0.85°, 2.4°. Two PG filters were placed in the diffracted beam after the sample to eliminate higher order wavelength contamination of the beam (see Figure 5.4). The sample was sealed under helium gas in an aluminium can and mounted in a close-cycle ^{3}He heliox displex cryostat that allowed cooling the sample down to 0.3 K. Neutron diffraction data was collected between 0.3 and 5 K. We used a

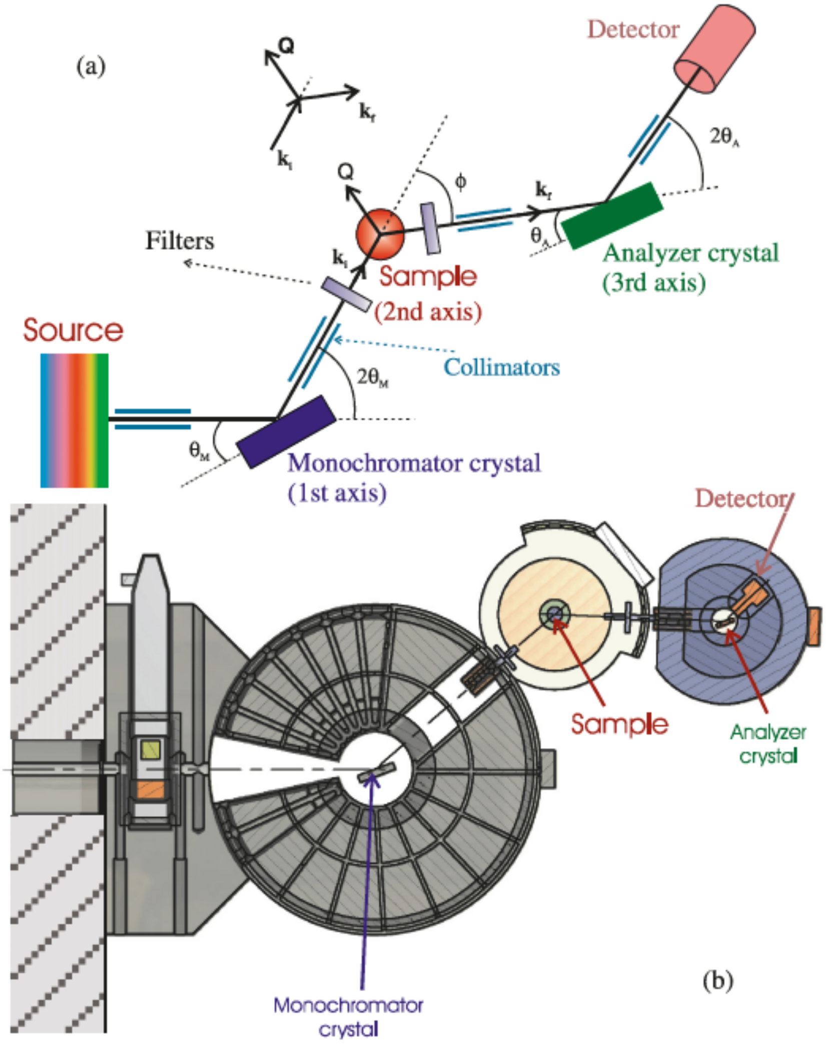

Figure 5.4: Schematic layout of a triple axis spectrometer at the Canadian Neutron Beam Centre. On the first axis a single crystal monochromator selects a specific wavelength from a white neutron beam. The interaction, magnetic and nuclear, with the sample happens on the second axis. The scattered neutrons are then Bragg reflected from the analyzing single crystal according to their energy (3^{rd} axis) and sent into the detector. Collimators placed before and after the sample control angular dispersion of the neutrons. Pg filters are used to cut signal from higher harmonics [84].

linear fit for the the background. Our measurements show slight twinning due to a mis-

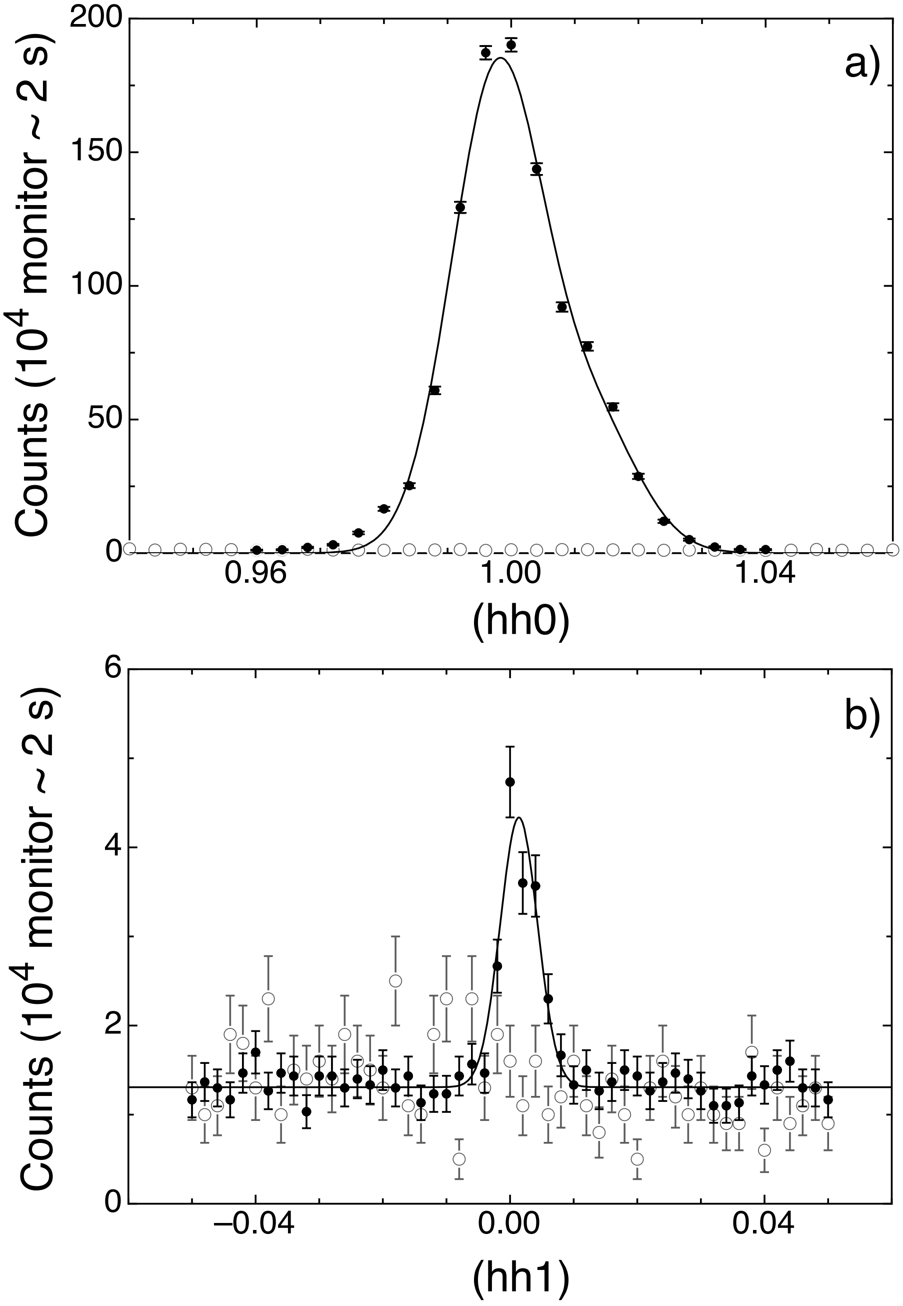

Figure 5.5: (a) (110) magnetic peak above (open circles) and below (black circles) the transition temperature. (b) Signal below $T_\mathbf{N}$ from the magnetic (001) peak which is due to secondary scattering of neutrons which were first diffracted by the (111) nuclear peak [9].

alignment of the mosaic of about one degree. To correct for the twinning the peaks were fitted with a double Gaussian:

$$
\begin{aligned}
G(x) &= B + A \cdot e^{\frac{-4 \cdot \ln 2 \cdot |x - x_0|^2}{s^2}} \\
&\quad \times \left\{ 1 + \frac{1}{R} e^{\frac{4 \cdot \ln 2 \cdot (\Delta^2 + 2|x - x_0| \cdot \Delta)}{s^2}} \right\},
\end{aligned}
\tag{5.1}
$$

where B corrects for an imperfect background subtraction. A is the amplitude and x_0 denotes the centre position of the dominant peak. The parameter s represents the full with at half maximum (FWHM), R is the ratio in intensity of the two peaks and Δ represents the distance between the two peak centres along x.

All the observed magnetic peaks could be indexed as integer fractions of the nuclear peaks indicating a commensurate magnetic structure (see Fig. 5.7a)). As we have seen in Chapter 4, for spins located on a *fcc* lattice, only four types of commensurate antiferromagnetic order are possible [70]. To determine the direction of the magnetic moment, we compare the intensities of the (110) peak with those of the (001) peak. The intensities observed at these two Bragg spots suggest that the magnetic moment is aligned parallel to the momentum of the incoming neutron beam, along the $[001]$-direction, as can be seen in Fig. 5.5a). Due to the cubic structure of the crystal, the magnetic moment can point along any of the six edges of the cube. Along four of these edges the form factor cancels, leaving only the $[001]$ direction. Therefore we can conclude that the magnetic moment of the Nd^{3+} ion points normal to the $\{100\}$ family of planes forming domains of orientations, where the moment lies along the directions $[100]$, or the equivalent $[010]$, and $[001]$ planes (see Figure 5.6).

This results in ferromagnetic ordered planes with alternating spin direction along the propagation vector $\mathbf{k} = (1, 0, 0)$ as depicted in Figure 5.6. A similar structure has been previously observed in the half-Heusler compound CeBiPt [12]. However, as we have seen in Chapter 3, the magnetic order required for the AFTI phase depends on a net magnetization enclosed by a hopping path that connects two intermediate non-magnetic sites over a magnetic Nd-site, i.e. the net spin in each Nd layer perpendicular to the space diagonal. This net magnetic field seen by electrons hopping between non-magnetic sites, has to be accounted for in the spin-orbit Hamiltonian (see 3.1) with an additional Aharonov-Bohm phase that is proportional to the in-plane magnetization [48]. In the spin arrangement found in NdBiPt two neighbouring spins perpendicular to the space diagonal cancel each other out and result in zero enclosed magnetic flux. Based on these observations we can exclude NdBiPt from the AFTI phase.

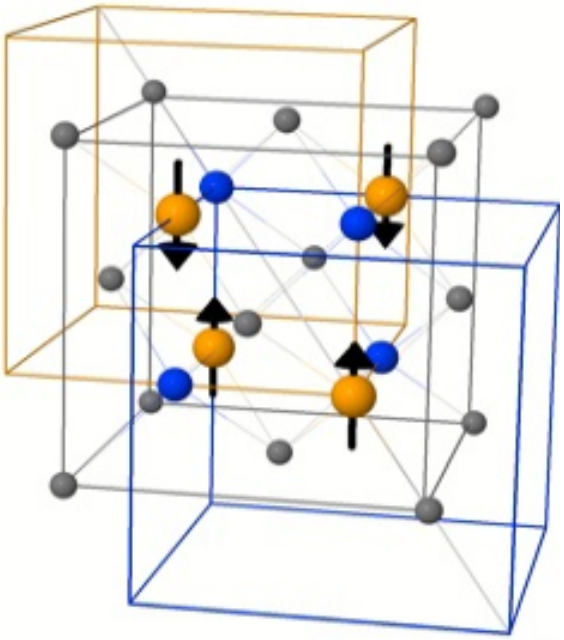

Figure 5.6: Magnetic structure of NdBiPt. Nd atoms are shown in Yellow, Bi in blue and Pt in grey. The moments are arrange in ferromagnetic sheets stacked antiferromagnetically along the propagation vector $\mathbf{k} = (100)$ [9].

The amplitude of the moment was determined by comparing the observed magnetic intensities $F_{\mathrm{mag}}(\mathbf{Q})$ to those of a nearby reciprocal lattice vector $I_N(\tilde{\mathbf{Q}})$ using the relation [84]:

$$|F_{\text{mag}}(\mathbf{Q})|^2 \quad = \quad \frac{I_{\text{mag}}(\mathbf{Q}) \cdot \sin\phi}{C(\tilde{\mathbf{Q}}) \cdot \sin^2(\alpha)} \quad , \tag{5.2}$$

where I_{mag} is the observed intensity, $\sin^2(\alpha) = 1 - (\hat{\tilde{Q}} \cdot \hat{\mathbf{Q}})^2$, ϕ is the scattering angle. $\hat{\tilde{Q}}$ and $\hat{\mathbf{Q}}$ are unit vectors in the direction of the nuclear and magnetic peaks used. $C(\tilde{\mathbf{Q}})$ can be determined from nuclear peaks, by comparing the nuclear structure factor, calculated from tabulated scattering lengths, with the observed intensities:

$$I_N(\tilde{\mathbf{Q}}) \quad = \quad C(\tilde{\mathbf{Q}}) \frac{|F_N(\tilde{\mathbf{Q}})|^2}{\sin\phi} = \frac{|F_N^{\text{obs}}(\tilde{\mathbf{Q}})|^2}{\sin\phi} \quad . \tag{5.3}$$

The magnetic structure factor can be written as [84]:

$$F_{\text{mag}}(\mathbf{Q}) \quad = \quad \frac{\gamma_{\text{n}} r_0}{2} \cdot \mu \dot{f}(\mathbf{Q}) \sum_j e^{2\pi i(hx_j + ky_j + lz_j)} \quad . \tag{5.4}$$

Here, $(\gamma_{\mathbf{n}} r_0/2) = 2.69 \cdot 10^{-15} m/\mu_B^2$ is the product of neutron gyromagnetic ratio, r_0 the electron radius, and μ_{B} the Bohr magneton. To calculate the magnetic form factor $f(\mathbf{Q})$ we used a dipole approximation [85]. Solving for μ results in an ordered magnetic moment of $1.92(1)$ μ_{B} at 1 K on the Nd site, which corresponds to $2.05(9)$ μ_{B} at 0 K. This value is considerably lower than the value of 3.8 μ_{B} obtained from Curie-Weiss analysis of the high-temperature susceptibility data. This reduction can be attributed to crystalline electric field (CEF) effects (see Sec. 5.6).

We also performed a single crystal refinement of the integrated peak intensities using the FullProf Suite [86]. A representational analysis using BasIreps for the space group $F\bar{4}3m$ with a propagation vector k of $(0,0,1)$ of this type-I AFM structure, i.e the decomposition of the magnetic representation in terms of nonzero irreducible representations of all the symmetry groups that leave k invariant, the so-called *little groups*. This analysis results in two sets of basis functions which are listed in Tab. 5.III. The refinement of nuclear

Table 5.III: Real (BASR) and imaginary (BASI) components of the basis vectors for the two permitted commensurable magnetic structures obtained from BasIreps and the resulting RF-factors from the FullProf refinement, for the space group $F\bar{4}3m$ with an ordering wave vector $\mathbf{k}$ of $[0,0,1]$, and Nd^{3+} occupying the $4c$ crystallographic site.

	Set 1	RF-factor	Set 2		RF-factor
BASR	(0 0 1)	11.5	(1 0 0)	(0 1 0)	47.2
BASI	(0 0 0)		(0 0 0)	(0 0 0)	

peaks followed by the magnetic refinement results in a magnetic moment of 1.788 μ_{B} with an RF factor of 11.5, in agreement with our previous analysis. To illustrate this point, we have used the measured magnetic moment to calculate the intensities of other Bragg peaks and compared them with the measured intensities as well as with the values obtained from the refinement. The result of these calculations are shown in Fig. 5.7a). It can be seen, that the (221) peak shows a higher intensity than the (112) peak, as expected for the magnetic structure presented in Figure 5.6. We did observe a small magnetic signal at the (001) position below the critical temperature, as shown in Fig. 5.5(b). We can exclude higher harmonics of the fundamental wavelength as the source of this signal due to the presence of PG filters. This led us to the conclusion that the observed intensity must result from second scattering: The incoming beam is first diffracted by the nuclear $[111]$ plane, as schematically shown in Fig. 5.7(b). The diffracted beam does now allow for a small magnetic intensity at the same position, which would correspond to a (001) magnetic reflection of the primary beam.

An estimate of the strength of a (001) magnetic peak due to secondary scattering can be obtained by using the outgoing flux from the (111) nuclear peak, as the incident beam that causes the (001) reflection. This estimate results in an integrated intensity $I^{\mathrm{calc}}_{(001)} = 1.1 \cdot I^{\mathrm{obs}}_{(001)}$, which is only slightly higher than the observed one, thus substantiating our conjecture. Fig. 5.8a) shows the temperature dependence of the integrated intensity of the (110) magnetic peak as we cross the transition temperature. To obtain the

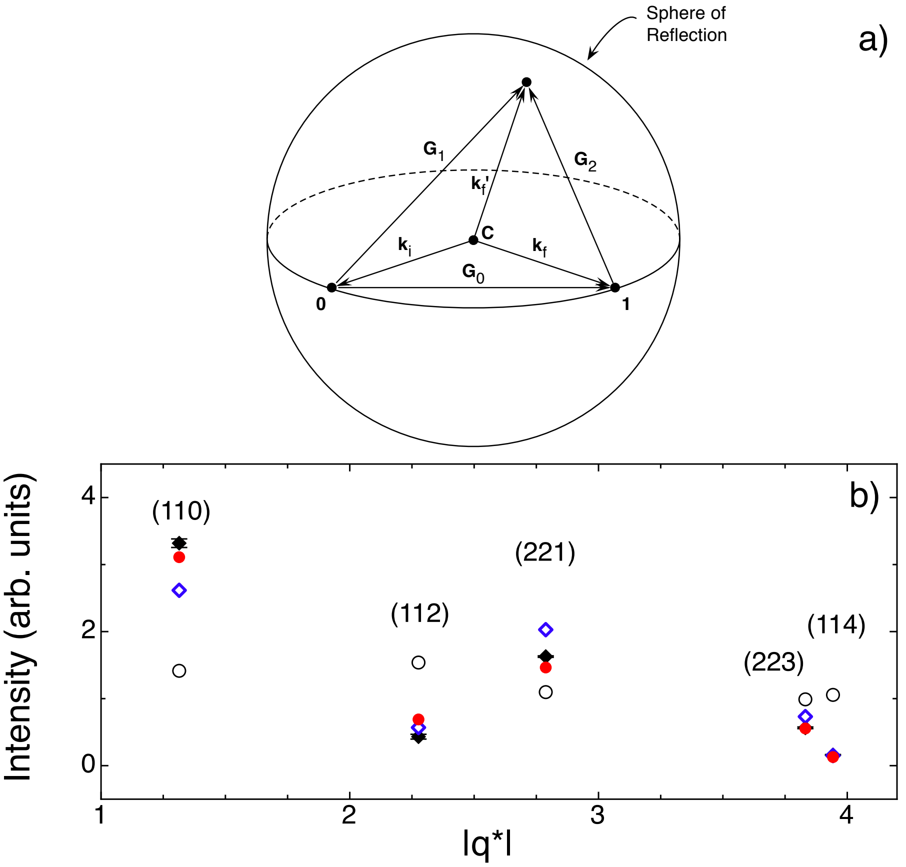

Figure 5.7: a) Neutrons diffracted by $\mathbf{G}_1$ undergo a second scattering by reciprocal lattice vector $\mathbf{G}_2 = \mathbf{G}_0 - \mathbf{G}_1$ [87]. b) Comparison between the calculated (full diamonds) and measured intensities (full circles) for a magnetic moment aligned along the crystallographic c-axis and propagation vector $\mathbf{k}$ of $(1,0,0)$. The open diamonds reflect the refined intensities using FullProf with the correct basis, and the open circles with the wrong basis vector set [9].

Néel temperature of $T_{\mathbf{N}} = 2.177 \pm 0.005$ K, the data was fitted to the scaling law in the temperature range between 1.6 K and 2.3 K (see Fig. 5.8a):

$$I \quad = \quad C \cdot \left(1 - \frac{T}{T_{\mathrm{N}}}\right)^{2\beta} \quad , \tag{5.5}$$

yielding a critical exponent of $\beta = 0.3704 \pm 0.003$, which is close to the value of $\beta = 0.3265$ expected for a three dimensional Heisenberg antiferromagnet [88]. With pure Heisenberg interactions a single-k structure is actually more favourable than any multi-k

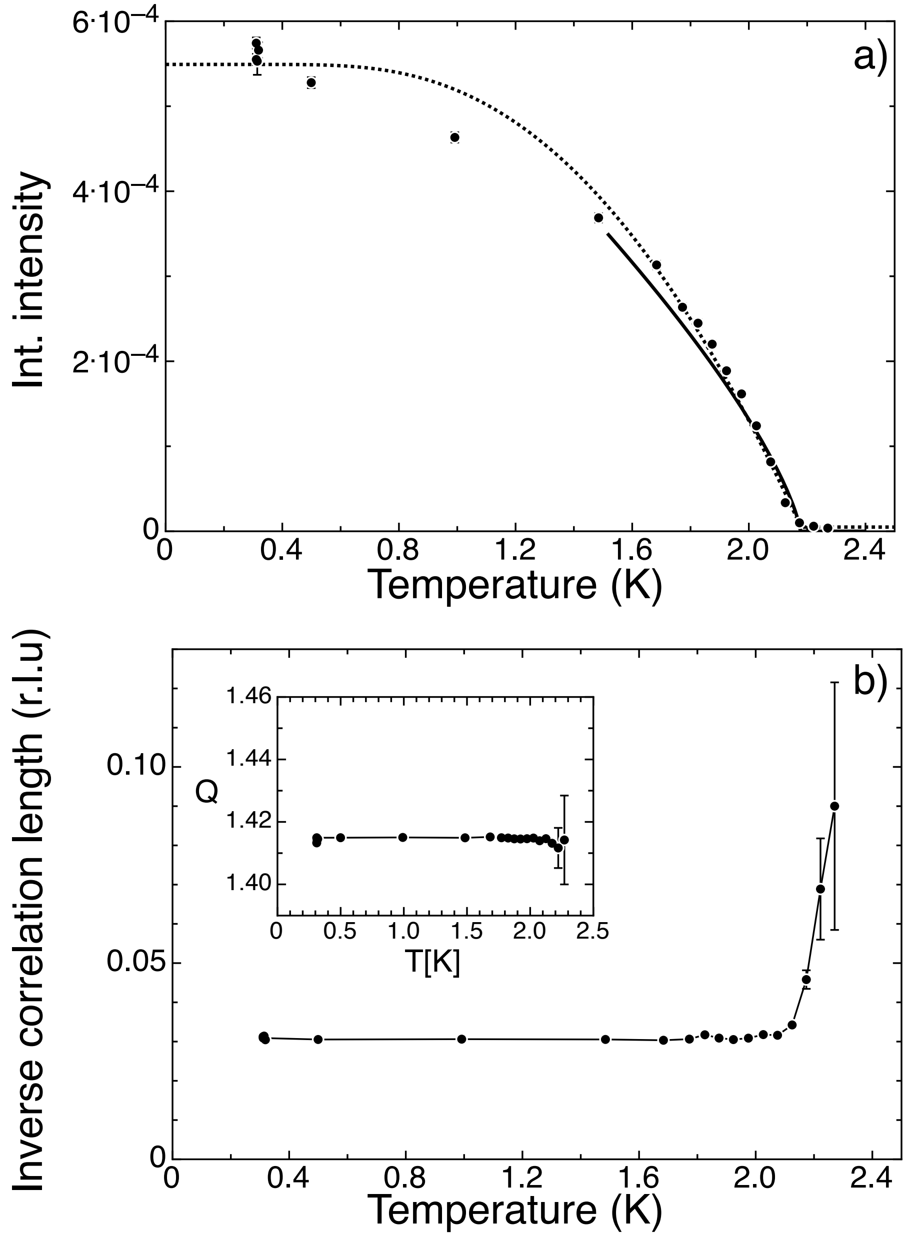

Figure 5.8: a) Temperature dependence of the integrated intensity of the (110) magnetic Bragg reflection. The solid line shows the scaling-law fit of Eq. (5.5) used to determine T_N. The dashed line is fit of the intensity to the Brillouin function of the CEF doublet. b) The solid lines are guides to the eye. Estimate of the inverse correlation length just below the ordering temperature. Inset: Peak position in q-space [9].

structure, which is in accordance with our earlier findings of a single $k = (0,0,1)$ type-I AFM structure [71].

Figure 5.8b) shows the temperature dependence of the Gaussian peak width along the

(110) direction, which is proportional to the average inverse correlation length $1/\xi$. One can see that ξ diverges as we cross the transition temperature, indicating long range order.

5.6 Crystalline Electric Field Effects

As noted in Sec. 5.5, the ordered magnetic moment observed in neutron scattering of 1.78(9) μ_B, is strongly reduced compared to the free ion value of Nd^{3+} of 3.62 μ_B. Such a reduction of the magnetic moment is often observed in inter-metallic compounds due to crystalline electric field (CEF) effects. This behaviour has been also reported for CeBiPt, where the ordered moment corresponds to the magnetic moment of the Γ_8 ground state of the Ce^{3+}-ion [12, 89].

Crystal field theory describes the lifting of degeneracies of electron orbital states in large ions (unfilled d or f orbitals are usually affected), due to a static electric field that is produced by surrounding charges. This field is incorporated into the Hamiltonian in the form of an additional perturbing potential created by all electrons in an unfilled shell. The electronic configuration of rare earth ions is $4f^n 5s^2 5p^6$ with $n = 3$ for Nd^{3+}. Luckily this problem can be radically simplified by respecting symmetries present in the crystallographic lattice. In the case of of NdBiPt, we find a local eightfold cubic symmetry (see Figure 5.9). The potential due to a charge q at $A(a,a,a)$, at a point $P(x,y,z)$ can be written as:

$$\begin{aligned} V_A &= \frac{+q}{[(a-x)^2+(a-y)^2+(a-z)^2]^{1/2}} \qquad (5.6) \\ &= \frac{+q}{A^{1/2}}\left(\frac{1}{1+Y}\right)^{1/2}, \end{aligned}$$

where we have substituted $A = 3a^2 + r^2$ and $\mathrm{Y} = -2a(x+y+z)/A$ and r denoting the distance between point p and the origin. We can expand $(1+\mathrm{Y})^{1/2} = 1 + \frac{1}{2}\mathrm{Y} + \frac{3}{2^3}\mathrm{Y}^2 + \frac{5}{2^4}\mathrm{Y}^3 + \ldots$ and arrive at:

$$V_\mathrm{A} = q\left[\frac{1}{\mathrm{A}^{1/2}} + \frac{a(x+y+z)}{\mathrm{A}^{3/2}} + \frac{3}{2}\frac{a^2(x+y+z)^2}{\mathrm{A}^{5/2}} + \ldots\right]. \qquad (5.7)$$

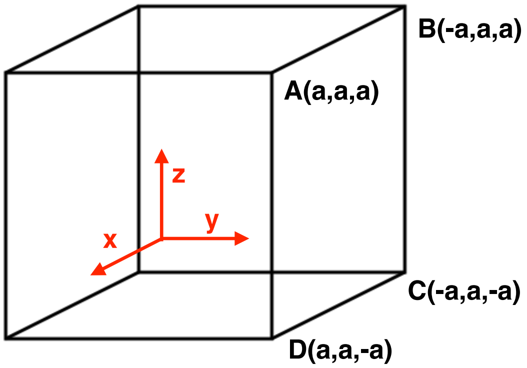

Figure 5.9: Locally we find an eightfold cubic symmetry. An electron at a point (x,y,z) is exposed to the field of eight point charges.

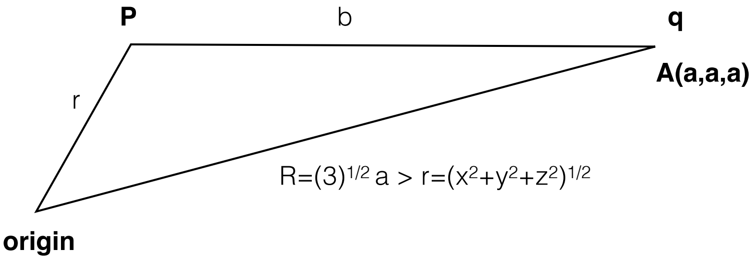

Figure 5.10: Schematic of the potential at a point $\mathrm{P}(x,y,z)$ due to a charge q at $\mathrm{A}(a,a,a)$.

If we further substitute $\mathrm{X} = \frac{r^2}{3a^2}$, A becomes $\mathrm{A} = 3a^2(1+\mathrm{X})$ and for each term in the expansion 5.7 we can rewrite:

$$
\begin{aligned}
\mathrm{I} &= \frac{1}{(3a^2)^{1/2}}(1+\mathrm{X})^{-1/2} && (5.8)\\
&= \frac{1}{(3a^2)^{1/2}}\left[1-\frac{1}{2}\frac{(x^2+y^2+z^2)}{3a^2}+\frac{3}{8}\frac{(x^2+y^2+z^2)^2}{9a^4}-\frac{5}{2^4}\frac{(x^2+y^2+z^2)^3}{27a^6}+\dots\right]\\
\mathrm{II} &= \frac{a}{(3a^2)^{3/2}}(x+y+z)(1+\mathrm{X})^{-3/2}\\
&= \frac{a}{(3a^2)^{3/2}}\left[(x+y+z)-\frac{1}{2}\frac{(x^2+y^2+z^2)(x+y+z)}{2a^2}\right. && (5.9)\\
&\quad\left.+\frac{5}{24a^4}(x^2+y^2+z^2)^2(x+y+z)+\dots\right]\\
\mathrm{III} &= \frac{3}{2}\frac{a^2}{(3a^2)^{5/2}}(x+y+z)^2(1+\mathrm{X})^{-5/2}\\
&= \frac{3}{2}\frac{a^2}{(3a^2)^{5/2}}\left[(x+y+z)^2-\frac{5}{6a^2}\frac{(x^2+y^2+z^2)(x+y+z)^2}{2a^2}\right. && (5.10)\\
&\quad\left.+\frac{35}{8\cdot 9a^4}(x^2+y^2+z^2)^2(x+y+z)^2+\dots\right].
\end{aligned}
$$

Now we want to add the potentials due to the other 7 charges in the unit cell. Having a cubic symmetry simplifies our problem. For example, the potential at the position (x,y,z) due to a charge at $(-a,a,a)$ is identical to the one at $(-x,y,z)$ due to a charge at (a,a,a). We therefore have to respect the symmetry $x \to -x$ when we add up terms in 5.7. For all charges the potential will be the sum of all terms arising from the different combinations of $\pm x, \pm y, \pm z$, or in other words, all odd degree terms have to cancel out. Also all terms with an odd total power of x,y,z have to cancel out.

The relevant terms in 5.7 up to 6^{th} degree are ([90]):

$$\begin{aligned}
V_{\mathrm{A}} &= q\Bigg\{\frac{1}{(3a^2)^{1/2}}+\left[\frac{-1}{(3a^2)^{3/2}}(x^2+y^2+z^2)+\frac{3}{2}\frac{a^2}{(3a^2)^{5/2}}(x+y+z)^2\right] \qquad (5.11)\\
&+\left[\frac{3}{8\cdot 9a^4}(x^2+y^2+z^2)^2-\frac{3}{2}\frac{a^2}{(3a^2)^{5/2}}\frac{5}{6a^2}(x^2+y^2+z^2)(x+y+z)^2\right.\\
&\left.+\frac{35}{8}\frac{a^4}{(3a^2)^{9/2}}(x+y+z)^4\right]\\
&+\left[-\frac{1}{(3a^2)^{1/2}}\frac{5}{2^4}\frac{(x^2+y^2+z^2)^3}{27a^6}+\frac{3}{2}\frac{a^2}{(3a^2)^{5/2}}\frac{35}{8\cdot 9a^4}(x^2+y^2+z^2)^2(x+y+z)^2\right.\\
&\left.-\frac{35a^4}{8(3a^2)^{9/2}}\frac{9}{6a^2}(x^2+y^2+z^2)(x+y+z)^4+\frac{231}{2^4}\frac{a^6}{(3a^2)^{13/2}}(x+y+z)^6\right]\Bigg\}
\end{aligned}$$

Replacing $d=\sqrt{3}a$ (see Fig. 5.10) and then collecting all terms that are not constants (because they only change the zero point energy) will let us express the potential energy of a charge q' at (x,y,z) ([90]):

$$\begin{aligned}
W_c &= \mathrm{C}_4\left[(x^4+y^4+z^4)-\frac{3}{5}r^4\right]+\mathrm{D}_6\left[(x^6+y^6+z^6)\right. \qquad (5.12)\\
&\left.+\frac{15}{4}(x^2y^4+x^2z^4+y^2x^4+y^2z^4+z^2x^4+z^2y^4)-\frac{15}{14}r^6\right],
\end{aligned}$$

Where we have used the standard notation for the coefficients:

$$\mathrm{C}_4 = -\frac{70qq'}{9d^5} \qquad (5.13)$$

$$\mathrm{D}_6 = -\frac{224qq'}{9d^7}. \qquad (5.14)$$

5.6.1 Stevens operator equivalent method

With equation 5.12 we have the perturbing part of our Hamiltonian that describes the effect of a crystalline electric field in a cubic symmetry. We can now calculate the matrix elements of this perturbing Hamiltonian between free-ion states; the eigenvalues of such a matrix will then describe the energy levels after the lifting of degeneracy of the free ion in the CEF. The most convenient way to evaluate such matrix elements is the use of an “operator equivalent" ([90]) to the Hamiltonian 5.12, built of angular momentum operators that act on the angular part of the wave function in the coupled system ([90]). The i dea is an application of the Wigner-Eckhart theorem and can be understood the following way: For a cartesian function $f(x,y,z)$ to find the operator equivalent to such terms as $\sum_i f_i(x_i,y_i,z_i)$ occuring in the perturbing Hamiltonian, one can replace x,y and z by the operators J_x,J_y and J_z, always allowing for the noncommutation of J_x,J_y and J_z. This can be achieved by replacing products of x,y,z by an expression consisting of all different combinations of J_x,J_y and J_z, normalized by the total number of combinations. A full description of the process can be found in [91]; due to the fcc structure of NdBiPt, we can restrict the formalism to an eighthfold cubic symmetry. The operator formed in this process has the same rotational symmetry as the potential. As a simple example, we can express the following sum as an operator using the factorial of J (permutations without repetitions)

$$\sum_i (3z_i^2 - r_i^2) \equiv \alpha_J \langle r^2 \rangle [3J_z^2 - J(J+1)] = \alpha_j \langle r^2 \rangle O_2^0] \tag{5.15}$$

O_n^m are called Stevens operators and can be found tabulated (for example in [90]). α_j is a numerical constant only depending on the orbital quantum number of electrons in unfilled shells and can be found in the same tables, denoted as β_j for 4^{th} degree terms and as γ_j for 6^{th} degree terms.

So the matrix elements of the sum $\sum_i (3z_i^2 - r_i^2)$ between coupled states $|LSJJ_z\rangle$ are equal to those of $\alpha_j \langle r^2 \rangle O_2^0$ between the angular part of the coupled wave functions.

$$\langle LSJJ_z'| \sum_i (3z_i^2 - r_i^2) \, |LSJJ_z\rangle \equiv \alpha_J \langle r^2 \rangle \, \langle LSJJ_z'| \, [3J_z^2 - J(J+1)] \, |LSJJ_z\rangle \,. \tag{5.16}$$

If we now return to our perturbing Hamiltonian 5.12, we can rewrite it using Stevens operators:

$$H_{\text{CEF}} = B_4\big(O_4^0 + 5O_4^4\big) + B_6\big(O_6^0 + 21O_6^4\big), \tag{5.17}$$

B_n are the CEF amplitudes. For the case of a $J = \frac{9}{2}$ Nd^{3+}-multiplet, they describe the admixture between the $|\pm\frac{9}{2}\rangle \ldots |\pm\frac{1}{2}\rangle$ states,

$$\begin{aligned} B_4 &= \frac{7}{18}\frac{|e|q}{d^5}\beta_j\langle r^4\rangle && (5.18)\\ B_6 &= -\frac{1}{9}\frac{|e|q}{d^7}\gamma_j\langle r^6\rangle. && (5.19) \end{aligned}$$

5.6.2 Schottky anomaly

If we calculate the effect of a crystalline electric field for the Nd^{3+} ion sitting in the cubic environment of the NdBiPt magnetic lattice, the CEF splitting is expected to result in a new ground state consisting of a Γ_6 doublet, and two quartets, $\Gamma_8^{(1)}$ and $\Gamma_8^{(2)}$, by lifting the 10-fold degeneracy of the $J = \frac{9}{2}$ multiplet (These calculations have been performed using a Mathematica routine that can be found in Appendix I).

To further investigate the conjecture that the reduction of the magnetic moment might be due to CEF, we carried out specific heat measurements in zero field over a temperature range from 0.3 to 30 K. The total specific heat $C_p = C_{\mathrm{el}} + C_{\mathrm{ph}} + C_{\mathrm{mag}}$, consists of an electronic contribution $C_{\mathrm{el}} = \gamma T$, the phonon contribution C_{ph}, and the magnetic contribution C_{mag} we are interested in. Due to the large phonon C_{ph} and magnetic C_{mag} contributions

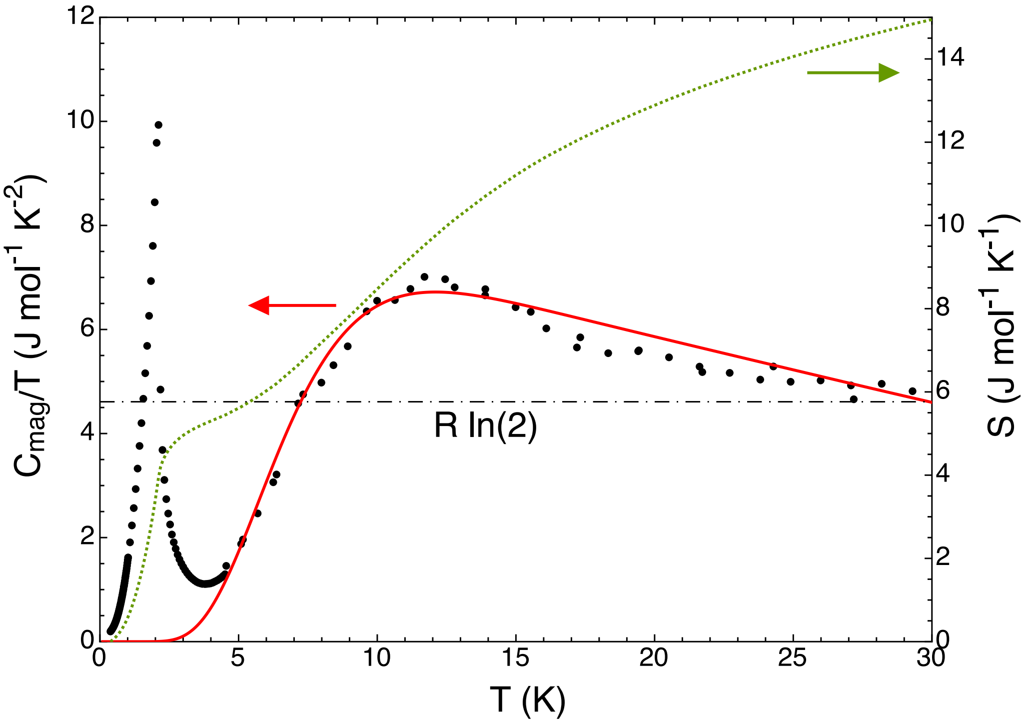

Figure 5.11: Magnetic contribution to the specific heat C_{mag} shown as $\frac{C_{\mathrm{mag}}}{T}$ vs. T. The solid line is the best fit of Eq. 5.24 to a Schottky anomaly by using all possible energy eigenvalue configurations obtained by solving the CEF Hamiltonian. The dotted line shows the temperature dependence of the magnetic entropy S_{mag}, which displays a plateau at $R\ln 2$ between 3 K and 5 K, indicating the Γ_6 doublet of the CEF ground state [9].

in the measured temperature range, we were not able to determine the electronic contribution C_{el} that is at maximum of the order of 1 mJ mol^{-1} K^{-2}. Such a low value for C_{el} is expected due to the low carrier concentration in NdBiPt.

Over the measured temperature range, C_{ph} can be described by the equation:

$$C_{\mathrm{ph}} \;=\; 9R\left(\frac{T}{\theta_{\mathrm{D}}}\right)^{3}\int_{0}^{\frac{\theta_{\mathrm{D}}}{T}}\frac{x^{4}e^{x}}{(e^{x}-1)^{2}}dx\,. \tag{5.20}$$

As can be seen in Fig. 5.11 we observe a rather broad magnetic peak between 4.5 K and 20 K, which makes it difficult to fit the the phonon contribution. We chose to use the θ_D value of 122.3 K obtained from a fit of Eq. 5.20 to the specific heat data of GdBiPt, which does not have CEF [10]. We then scaled this Debeye temperature with the square root of the inverse mass ratio between Gd and Nd. This yields a Debye temperature of $\theta_D = 123.7$ K for NdBiPt. Fig. 5.11 shows the magnetic contribution $C_{\mathrm{mag}} = C_p - C_{\mathrm{ph}}$ to the specific heat C_p after subtraction of the phonon contribution C_{ph}. By integrating the magnetic specific heat C_{mag}, we can obtain the magnetic entropy

$$S_{\mathrm{mag}} = \int_{0}^{T}\frac{C_{\mathrm{mag}}}{T}dT, \tag{5.21}$$

associated with the CEF ground state which orders. The magnetic entropy shows a plateau at $R\ln 2$ corresponding to a doublet ground state.

To analyze the splitting of our degenerate ground state due to the crystalline electric field we search for solutions of the perturbation Hamiltonian for an eightfold cubic symmetry. For an f-electron configuration, terms up to sixth degree are sufficient [92], so we can use the perturbing Hamiltonian from the last section, given by Equation 5.12:

$$H_{\mathrm{CEF}} \;=\; B_4\left(O_4^0+5O_4^4\right)+B_6\left(O_6^0+21O_6^4\right) \quad , \tag{5.22}$$

To determine the ratio between the fourth- and sixth- degree terms, we substitute $O_4 = O_4^0 + 5O_4^4$ and $O_6 = O_6^0 + 21O_6^4$. This allows us to rewrite Eq. 5.22 as [92]:

$$H_{\text{CEF}} = W\left[x\frac{O_4}{F(4)} + (1-|x|)\frac{O_6}{F(6)}\right] \quad , \tag{5.23}$$

where $B_4F(4) = Wx$ and $B_6F(6) = W(1-|x|)$ for $-1 < x < +1$. Now we can fit the magnetic part of the specific heat S_{mag} for different values of x and W (see Fig. 5.12) in terms of a Schottky anomaly:

$$\begin{aligned} C_{\text{CEF}} = \frac{R}{T^2}\Bigg[&\frac{4\Delta_1^2 e^{-\frac{\Delta_1}{T}} + 4\Delta_2^2 e^{-\frac{\Delta_2}{T}}}{2+4e^{-\frac{\Delta_1}{T}} + 4e^{-\frac{\Delta_2}{T}}} \\ &-\left(\frac{4\Delta_1 e^{-\frac{\Delta_1}{T}} + 4\Delta_2 e^{-\frac{\Delta_2}{T}}}{2+4e^{-\frac{\Delta_1}{T}} + 4e^{-\frac{\Delta_2}{T}}}\right)^2\Bigg]. \end{aligned} \tag{5.24}$$

For Nd^{3+} with a $J = 9/2$ the 10 fold degenerate ground state is lifted into a doublet Γ_6 as the ground state and the two quadruplets $\Gamma_8^{(1)}$ and $\Gamma_8^{(2)}$, which are separated by an energy gap of Δ_1, and Δ_2, respectively. We obtain a best fit shown as the solid line in Fig. 5.11 for $\Delta_1 = 29$ K and $\Delta_2 = 72$ K, which corresponds to two possible combinations of x and W; $x_1 = 0.139$, $W_1/k_B = 0.774$ K and $x_2 = -0.965$ and $W_1/k_B = 1.141$ K.

Knowing the values of x and W allows us to calculate the expected value for the magnetic moment of the Γ_6 doublet. This calculation yields a theoretical value of 1.833 μ_{B} for the ordered moment, for both combinations of x and W, which is close to the $1.78(9)$ μ_{B} obtained from neutron diffraction.

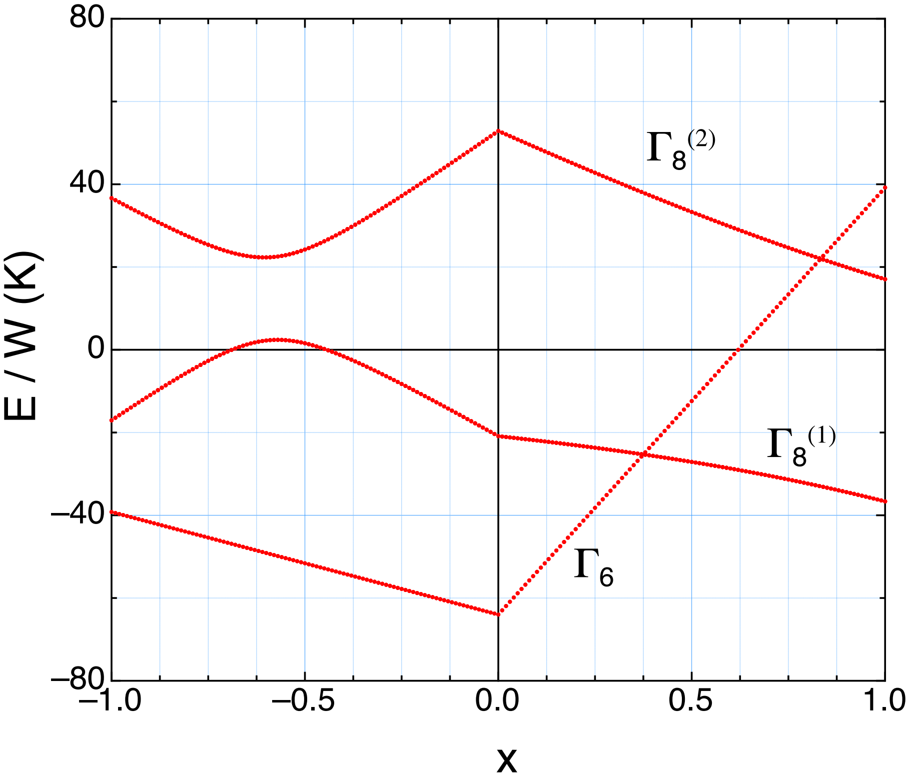

Figure 5.12: Solutions of the CEF Hamiltonian scaled by W (Eq. 5.23), for different x between -1 and 1 [9].

5.7 Conlusions

We determined the magnetic structure of the semi-metal NdBiPt, which crystallizes in a half-Heusler structure. Below the Néel temperature T_N of 2.18 K we find an up-down structure of ferromagnetically aligned planes, in which the spin of the Nd points along [001] direction, that alternate along the propagation vector $\mathbf{k} = (100)$. As pointed out by Wosnitza *et al.*, [12] this *type-I* structure is common for crystals belonging to the space group $F\bar{4}3m$. This suggests the following question: Why in GdBiPt [10, 79], YbBiPt, and vanadium doped CuMnSb [74, 93] does the propagation vector of the antiferromagnetic structure point along [111]? However, the magnetic structure we found in NdBiPt excludes this material from being a candidate for the new class of antiferromagnetic topological insulator [48]. In NdBiPt, the ground state is the Γ_6 CEF doublet which orders, and we find an ordered moment of $1.78(9)\ \mu_\mathrm{B}$.

5.8 Contributions

All samples for this experiment I grew with help from Alexandre Desilets-Benoit and Luc Lapointe. Powder X-ray measurements where performed by Nicholas Gauthier. The single crystal X-ray analysis was performed by Thiery Maris from the department of chemistry at UdeM. The single crystal neutron diffraction study was performed together with Alexandre Desilets-Benoit at the Canadian Neutron Beam Centre, Chalk River, Ontario where Zarah Yamani acted as our local contact.

CHAPTER 6

CONCLUSION AND OUTLOOK

This thesis presents the results of a full structural and magnetic analysis on GdBiPt and NdBiPt, both candidate materials for a new antiferromagnetic topological insulator phase. For both materials single-crystal X-ray experiments were conducted to confirm the $F\bar{4}3m$ half-Heusler nuclear structure. Hall measurements in GdBiPt revealed an anomalous kink around 25 K, followed by a steeper increase in $R_{\mathbf{H}}$. A similar behaviour has been observed in CeBiPt [94], with the difference that the kink appeared at the Néel temperature. The authors ascribed this effect to the fformation of a superzone gap in the ordered state, but since we see this behaviour well above the AFM transition in GdBiPt, we have to conclude that it is most certainly not linked to the magnetic order. A powder neutron scattering study on GdBiPt revealed a magnetic moment of $7.6\mu_{\mathbf{B}}$ at 0 K, very close to the value of $7.97\mu_{\mathbf{B}}$, which was obtained from magnetic susceptibility measurements, proving that for the $4f^7$ configuration (angular momentum $L = 0$) of Gd^{3+}, crystalline electric fields don't play a significant role.

In the case of NdBiPt, a single-crystal neutron scattering study revealed an antiferromagnetic transition at the Néel temperature of $T_{\mathbf{N}} = 2.18$ K, with a magnetic moment of $1.78\mu_{\mathbf{B}}$ at 0 K, lower then the expected moment of $3.8\mu_{\mathbf{B}}$ obtained from a Curie-Weiss analysis of the high temperature susceptibility data taken. This lowering of the moment could be ascribed to the splitting of the ground state due to crystalline electric fields. This splitting leads to a new doublet ground state that manifests itself also in the from of a Schottky anomaly in the specific heat and in the form of a plateau around $S = \mathbf{R}\ln(2)$ in the entropy of NdBiPt. Solving the crystal field Hamiltonian for this Schottky peak led to a theoretical value of the magnetic moment of $1.833\mu_{\mathbf{B}}$ which is in good agreement with the results from the neutron scattering study.

To see if the two materials qualify for the antiferromagnetic topological insulator phase, a full magnetic analysis was performed in both cases. GdBiPt reveals the desired type-II antiferromagnetic structure (see Figure 4.6), with ferromagnetic sheets stacked antiferromagnetically along the space diagonal of the half-Heusler structure, resulting in a propagation vector $\mathbf{k} = (\frac{1}{2}, \frac{1}{2}, \frac{1}{2})$. As outlined in Chapter 3, theory predicts a mechanism behind a band inversion, driven by a specific antiferromagnetic order, which increases spin-orbit coupling for inter-plane electron hopping. The magnetic structure found for GdBiPt maximizes this effect, making it a strong candidate for this new phase of matter.

As for NdBiPt a type-I AFM structure was found with a propagation vector $\mathbf{k} = (1, 0, 0)$. In this structure the magnetic moment is aligned with the $(1, 0, 0)$ crystallographic axis forming ferromagnetic sheets stacked antiferromagnetically along the (1,0,0) direction, and therefore we find opposite spin components along the space diagonal, cancelling each other out. This structure results in a zero magnetization perpendicular to the hopping path that connects two intermediate non-magnetic sites over a Nd-site and therefore excludes NdBiPt from the ATFI phase.

quid nunc?

The topological insulating state is one of the great discoveries in physics of the past decade and even though we have already learned a lot in a brief period of time about this new fundamental state of matter, many challenges have yet to be overcome when it comes to experimental means of probing it.

One of the main problems researchers face when working on topological insulators, is the fact that all known represents are bad insulators, i.e. we have seen in Chapter 2 that a small band gap is a necessary prerequisite for a compound to inhere topologically non-trivial features, a fact that makes transport experiments very challenging and often has limited our possibilities in probing new materials by means other than ARPES technologies. Due to the bad band insulating characteristics, weak transport signals from the metallic surface are overshadowed by bulk electrons.

If on the other hand the topological phase is bound to another broken-symmetry, as suggested for the AFTI state, or as in SmB_6 where the transition from a Kondo lattice to a gapped insulating bulk with topologically protected surface states has been observed [95, 96], we can find new methods for separating bulk from surface signal. The additional broken symmetry state allows us to turn on or off the topological phase and one can look at the surface signal with respect to a topologically trivial reference.

We also have to think about new and simple means when it comes to testing possible candidate materials for their topological properties, that go beyond ARPES, a technique that is limited to large research facilities. During my PhD it has always puzzled me how to best approach this problem. One elegant solution is to make transport measurements on a sample of unorthodox shape, as successfully shown by Kim *et al.* [95] with Hall measurements on a sample of SmB_6 in the shape of a wedge, so that the hall conductivity can be put into relation with the wedges thickness. Another interesting approach came from Wolgast *et al.*. By mounting a thin sample plate of SmB_6 perpendicular to the sample holder and contact it on the front and the back, they where able to separate bulk from surface conductance [97].

During the past year we have worked on another, promising and very applicable procedure to test a material for its topological character. The basic idea is to use a common Raman setup that can be found in most physics labs. We are looking for a Raman response which will show an amplified signal due to resonant inter-band transmissions between bulk bands and surface Dirac cones whose intensity depends on the direction of the polarization of the excitation as well as the analyzer. One of the properties of topological insulators is that the spins of the surface states have a chiral symmetry, leading to a helical alignment of the spins on the circle, where the Fermi surface cuts the Dirac cone. This should in principle allow us to probe these states by using circular polarized light as excitation. We can induce resonant optical inter-band transitions from the bulk valence band to the surface Dirac cones. As such a transition requires a spin flip, incoming light with a circular polarization should result in the emission of a photon with the opposite polarization. The probability of these inter-band transitions depends on both, the polarization and the energy of the excitation. From band structure calculation and ARPES measurements we have a good understanding of the electronic band structure. As schematically outlined in Figure 6.1, we can estimate the wavelength required in such an experiment. Raman measurements on the conventional topological insulator Bi_2Se_3 have already shown promising results that support our conjecture [98], but certainly more work is needed to cement it.

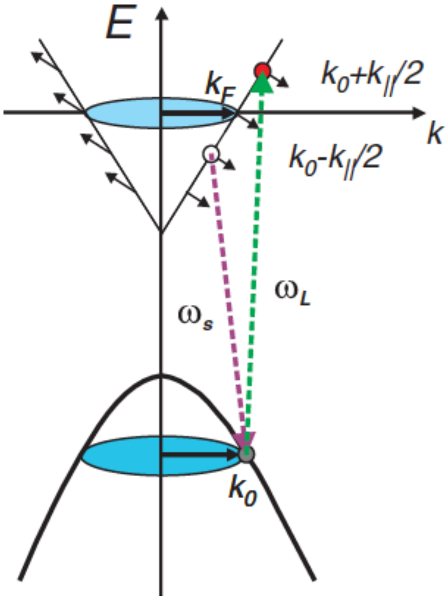

Figure 6.1: Electrons from a bulk band at k_0 are excited to a Dirac surface cone near the Fermi energy, leading to fluctuations of the particle-hole continuum which are probed at resonance [98].

From an experimental point of view, we can use the fact that in SmB_6 and also in GdBiPt the topological phase is bound to another phase transition. By changing the temperature above and beyond the critical value where the phase transition occurs, we will be able to experimentally prove that this technique can be reliable. To date, measurements are still being taken and no results are therefore included in this thesis. Our hope is that this experiment will provide enough experimental evidence to introduce Raman spectroscopy as a new technique for preliminary probing new topological insulators.

BIBLIOGRAPHY

[1] D.J.Thouless et M.Komoto, *Quatized Hall Conductance in a Two-Dimensional Periodic Potential*, Phys. Rev. Lett. **49**, 405 (1982).

[2] B. A. Bernevig, T. L. Hughes, et S.-C. Zhang, *Quantum Spin Hall Effect and Topological Phase Transition in HgTe Quantum Wells*, Science **314**, 1757 (2006).

[3] M. Konig, S. Wiedmann, C. Brune, A. Roth, H. Buhmann, L. W. Molenkamp, X.-L. Qi, et S.-C. Zhang, *Quantum Spin Hall Insulator State in HgTe Quantum Wells*, Science **318**, 766 (2007).

[4] J. E. Moore, *The birth of topological insulators.*, Nature **464**, 194 (2010).

[5] M. Z. Hasan et C. L. Kane, *Colloquium: Topological insulators*, Rev. Mod. Phys. **82**, 3045 (2010).

[6] D. Xiao, Y. Yao, W. Feng, J. Wen, W. Zhu, X.-Q. Chen, G. Stocks, et Z. Zhang, *Half-Heusler Compounds as a New Class of Three-Dimensional Topological Insulators*, Physical Review Letters **105**, 96404 (2010).

[7] D. Hsieh, Y. Xia, L. Wray, D. Qian, A. Pal, J. H. Dil, J. Osterwalder, F. Meier, G. Bihlmayer, C. L. Kane, Y. S. Hor, R. J. Cava, et M. Z. Hasan, *Observation of unconventional quantum spin textures in topological insulators.*, Science **323**, 919 (2009).

[8] H.-J. Zhang, C.-X. Liu, X.-L. Qi, X.-Y. Deng, X. Dai, S.-C. Zhang, et Z. Fang, *Electronic structures and surface states of the topological insulator* $Bi_{1-x}Sb_x$, Physical Review B **80**, 1 (2009).

[9] R. A. Müller, A. Désilets-Benoit, N. Gauthier, L. Lapointe, A. D. Bianchi, et T. Maris, *Magnetic structure of the antiferromagnetic half-Heusler compound NdBiPt*, arXiv preprint (2015), 1503.04487v1.

[10] R. A. Müller, N. R. Lee-Hone, L. Lapointe, D. H. Ryan, T. Pereg-Barnea, A. D. Bianchi, Y. Mozharivskyj, et R. Flacau, *Magnetic structure of GdBiPt: A candidate antiferromagnetic topological insulator*, Physical Review B **90**, 041109 (2014).

[11] G. Goll, J. Hagel, H. v. Löhneysen, T. Pietrus, S. Wanka, J. Wosnitza, G. Zwicknagl, T. Yoshino, T. Takabatake, et A. G. M. Jansen, *Temperature-dependent Fermi surface in CeBiPt*, Europhysics Letters **57**, 233 (2002).

[12] J. Wosnitza, G. Goll, A. D. Bianchi, B. Bergk, N. Kozlova, I. Opahle, S. Elgazzar, M. Richter, O. Stockert, H. V. Löhneysen, T. Yoshino, et T. Takabatake, *Magnetic-field- and temperature-dependent Fermi surface of CeBiPt*, New J. Phys. **8**, 174 (2006).

[13] N. Butch, P. Syers, K. Kirshenbaum, A. Hope, et J. Paglione, *Superconductivity in the topological semimetal YPtBi*, Physical Review B **84**, 1 (2011).

[14] T. V. Bay, T. Naka, Y. K. Huang, et A. de Visser, *Superconductivity in noncentrosymmetric YPtBi under pressure*, Physical Review B **86**, 064515 (2012).

[15] T. Bay, M. Jackson, C. Paulsen, C. Baines, A. Amato, T. Orvis, M. Aronson, Y. Huang, et A. de Visser, *Low field magnetic response of the non-centrosymmetric superconductor YPtBi*, Solid State Communications **183**, 13 (2014).

[16] F. F. Tafti, T. Fujii, A. Juneau-Fecteau, S. René de Cotret, N. Doiron-Leyraud, A. Asamitsu, et L. Taillefer, *Superconductivity in the noncentrosymmetric half-Heusler compound LuPtBi: A candidate for topological superconductivity*, Physical Review B **87**, 184504 (2013).

[17] E. Hall, *On a new action of the magnet on electric currents*, American Journal of Mathematics **2**, 287 (1879).

[18] H. Smith, *Introduction to Quantum Mechanics* (World Scientific Publishing Co., 1991).

[19] J. Weis et K. von Klitzing, *Metrology and microscopic picture of the integer quantum Hall effect*, Philosophical Transactions of the Royal Society A: Mathematical, Physical and Engineering Sciences **369**, 3954 (2011).

[20] R. Laughlin, *Quantized Hall conductivity in two dimensions*, Physical Review B **23**, 1 (1981).

[21] O. Taylor, P. L., Heinonen, *A Quantum Approach to Condensed Matter Physics* (Cambridge, Cambridge, 2002).

[22] P. Chakraborty, T. Pietilainen, *No TitleThe Quantum Hall Effects* (Springer Berlin / Heidelberg, 1995).

[23] D. Yoshioka, *The Quantum Hall Effect* (Springer Berlin Heidelberg, 1987).

[24] J. von Bergmann et H. von Bergmann, Foucault pendulum through basic geometry, 2007.

[25] J. Oprea, *Geometry and the Foucault pendulum*, Am. Math. Monthly **102**, 515 (1995).

[26] M. Berry, *Quantal phase factors accompanying adiabatic changes*, Proceedings of the Royal Society of **392**, 45 (1984).

[27] R. Kubo, S. J. Miyake, et N. Hashitsume, *Quantum Theory of Galvanomagnetic Effect at Extremely Strong Magnetic Fields*, Solid State Physics - Advances in Research and Applications **17**, 269 (1965).

[28] Q. Niu et D. Thouless, *Quantized Hall conductance as a topological invariant*, Phys. Rev. B **31**, 3372 (1985).

[29] J. Avron et D. Osadchy, *A topological look at the quantum Hall effect*, Physics today (2003).

[30] B. Halperin, *Quantized Hall conductance, current-carrying edge states, and the existence of extended states in a two-dimensional potential*, Physical Review B **25** (1982).

[31] X.-l. Qi et S.-c. Zhang, *The quantum spin Hall effect and topological insulators*, p. 7 (2010), 1001.1602.

[32] X.-L. Qi et S.-C. Zhang, *Topological insulators and superconductors*, Reviews of Modern Physics **83**, 1057 (2011).

[33] C. L. Kane et E. J. Mele, *Z_2 Topological Order and the Quantum Spin Hall Effect*, Physical Review Letters **95**, 3 (2005).

[34] X.-L. Qi et S.-C. Zhang, *Spin-Charge Separation in the Quantum Spin Hall State*, Physical Review Letters **101**, 1 (2008).

[35] B. Zhou, H.-Z. Lu, R.-L. Chu, S.-Q. Shen, et Q. Niu, *Finite Size Effects on Helical Edge States in a Quantum Spin-Hall System*, Physical Review Letters **101**, 246807 (2008).

[36] J. Linder, T. Yokoyama, et A. Sudbø, *Anomalous finite size effects on surface states in the topological insulator Bi_2Se_3*, Physical Review B **80**, 205401 (2009).

[37] H.-Z. Lu, W.-Y. Shan, W. Yao, Q. Niu, et S.-Q. Shen, *Massive Dirac fermions and spin physics in an ultrathin film of topological insulator*, Physical Review B **81**, 115407 (2010).

[38] B. Buttner, C. Liu, G. Tkachov, et E. Novik, *Single valley Dirac fermions in zero-gap HgTe quantum wells*, Nature Physics , 1 (2011), arXiv:1009.2248v2.

[39] C. Wu, B. A. Bernevig, et S.-c. Zhang, *Helical Liquid and the Edge of Quantum Spin Hall Systems*, **106401**, 1 (2006).

[40] M. König, S. Wiedmann, C. Brüne, A. Roth, H. Buhmann, L. W. Molenkamp, X.-L. Qi, et S.-C. Zhang, *Quantum spin hall insulator state in HgTe quantum wells.*, Science (New York, N.Y.) **318**, 766 (2007), 0710.0582.

[41] L. Fu, C. Kane, et E. Mele, *Topological Insulators in Three Dimensions*, Physical Review Letters **98**, 1 (2007).

[42] J. Moore et L. Balents, *Topological invariants of time-reversal-invariant band structures*, Physical Review B **75**, 3 (2007).

[43] R. Roy, *Topological phases and the quantum spin Hall effect in three dimensions*, Physical Review B **79**, 1 (2009).

[44] H. Zhang, C.-X. Liu, X.-L. Qi, X. Dai, Z. Fang, et S.-C. Zhang, *Topological insulators in Bi_2Se_3, Bi_2Te_3 and Sb_2Te_3 with a single Dirac cone on the surface*, Nature Physics **5**, 438 (2009).

[45] R. Winkler, *Spin-orbit coupling effects in two-dimensional electron and hole systems*, (2003).

[46] S. Shen, *Topological insulators: Dirac equation in condensed matters* (Springer Series in Solid-State Sciences, 2013).

[47] L. Fu et C. Kane, *Time reversal polarization and a Z_2 adiabatic spin pump*, Physical Review B **74**, 195312 (2006).

[48] R. Mong, A. Essin, et J. Moore, *Antiferromagnetic topological insulators*, Physical Review B **81**, 245209 (2010).

[49] C. Fang, M. J. Gilbert, et B. A. Bernevig, *Topological insulators with commensurate antiferromagnetism*, Phys. Rev. B **88**, 085406 (2013).

[50] C. L. Kane et E. J. Mele, *Quantum Spin hall effect in graphene*, Physical Review Letters **95**, 226801 (2005), 0411737v2.

[51] S. Chadov, X. Qi, J. Kübler, G. H. Fecher, C. Felser, et S. C. Zhang, *Tunable multifunctional topological insulators in ternary Heusler compounds*, Nat. Mater **9**, 541 (2010).

[52] H. Lin, L. A. Wray, Y. Xia, S. Xu, S. Jia, R. J. Cava, A. Bansil, et M. Z. Hasan, *Half-Heusler ternary compounds as new multifunctional experimental platforms for topological quantum phenomena*, Nat Mater **9**, 546 (2010).

[53] D. Xiao, Y. Yao, W. Feng, J. Wen, W. Zhu, X.-Q. Chen, G. M. Stocks, et Z. Zhang, *Half-Heusler Compounds as a New Class of Three-Dimensional Topological Insulators*, Phys. Rev. Lett. **105**, 096404 (2010).

[54] C. Li et Z. Wen, *Electronic structure of topological insulators with half-Heusler compounds using density functional theory*, Thin Solid Films **546**, 436 (2013).

[55] W. Al-Sawai, H. Lin, R. S. Markiewicz, L. A. Wray, Y. Xia, S.-Y. Xu, M. Z. Hasan, et A. Bansil, *Topological electronic structure in half-Heusler topological insulators*, Phys. Rev. B **82**, 125208 (2010).

[56] P. C. Canfield, J. D. Thompson, W. P. Beyermann, A. Lacerda, M. F. Hundley, E. Peterson, Z. Fisk, et H. R. Ott, *Magnetism and heavy fermion-like behavior in the RBiPt series*, J. Appl. Phys. **70**, 5800 (1991).

[57] Z. Fisk, P. Canfield, W. Beyermann, J. Thompson, M. Hundley, H. Ott, E. Felder, M. Maple, M. Lopez de la Torre, P. Visani, et C. Seaman, *Massive electron state in YbBiPt*, Physical Review Letters **67**, 3310 (1991).

[58] N. Kozlova, J. Hagel, M. Doerr, J. Wosnitza, D. Eckert, K.-H. Müller, L. Schultz, I. Opahle, S. Elgazzar, M. Richter, G. Goll, H. v. Löhneysen, G. Zwicknagl,

T. Yoshino, et T. Takabatake, *Magnetic-Field-Induced Band-Structure Change in CeBiPt*, Physical Review Letters **95**, 086403 (2005).

[59] K. Gofryk, D. Kaczorowski, T. Plackowski, J. Mucha, A. Leithe-Jasper, W. Schnelle, et Y. Grin, *Magnetic, transport, and thermal properties of the half-Heusler compounds ErPdSb and YPdSb*, Physical Review B **75**, 224426 (2007).

[60] G. Xu, W. Wang, X. Zhang, Y. Du, E. Liu, S. Wang, G. Wu, Z. Liu, et X. X. Zhang, *Weak antilocalization effect and noncentrosymmetric superconductivity in a topologically nontrivial semimetal LuPdBi.*, Scientific Reports **4**, 5709 (2014).

[61] C. Liu, Y. Lee, T. Kondo, E. D. Mun, M. Caudle, B. N. Harmon, S. L. Budko, P. C. Canfield, et A. Kaminski, *Metallic surface electronic state in half-Heusler compounds RPtBi (R= Lu, Dy, Gd)*, Phys. Rev. B **83**, 205133 (2011).

[62] A. Kreyssig, M. G. Kim, J. W. Kim, D. K. Pratt, S. M. Sauerbrei, S. D. March, G. R. Tesdall, S. L. Budḱo, P. C. Canfield, R. J. McQueeney, et A. I. Goldman, *Magnetic order in GdBiPt studied by x-ray resonant magnetic scattering*, Phys. Rev. B **84**, 220408 (2011).

[63] R. A. Robinson, A. Purwanto, M. Kohgi, P. C. Canfield, T. Kamiyama, T. Ishigaki, J. W. Lynn, R. Erwin, E. Peterson, et R. Movshovich, *Crystallography and magnetism of the heavy-fermion compound YbBiPt*, Physical Review B **50**, 9595 (1994).

[64] M. H. Jung, T. Yoshino, S. Kawasaki, T. Pietrus, Y. Bando, T. Suemitsu, M. Sera, et T. Takabatake, *Thermoelectric and transport properties of CeBiPt and LaBiPt*, J. Appl. Phys. **89**, 7631 (2001).

[65] S. Khmelevskyi, *Antiferromagnetic ordering on the frustrated fcc lattice in the intermetallic compound GdPtBi*, Phys. Rev. B **86**, 104429 (2012).

[66] M. E. Fisher et J. S. Langer, *Resistive anomalies at magnetic critical points*, Phys. Rev. Lett. , 665 (1968).

[67] M. E. Fisher, *Relation between the specific heat and susceptibility of an antiferromagnet*, Phil. Mag. **7**, 1731 (1962).

[68] D. H. Ryan et L. M. D. Cranswick, *Flat-plate single-crystal silicon sample holders for neutron powder diffraction studies of highly absorbing gadolinium compounds*, J. Appl. Cryst. **41**, 198 (2008).

[69] T. Chatterji, *Neutron Scattering from Magnetic Materials* (, 2006).

[70] T. Yildirim, A. Harris, et E. Shender, *Frustration and quantum fluctuations in Heisenberg fcc antiferromagnets*, Physical Review B **58**, 3144 (1998).

[71] J. Rossat-Mignod, Magnetic structures of rare earth intermetallics, 1979.

[72] J. Rodríguez-Carvajal, *Recent advances in magnetic structure determination by neutron powder diffraction*, Physica B **192**, 55 (1993).

[73] G. Will, R. Nathans, et H. A. Alperin, Journal of Applied Physics **35**, 1045 (1964).

[74] M. Halder, S. M. Yusuf, A. Kumar, A. K. Nigam, et L. Keller, *Crossover from antiferromagnetic to ferromagnetic ordering in the semi-Heusler alloys Cu_{1,àíx}Ni_{x}MnSb with increasing Ni concentration*, Phys. Rev. B **84**, 094435 (2011).

[75] T. Roisnel et J. Rodriguez-Carvajal, *WinPLOTR: A Windows Tool for Powder Diffraction Pattern Analysis*, Mater. Sci. Forum **378-381**, 118 (2001).

[76] J. Lynn et P. Seeger, *Resonance effects in neutron scattering lengths of rare-earth nuclides*, Atomic Data and Nuclear Data Tables **44** (1990).

[77] STOE and Cie GmbH, *X-SHAPE 1.03: Crystal Optimization for Numerical Absorption Correction* (, 1997).

[78] G. M. Sheldrick, *A short history of SHELX.*, Acta crystallographica. Section A, Foundations of crystallography **64**, 112 (2008).

[79] A. Kreyssig, M. Kim, J. Kim, D. Pratt, S. Sauerbrei, S. March, G. Tesdall, S. Bud'ko, P. Canfield, R. McQueeney, et A. Goldman, *Magnetic order in GdBiPt studied by x-ray resonant magnetic scattering*, Physical Review B **84**, 220408 (2011).

[80] *APEX2 and SAINT, Version 7.68A* (Bruker AXS Inc., Madison, WI, 2009).

[81] G. M. Sheldrick, *SADABS, Version 2008* (Bruker AXS Inc., Madison, WI, 2008).

[82] D. Morelli, P. Canfield, et P. Drymiotis, *Low-temperature transport properties of NdBiPt*, Physical Review B **53**, 12896 (1996).

[83] M. Fisher et J. Langer, *Resistive Anomalies at Magnetic Critical Points*, Physical Review Letters **20**, 665 (1968).

[84] Z. Yamani, Z. Tun, et D. H. Ryan, *Neutron scattering study of the classical antiferromagnet* MnF_2 *: a perfect hands-on neutron scattering teaching courseSpecial issue on Neutron Scattering in Canada.*, Canadian Journal of Physics **88**, 771 (2010).

[85] M. Blume, A. J. Freeman, et R. E. Watson, *Neutron Magnetic Form Factors and X-Ray Atomic Scattering Factors for Rare-Earth Ions*, The Journal of Chemical Physics **37**, 1245 (1962).

[86] J. Rodriguez-Carvajal, *Recent advances in magnetic structure determination neutron powder diffraction*, Physica B **192**, 55 (1993).

[87] G. Shirane, S. M. Shapiro, et J. M. Tranquada, *Neutron Scattering with a Triple Axis Spectrometer* (Cambridge University Press, Cambridge, 2002).

[88] A. Pelissetto et E. Vicari, *Critical phenomena and renormalization-group theory*, Physics Reports **368**, 549 (2002).

[89] G. Goll, O. Stockert, M. Prager, T. Yoshino, et T. Takabatake, *Low-energy excitations in CeBiPt*, J. Magn. Magn. Mater **310**, 1773 (2007).

[90] M. T. Hutchings, *Point-Charge Calculations of Energy Levels of Magnetic Ions in Crystalline Electric Fields*, Solid State Physics - Advances in Research and Applications **16**, 227 (1964).

[91] K. W. H. Stevens, Matrix Elements and Operator Equivalents Connected with the Magnetic Properties of Rare Earth Ions, 2002.

[92] K. Lea, M. Leask, et W. Wolf, *The raising of angular momentum degeneracy of f-Electron terms by cubic crystal fields*, Journal of Physics and Chemistry of Solids **23**, 1381 (1962).

[93] R. H. Forster, G. B. Johnston, N. S. Wales, D. A. Wheeler, et L. Heights, *Studies on the heusler alloys. The antiferro-magnetic phase in the Cu-Mn-Sb system*, Ôø^{o}J. Phys. Chem. Solids **29**, 855 (1968).

[94] J. Wosnitza, G. Goll, a. D. Bianchi, B. Bergk, N. Kozlova, I. Opahle, S. Elgazzar, M. Richter, O. Stockert, H. V. Löhneysen, T. Yoshino, et T. Takabatake, *Magnetic-field- And temperature-dependent fermi surface of CeBiPt*, New Journal of Physics **8** (2006).

[95] D. J. Kim, T. Grant, et Z. Fisk, *Limit cycle and anomalous capacitance in the Kondo insulator SmB_6*, Physical Review Letters **109** (2012).

[96] D. J. Kim, J. Xia, et Z. Fisk, *Topological surface state in the Kondo insulator samarium hexaboride.*, Nature materials **13**, 466 (2014), 1307.0448.

[97] S. Wolgast, c. Kurdak, K. Sun, J. W. Allen, D.-J. Kim, et Z. Fisk, *Low-temperature surface conduction in the Kondo insulator* SmB_6, Physical Review B **88**, 180405 (2013).

[98] V. Gnezdilov, Y. G. Pashkevich, H. Berger, E. Pomjakushina, K. Conder, et P. Lemmens, *Helical fluctuations in the Raman response of the topological insulator* Bi_2Se_3, Physical Review B **84**, 195118 (2011).

LIST OF APPENDICES

Appendix I

Code

I.1 Mathematica code to calculate the magnetic moment of NdBiPt from the neutron scattering integrated intesities

```
A = 0.054;
a = 25.0293;
B = 0.3101;
b = 12.102;
G = 0.6575;
g = 4.7223;
Q = −0.0216;
AS = 0.6751;
aS = 18.3421;
BS = 1.6272;
bS = 7.26;
GS = 0.9644;
gs = 2.6016;
QS = 0.015;
(*GroundelectronicstateofNd3 + is4 4I9/2withS = 3/2, L = 6, J = 9/2*)

L = 6;
S = 1.5;
J = 4.5;
```

magneticformfactorindipoleapprox

$$j{:=}1+\frac{J(J+1)+S(S+1)-L(L+1)}{2J(J+1)};$$

```
j0[s_]:=AExp[−a∗(s)^2]+BExp[−b∗(s)^2]+GExp[−g∗(s)^2]+Q;
j2[s_]:=(s^2)(ASExp[−aS(s^2)]+BSExp[−bS(s^2)]+GSExp[−gs(s^2)]+QS)
```

approxdipolefactorforminmagnetic

```
(*approx dipole factor form in magnetic*)
```

```
Plot[{j0[x],j2[x]},{x,0,0.6366}]
```

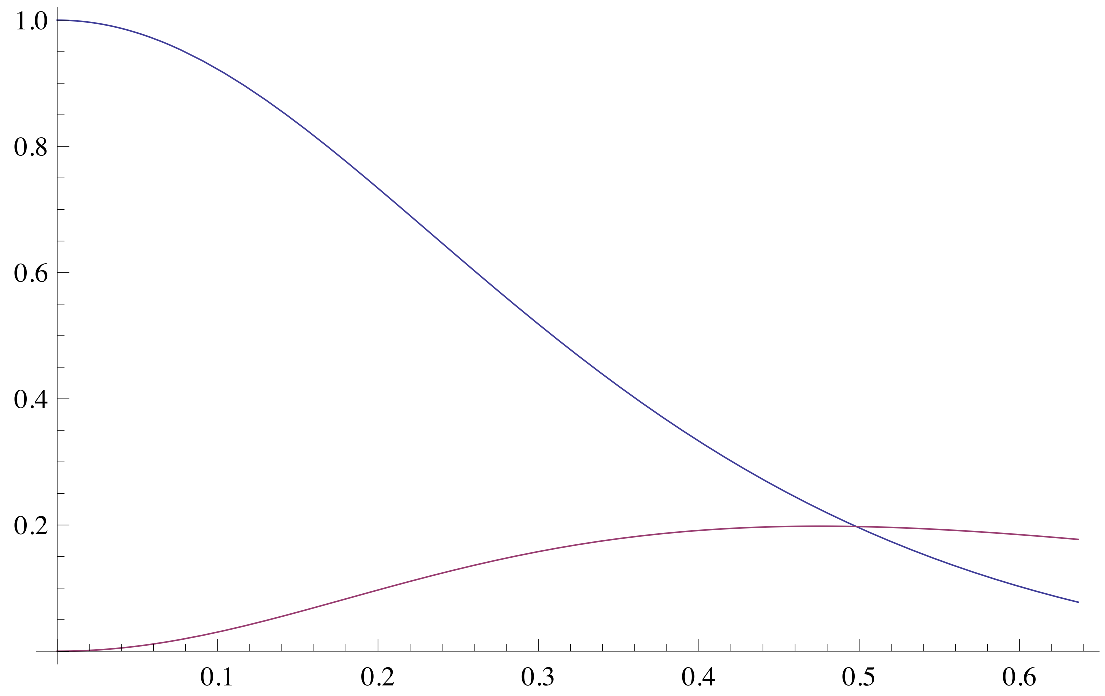
1.0
0.8
0.6
0.4
0.2
0.1
0.2
0.3
0.4
0.5
0.6

```
gg:=1 + (J(J + 1) + S(S + 1) − L(L + 1))/(2J(J + 1))

h1:=(J(J + 1) − S(S + 1) + L(L + 1))/(3J(J + 1) + S(S + 1) − L(L + 1));

w2[s_]:=j0[s] + j2[s] ∗ (1 − (2/gg));

w[s_]:=j0[s] + j2[s] ∗ h1;

(*R[s_]:=r0^2 ∗ j^2 ∗ w[s]^2 ∗ J(J + 1)/6*)

(*Plot[w[s], {s, 0, 10}, PlotRange → All]*)

Plot[{j0[x], j2[x], w[x]^2}, {x, 0, 0.628}]
```

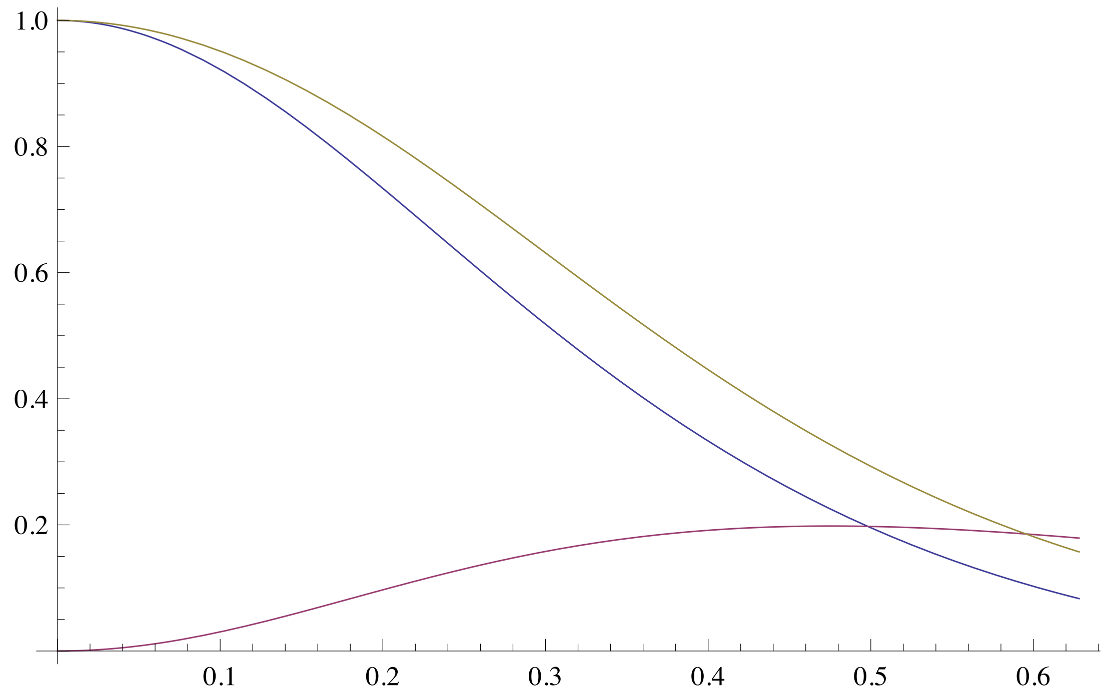
1.0
0.8
0.6
0.4
0.2
0.1
0.2
0.3
0.4
0.5
0.6

```
k = 2 * Pi/2.37051;

Q1[h_,l_]:=Sqrt[h^2 + h^2 + l^2] * 2Pi/6.7613;(*scattering vector*)

(*Phimag[q_]:=2 * ArcSin[q/(2 * k)];*)

Betrag[h_,l_]:=Sqrt[h^2 + h^2 + l^2];

Angle[q_]:=ArcSin[(q)/(2 * k)];

q2[angle_]:=4 * Pi * Sin[angle]/2.37051;

q1 = Q1[1,0]

1.31421

Phinuc = 2 * Angle[Q1[1,1]]

phimag1:=2 * Angle["1.31421"];

N[phimag1];

0.616997


Q1[1,0](*tousefunctionw, Q1hastobedividedby4Pi*)

1.31421

(*magnetic structure factor calculation*)


fmag[h_,l_]:=2.69 * Abs[(w[(Q1[h,l]/(4 * Pi))] * Exp[2 * Pi * I * ((h * 1.69) + (h * 1.69) + (l * 1.69))])+


(w[(Q1[h,l]/(4 * Pi))] * Exp[2 * Pi * I * ((h * 5.07) + (h * 5.07) + (l * 1.69))]) - (w[(Q1[h,l]/(4 * Pi))] * Exp[


(w[(Q1[h,l]/(4 * Pi))] * Exp[2 * Pi * I * ((h * 5.07) + (h * 1.69) + (l * 5.07))]) + (w[(Q1[h,l]/(4 * Pi))] * Exp[


(w[(Q1[h,l]/(4 * Pi))] * Exp[2 * Pi * I * ((h * 5.07) + (h * 5.07) + (l * 8.45))])];

fmag[1,0]

9.05158
```

```
Imag:=03.31861 * 10^(−4); (*3.31861 * 10^(−4); at0.99K*)
Inuc = 0.0037464312329997186299590511;
Fnuc = 923.640; (*1199.102;*)
CQ:=(Inuc/(Abs[Fnuc])) * Sin[Phinuc];
Mucal = Sqrt[(Sin[phimag1] * Imag)/(CQ)] * (1/(fmag[1,0]))(*8/9 = (1 − (hat(Q) * hat(mu)))^2*)
“0.640478” * 3
1.92143


fmag2[h_,1_]:=2.69 * Mucal * Abs[(w[(Q1[h,l]/(4 * Pi))] * Exp[2 * Pi * I * ((h * 1.69) + (h * 1.69) + (l * 1.69
(w[(Q1[h,l]/(4 * Pi))] * Exp[2 * Pi * I * ((h * 5.07) + (h * 5.07) + (l * 1.69))]]);


Phinuc2 = 2 * Angle[Q1[1,1]];
Inuc2 = 5.58857 * 10^(−3);
CQx:=(Inuc2/(Abs[Fnuc])) * Sin[Phinuc2];


phimag2:=2 * Angle[Q1[1,0]]


Imag3[h_,1_]:=(fmag2[h,l])^2 * ((CQ(1 − (Normalize[{h,h,l}].Normalize[{0,0,1}])^2))/Sin[phimag2]);
Imag3[1,0]
0.000373343
```

I.2 Mathematica code to fit the Schottky anomaly

```
R:=8.314472(*Universal constant*)
kB:=1.3806488/10^23(*Boltzman constant*)
Na:=6.02214129 ∗ 10^23(*Avogadro number*)
ℏ:=1.054571628/10^34(*Plancks constant*)
At:=1(*NdBiPt has 12 atoms per unit cell*)
a:=6.7613/10^10(*lattice constant NdBiPt*)
n:=At/a^3(*NdBiPt contains 12 atoms per unit cell*)
(*this program calculates the crystal field hamiltonian and diagonalize the hamiltonian*)
(*this program useS the LLW notation*)(*jistheangularmomentumofthestate,*)
j = Input["Please input the value of the angular momentum"];

n = Input["Please input the number of points plotted between 2 and 100"];
ncoord = 6;
(*the following parameters are for quantization axis along the four fold axis*)
c4 = Table[0, {c2, 1, 17}]; (*factorsforconvertingtheH&Pnotationinllw*)
c6 = Table[0, {c2, 1, 17}];
c4[[17]] = 0.0011570726; c6[[17]] = 0.000957496;
c4[[16]] = 0.001484961; c6[[16]] = 0.001408758;
c4[[15]] = 0.00193873; c6[[15]] = 0.0005816218;
c4[[14]] = 0.00258175; c6[[14]] = 0.00182076;
c4[[13]] = 0.00351833; c6[[13]] = 0.002965701;
c4[[12]] = 0.00492760; c6[[12]] = 0.00253523;
c4[[11]] = 0.00166429; c6[[11]] = 0.001535158;
c4[[10]] = 0.01075291; c6[[10]] = 0.006035056;

(*initialize the hamiltonian matrix ham*)
```

```
(*ham4 is the matrix for the rank four operator*)
(*ham6 is the matrix for the rank six operator*)
ei = Table[0,{c1,−n,n},{c2,−j, j}];
stheta = Table[0,{c1,−n,n}];
ham = Table[0,{c1,−j, j},{c2,−j, j}];
ham4 = Table[0,{c1,−j, j},{c2,−j, j}];
ham6 = Table[0,{c1,−j, j},{c2,−j, j}];
sover = Table[0,{c1,−j, j},{c2,−j, j}];

(*beginning section for eight fold degeneracy*)

If[ncoord == 8,(*initialize matrix for tensor operators*)
(*c40 tensor operator rank 4 zero component m4 means minus 4 p4 means plus 4*)
c40 = Table[ClebschGordan[{4,0},{j,c1},{j,c2}],{c2,−j, j},{c1,−j, j}];
c4m3 = Table[ClebschGordan[{4,−3},{j,c1},{j,c2}],{c2,−j, j},{c1,−j, j}];
c4p3 = Table[ClebschGordan[{4,3},{j,c1},{j,c2}],{c2,−j, j},{c1,−j, j}];
c60 = Table[ClebschGordan[{6,0},{j,c1},{j,c2}],{c2,−j, j},{c1,−j, j}];
c6m3 = Table[ClebschGordan[{6,−3},{j,c1},{j,c2}],{c2,−j, j},{c1,−j, j}];
c6p3 = Table[ClebschGordan[{6,3},{j,c1},{j,c2}],{c2,−j, j},{c1,−j, j}];
c6m6 = Table[ClebschGordan[{6,−6},{j,c1},{j,c2}],{c2,−j, j},{c1,−j, j}];
c6p6 = Table[ClebschGordan[{6,6},{j,c1},{j,c2}],{c2,−j, j},{c1,−j, j}];
ham4 = (−2/3) ∗ (Sqrt[7/12] ∗ N[c40] + Sqrt[20/24] ∗ N[(c4m3 − c4p3)]);
ham6 = 2 ∗ (Sqrt[8] ∗ N[c60] + Sqrt[70/24] ∗ N[(c6p3 − c6m3)] + Sqrt[77/24] ∗ N[(c6m6 + c6p6)])/9;

“eigenvalues” >> /Users/roger/eigen1.dat;
 “eigenvalues” >> /Users/roger/eigen2.dat;
```

```
Do[theta = i/n;
stheta[[i + n + 1]] = theta;
ham = theta * ham4/c4[[2 * j + 1]] + (1. − Abs[theta]) * ham6/c6[[2 * j + 1]];
et = Eigenvalues[ham];
et = Sort[et];
Do[ei[[i + n + 1, c2]] = et[[c2]]; (*Print[et[[c2]]]*), {c2, 1, 2 * j + 1}];
theta >>> /Users/roger/eigen1.dat;
ei[[i + 1]] >>> /Users/roger/eigen1.dat;
, {i, −n, n}];];


(*output section for final results*)
(*the separation between two data points is $*)


“eigenvalues” >> /Users/roger/eigen2.dat;
finalresult = {}




Do[x1 = FortranForm[N[stheta[[i1]]]];
x2 = FortranForm[ei[[i1, i2]]];
r1 = N[stheta[[i1]]];
r2 = ei[[i1, i2]];
x3 = SequenceForm[x1, $, x2];
finalresult = Append[finalresult, {r1, r2}];
If[i1 == 1, “level” >>> /Users/roger/eigen2.dat];
x3 >>> c:\temp\eigen2.dat;, {i2, 1, 2 * j + 1}, {i1, 1, 2 * n + 1}];
```

```
(*end of section of eight fold degeneracy*)

Print[“j=”, j];

ListPlot[finalresult, Prolog → AbsolutePointSize[2.], AspectRatio → 1, Ticks → Automatic,

Frame → True, PlotLabel → “Crystal field levels”, Prolog → Text[“j=”, {0.0, 0.0}],

Prolog → Text[j, {0.8, 0.1}]]
```

```
j=4.5
```

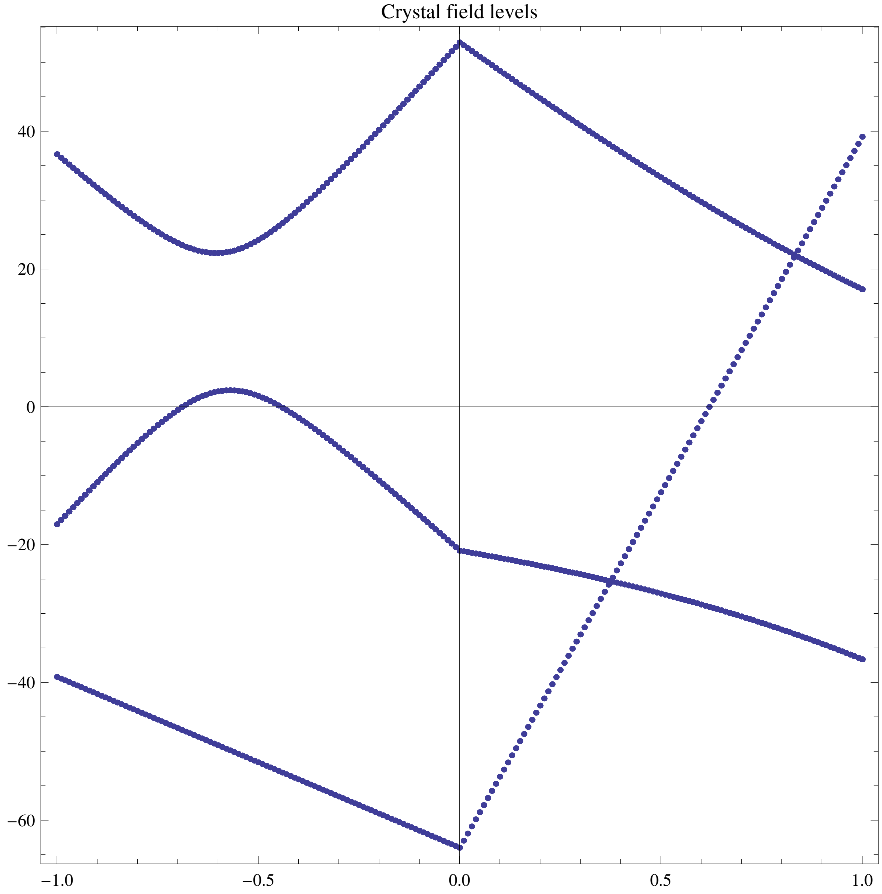

```
A1 = Select[finalresult, #[[1]] == 0&];

A2 = Select[finalresult, #[[1]] == −0.1&];

A3 = Select[finalresult, #[[1]] == −0.2&];

A4 = Select[finalresult, #[[1]] == −0.4&];

A5 = Select[finalresult, #[[1]] == −0.5&];
```

```
A6 = Select[finalresult,#[[1]] == −0.6&];
A7 = Select[finalresult,#[[1]] == −0.7&];
A8 = Select[finalresult,#[[1]] == −0.8&];
A9 = Select[finalresult,#[[1]] == −0.9&];
A10 = Select[finalresult,#[[1]] == −1&];
A11 = Sort[A1,#1[[2]] < #2[[2]]&];
A22 = Sort[A2,#1[[2]] < #2[[2]]&];
A33 = Sort[A3,#1[[2]] < #2[[2]]&];
A44 = Sort[A4,#1[[2]] < #2[[2]]&];
A55 = Sort[A5,#1[[2]] < #2[[2]]&];
A66 = Sort[A6,#1[[2]] < #2[[2]]&];
A77 = Sort[A7,#1[[2]] < #2[[2]]&];
A88 = Sort[A8,#1[[2]] < #2[[2]]&];
A99 = Sort[A9,#1[[2]] < #2[[2]]&];
A1010 = Sort[A10,#1[[2]] < #2[[2]]&];

OAS1 = Abs[A11[[10,2]] − A11[[1,2]]];
OAS2 = Abs[A22[[10,2]] − A22[[1,2]]];
OAS3 = Abs[A33[[10,2]] − A33[[1,2]]];
OAS4 = Abs[A44[[10,2]] − A44[[1,2]]];
OAS5 = Abs[A55[[10,2]] − A55[[1,2]]];
OAS6 = Abs[A66[[10,2]] − A66[[1,2]]];
OAS7 = Abs[A77[[10,2]] − A77[[1,2]]];
OAS8 = Abs[A88[[10,2]] − A88[[1,2]]];
OAS9 = Abs[A99[[10,2]] − A99[[1,2]]];
OAS10 = Abs[A1010[[10,2]] − A1010[[1,2]]];
Delta1 = Abs[A11[[5,2]] − A11[[1,2]]];
```

```
Delta2 = Abs[A22[[5,2]] – A22[[1,2]]];
Delta3 = Abs[A33[[5,2]] – A33[[1,2]]];
Delta4 = Abs[A44[[5,2]] – A44[[1,2]]];
Delta5 = Abs[A55[[5,2]] – A55[[1,2]]];
Delta6 = Abs[A66[[5,2]] – A66[[1,2]]];
Delta7 = Abs[A77[[5,2]] – A77[[1,2]]];
Delta8 = Abs[A88[[5,2]] – A88[[1,2]]];
Delta9 = Abs[A99[[5,2]] – A99[[1,2]]];
Delta10 = Abs[A1010[[5,2]] – A1010[[1,2]]];
Elements1 = {{0.1,Delta1},{0.2,Delta2},{0.3,Delta3},{0.4,Delta4},{0.5,Delta5},{0.6,Delta6},
{0.7,Delta7},{0.8,Delta8},{0.9,Delta9},{1,Delta10}};
Elements2 = {{0.1,OAS1},{0.2,OAS2},{0.3,OAS3},{0.4,OAS4},{0.5,OAS5},{0.6,OAS6},
{0.7,OAS7},
{0.8,OAS8},{0.9,OAS9},{1,OAS10}};
LinearModelFit[Elements2,{x^3,x^2,x},x]
LinearModelFit[Elements1,{x^3,x^2,x},x]
(*Polinomial functions fitting above calculated values of E’ and x *)
fDelta[a_]:=“133.131” –“148.263”a+“60.0113”a^2+“32.5355”a^3;
fOAS[a_]:=“35.962”+“66.7043” a–“57.4822”a^2–“24.1051”a^3;
pingu = Plot[fDelta[x],{x,0,1},PlotRange → {All,All},PlotStyle → Blue];
malmo = Plot[fOAS[x],{x,0,1},PlotRange → {All,All},PlotStyle → Blue];
Show[pingu,malmo]
(*Debye specific heat*)
Ctotd[Td_?NumberQ,θd_?NumberQ,γ_?NumberQ,al_?NumberQ]:=
```

$$\gamma\mathrm{Td}+\left(\left(\frac{9*6*R}{1-\mathrm{al}*\mathrm{Td}}\right)*\left(\frac{\mathrm{Td}}{\theta\mathrm{d}}\right)^{3}\mathrm{NIntegrate}\left[\frac{x^{4}e^{x}}{(e^{x}-1)^{2}},\{x,0.01,\theta\mathrm{d}/\mathrm{Td}\}\right]\right);$$

```
(*Schottky anomaly*)
Cschottky[Δ_?NumberQ,Θ_?NumberQ,w_?NumberQ,T_?NumberQ]:=
```

$$\frac{R}{T^2}\left(\frac{(w*\Delta)^2*4e^{\frac{-w*\Delta}{T}}+(w*\Theta)^2*4e^{\frac{-w*\Theta}{T}}}{2+4e^{\frac{-w*\Delta}{T}}+4e^{\frac{-w*\Theta}{T}}}-\left(\frac{w*\Delta*4e^{\frac{-w*\Delta}{T}}+w*\Theta*4e^{\frac{-w*\Theta}{T}}}{2+4e^{\frac{-w*\Delta}{T}}+4e^{\frac{-w*\Theta}{T}}}\right)^2\right);$$

Estimate the best fit to the specific heat data using the above polynomials as input into the schottky fct;

```
Clear[w,x,a,Const1c,Const2c];Off[Fit::fitc]
dataZT =
Import[
"/Users/roger/Google
Drive/NdBiPt_LOG_BOOK/NdBiPt_PhaseDiagram_LogBook_
Data/20141103_schottky/merge.txt", “Data”
dataZTsubPhon1 =
ReplacePart[#, 2 → #[[2]] − Ctotd[#[[1]], “205.57”, 0, −“0.00749226”]]&/@dataZT;
dataZTsubPhonfit1 = Select[dataZTsubPhon1, #[[1]] > 4&];
dataZTsubPhonfit2 = Select[dataZTsubPhonfit1, #[[1]] < 17&];
plot2 = ListPlot [dataZTsubPhon1, PlotStyle → Red, AxesLabel → {T, Cp}] ;
schottky = NonlinearModelFit[dataZTsubPhonfit2, Cschottky[fDelta[x], fOAS[x], w, T],
{{x}, {w}}, T, Method → LevenbergMarquardt];
schottky[“ParameterTable”]
Schottkytable = schottky[“ParameterTableEntries”];
Const1c:=Schottkytable[[1, 1]]
Const2c:=Schottkytable[[2, 1]]
schottkyplot = Plot[N[Cschottky[fDelta[Const1c], fOAS[Const1c], Const2c, t]], {t, 0, 30},
PlotRange → {All, All}, PlotStyle → Blue];
Show [schottkyplot, plot2, AxesLabel → {T, Cp}]
ΔE1 = Const2c ∗ fDelta[Const1c];
ΔE2 = Const2c ∗ fOAS[Const1c];
```

	Estimate	Standard Error	t-Statistic	P-Value
x	0.964647	0.00469323	205.54	1.96609×10^{-47}
w	1.14119	0.0263027	43.3869	6.24024×10^{-28}

Δ_{E1}

“28.7359”

Δ_{E2}

“85.7704”

I.3 Mathematica code to solve Brillouin function

```
SetDirectory[“/Users/myself/Google Drive/NdBiPt_LOG_BOOK/NdBiPt_PhaseDiagram_LogBook_Data/20141126_NdBiPt_Brillouin_fit/”]
Import[“multicef_2.m”];
InitMultiCef[9/2]
MultiCEF initialized. Version 2.3 with J = 9/2
F4 = 60
60
F6 = 2520
2520
B4 = -Wx/F4
-Wx/60
B6 = -W(1 - Abs[x])/F6
-W(1-Abs[x])/2520
O4 = O40 + 5 * O44
SparseArray[]
O6 = O60 - 21 * O66
SparseArray[]
(*testing the reverse value obtained for x and W *)
x:=1.1453523702908341
W:=“0.71397”
{es, vs} = Eigensystem[CreateHcefcub[B4, B6;]]
ordre = Ordering[es];
{es, vs} = {es[[ordre]], vs[[ordre]]};
g61 = Chop[vs[[1]]](*gamma6groundstate + *)
{0, 0.204124, 0, 0, 0, 0.763763, 0, 0, 0, 0.612372}
g62 = Chop[vs[[2]]](*gamma6groundstate - *)
```

{0.612372, 0, 0, 0, 0.763763, 0, 0, 0, 0.204124, 0}

Meas[Jz, g61]

1.83333

Meas[Jz, g62]

−1.83333

(*We assume that we have an effective doublet which corresponds to spin 1/2, so the Brillouin function is now just the tanh *)

Needs["ErrorBarPlots"];

$\mathbf{JJ:=\frac{9}{2};}$

LL:=6;

$\mathbf{SS:=\frac{3}{2};}$

$$g=\frac{3}{2}+\frac{\mathrm{SS(SS+1)-LL(LL+1)}}{\mathrm{2JJ(JJ+1)}}$$

B[x_]:=Tanh[x];

χ:=Limit[D[B[x], x], $x \to 0$];

$\frac{8}{11}$

$$\mathrm{FindY[CW\_?NumericQ, T\_?NumericQ]:=}y\mathrm{/.FindRoot}\left[\frac{1}{\chi}B[y]==y\left(\frac{T}{\mathrm{CW}}\right),\{y,100\}\right];$$

$$\mathrm{CC[M\_?NumericQ, BG\_?NumericQ, CW\_?NumericQ, T\_?NumericQ]:=}(MB[\mathrm{FindY}[\mathrm{CW},T]])^2+\mathrm{BG};$$

rawdata = Import["/Users/myself/Google Drive/NdBiPt_LOG_BOOK/NdBiPt_fit/brillouin.txt", "Data"]

data = Drop[rawdata, None, {3}];

Δys = Flatten[Take[rawdata, All, {3}], 1];

p1 = ErrorListPlot[rawdata, AxesOrigin → {0, 0}, PlotRange → {{0, 3}, {0, 7}}, AxesLabel → {Temperature, integratedintensity}];

nlm = NonlinearModelFit[data, CC[*M*, BG, CW, *T*], {{*M*, 2.5}, {BG, 0.05}, {CW, 2.2}}, *T*, *textWeights* → 1/Δys^2, VarianceEstimatorFunction → (1&)]

FittedModel[]

```
p3 = Plot[CC[“2.33286”, “0.0494832”, “2.17878”, T], {T, 0.1, 3}, PlotStyle → Red];

Show[p1, p3]
```

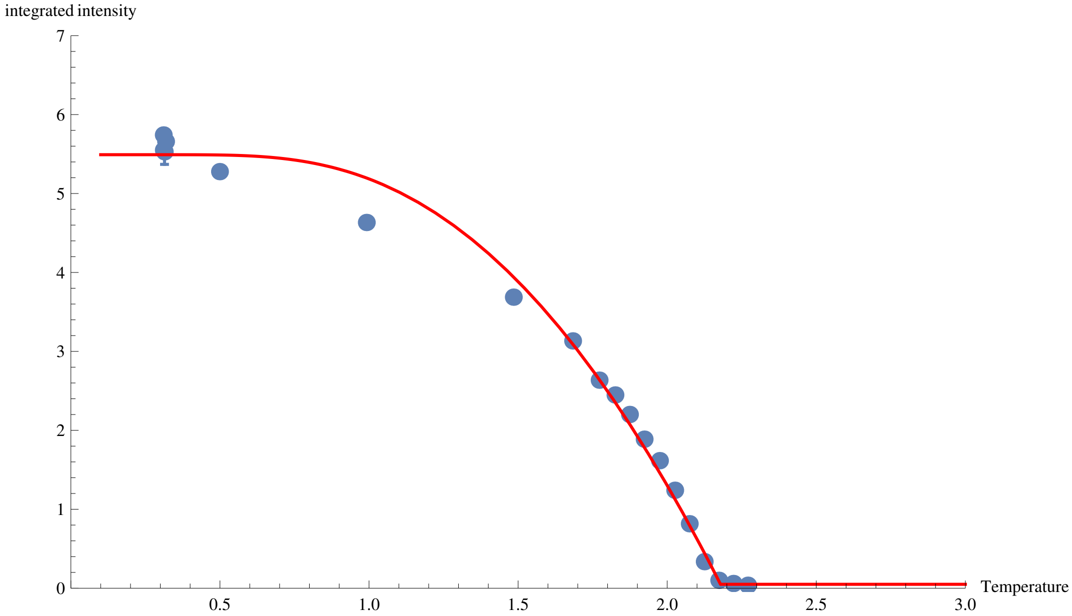

```
out = Table[{T, CC[“2.33286”, “0.0494832”, “2.17878”, T]}, {T, 0, 3, 0.01}]
```